DISSERTATION

SPECTRUM EFFICIENCY FOR FUTURE WIRELESS

COMMUNICATIONS

Submitted by

Bo Yu

Department of Electrical and Computer Engineering

In partial fulfillment of the requirements

For the Degree of Doctor of Philosophy

Colorado State University

Fort Collins, Colorado

Spring 2015

Doctoral Committee:

    Advisor: Liuqing Yang

    Jie Luo
    Yu Morton
    Haonan Wang

ABSTRACT

SPECTRUM EFFICIENCY FOR FUTURE WIRELESS COMMUNICATIONS

Spectrum efficiency has long been at the center of wireless communication research, development, and operation. Today, it is even more so with the explosive popularity of mobile internet, social networks, and smart phones that are more powerful than our desktops not long ago. As a result, there is an urgent need to further improve the spectrum efficiency in order to provide higher wireless data capacity. To respond to this demand, the 3rd Generation Partnership Project (3GPP) standardized the radio interface specifications for the next generation mobile communications system, called Long Term Evolution (LTE), in Release 8 specifications in 2008. Then the development continued and an enhanced LTE radio interface called LTE-Advanced (LTE-A) was standardized in Release 10 specifications in 2011. In order to ensure the sustainability of 3GPP radio access technologies over the coming decade, 3GPP standardization will need to continue identifying and providing new solutions that can respond to the future challenges.

In this research, we investigate the potential technologies for further spectrum efficiency enhancement in the future steps of the standardization. One key direction is the further enhancement of local area technologies, which play a more and more important role in complementing the wide area networks. Specifically, we investigate two promising techniques for spectrum efficiency improvement in a macro-assisted small cell architecture, called the *Phantom cell*, which is proposed by DOCOMO.

One is the possibility of dynamic allocation of subframes to uplink (UL) or downlink (DL) in time-division duplexing (TDD), called 'Dynamic TDD'. The other is the more dynamic and flexible 3-dimensional (3D) beamforming which is facilitated by the adoption of active antenna systems (AAS) in BSs. In addition, full-duplex transmission and cooperative communication are two promising techniques known to enhance the spectrum efficiency of wireless communications. We focus on applying full-duplex in cooperative relaying networks and investigating the optimal resource allocation (both power and relay location) for full-duplex decode-and-forward (DF) relaying systems for spectrum efficiency enhancement.

ACKNOWLEDGMENTS

that have supported me through the PhD study.

TABLE OF CONTENTS

LIST OF TABLES

LIST OF FIGURES

CHAPTER 1

INTRODUCTION

"When you have a scarce resource, an industry run as an oligopoly and a population that can't get enough, you have all the ingredients for the first new resource crisis of the millennium." No, not oil-This excerpt from a 2010 TIME Magazine article is all about the wireless spectrum. Driven by new services and terminal capabilities, the dramatic growth of mobile data traffic over the past several years further points to this truth. According to the latest forecast by Cisco [17], the global mobile data traffic grew 81 percent in 2013, reaching 1.5 exabytes per month at the end of 2013. The overall mobile data traffic is expected to grow to 15.9 exabytes per month by 2018, nearly an 11-fold increase over 2013. To respond to this demand, the 3rd Generation Partnership Project (3GPP) has initiated studies on the further evolution of Long Term Evolution/ Long Term Evoluation-Advanced (LTE/LTE-A). In this dissertation, we will focus on two potential directions for the future steps of the evolution, namely, small cell enhancement and full-duplex relaying.

1.1 Dynamic TDD in macro-assisted small cell architecture

Dynamic allocation of subframes to uplink (UL) or downlink (DL) in Time Division Duplex (TDD), termed 'Dynamic TDD,' has been studied by 3GPP since the LTE Release 11 timeframe. At the same time, 3GPP is also standardizing macro-assisted small cell heterogeneous architectures for inclusion in LTE Release 12 as a

solution offering high data rate to user terminals (UEs) along with high system capacity through spatial reuse of spectrum. In this study, we focus on a particular small cell architecture proposed by DOCOMO, known as the Phantom Cell architecture [41, 27, 9, 64], which provides the option to support dynamic TDD. A detailed description of the architecture can be found in [27]. The architecture permits flexibility with regard to the extent of coordination and signaling across phantom cells. In particular, thanks to having no (or much less) cell-specific fixed channel/signaling, dynamic DL/UL slot reconfiguration ('Dynamic TDD') and dynamic DL power control can be easily realized, thus facilitating more efficient use of spectrum.

Recently stochastic geometry has emerged as an effective tool for cellular network modeling and gained lots of popularity in the research community [7, 36, 21]. If the only interference on a DL (UL) subframe is from out-of-cell DL (UL) transmissions, then we can use recent results for the distribution of DL [6] and UL [19] signal to interference plus noise ratio (SINR). However, when we have dynamic TDD with incomplete coordination and/or imperfect synchronization across phantom cells, there is additional interference on the DL (UL) subframes from out-of-cell UL (DL) transmissions. This arises because of possibly different sequences of UL and DL subframes in the radio frames for different phantom cells, where the starting and ending time of these subframes may not be exactly aligned. Allocating shared UL/DL resources across phantom cells to optimize a network utility function is a difficult combinatorial problem [5]. An overview of dynamic UL/DL reconfiguration in time-division LTE systems has been provided in [53]. In [39], the UL/DL optimization problem is for-

mulated as a noncooperative game among the small cell BSs in which each BS aims at minimizing its total UL and DL flow delays. In order to address the interference issue for dynamic DL/UL slot assignment in TDD systems, some interference coordination techniques have been proposed in the literature such as the busy-burst TDMA [42], time-slot opposing [26], time-slot allocation [54], and cell clustering [53], etc.

In this dissertation, we focus on the benefits and tradeoffs of having no coordination across phantom cells. We couple this with 'Dynamic TDD' resource allocation, wherein each phantom cell is free to redistribute the resources allocated to DL and UL transmissions depending on traffic load, without coordinating with or informing any other phantom cell. We first derive the distribution of DL and UL SINR analytically and then simulation results are provided to verify our analytic results. Based on the analytic results, we observe significant interference for both DL and UL, especially for UL when DL uses fixed transmit power. In order to mitigate the severe inter-cell interference (ICI) for dynamic TDD, we further propose a novel technique for inter-cell interference coordination (ICIC), namely, the half-duplex FDD-like radio resource assignment technique. We evaluate the performance of dynamic TDD and the proposed ICIC technique via dynamic system level simulations under more realistic system assumptions and partial buffer traffic models. We also study the effect of different propagation models on the performance of dynamic TDD and some interesting results are observed.

1.2 3D beamforming in macro-assisted small cell architecture

In existing cellular systems, the BS antenna array has remained passive and can only adjust the beam in the horizontal dimension while the beamwidth in the vertical dimension and the antenna down-tilt are usually fixed. The capability of tilting the transmit beam angle and controlling the antenna beam pattern in the full 3D space will intuitively improve the overall system throughput and interference management, especially for scenarios where mobile users are distributed in a 3-dimensional (3D) space with distinguishable elevation such as modern urban environments. This is becoming increasingly important with the prevalence of the small cell concept, in which the horizontal scale becomes more comparable with the vertical scale.

Recently, the employment of active antenna system (AAS) at base stations (BSs) has been approved by 3GPP at TSG RAN #53 in September, 2011. The AAS technology integrates radio frequency components (power amplifiers and transceivers) with the antenna elements. In this manner, the phase and amplitude of the signals from each antenna element can be electronically controlled, thus facilitating more flexible and intelligent beamforming and resulting in increased capacity and coverage. With a 2D or 3D AAS array at the BS, the antenna radiation pattern can be dynamically controlled in both horizontal and vertical dimensions, thus enabling 3D beamforming as opposed to the conventional 2D beamforming. The AAS-enabled 3D beamforming is attracting significant attention from academic researchers, as well as industrial developers and operators [60, 12, 33, 13, 66, 65, 63, 13].

In this dissertation, we exploit the AAS-enabled 3D beamforming for traffic load

balancing and capacity enhancement in the macro-assisted small cell architecture. In terms of traffic load balancing, we propose the dynamic 3D UE-specific beamforming and show that it is especially feasible for this small cell architecture and also very effective due to its unique characteristics that the received signal is maximized while the interference is limited with narrower beamwidth. Then we formulate the load balancing problem as a log utility maximization problem and a two-step solution is provided, namely, the inter-cell load balancing (cell association) and intra-cell load balancing (cell sectorization). The performance of the proposed load balancing algorithms together with the UE-specific beamforming scheme is evaluated via system level simulations. In terms of capacity enhancement, we demonstrate that the flexible and dynamic 3D beamforming with narrow beamwidth can achieve significant performance gain compared to the conventional sectorization with fixed antenna down-tilt scheme in terms of both the cell average capacity and the cell edge user throughput. It is also shown that our proposed UE group-specific beamforming as a more realistic operation can approach to the performance of UE-specific beamforming.

1.3   Resource optimization for full-duplex relaying systems

Wireless cooperative communication has attracted significant attention in the literature by improving transmission reliability and increasing network coverage, thus improving the spectrum efficiency (see, e.g., [35, 40, 11, 68, 14] and the references therein). Relays are also a key new feature of LTE-Advanced, introduced in Release 10 of the LTE specifications, aiming to complement a macrocell network with

reduced cost by expanding coverage or increase capacity. However, in conventional relay communications, the relay operates in half-duplex mode, where the relay reception and transmission are carried out with either TDD or frequency-division duplexing (FDD). This implicitly limits the relay communication capacity. Recently, research in [20, 16, 30, 31] has shown that full-duplex radios have become feasible using off-the-shelf hardware and software radios. Full-duplex radio, which allows simultaneous transmission and reception, is enabled by advanced self-interference cancellation schemes, such as antenna cancellation, analog RF interference cancellation, and digital baseband interference cancellation. Other interference cancellation methods have also been proposed in the literature[22, 37, 47, 67]. It has also been shown that full-duplex radio can achieve higher throughput compared to the conventional half duplex systems with proper self-interference cancellation schemes. All these make full-duplex radio an attractive solution for high-rate wireless relay systems.

By employing full-duplex radio at the relay, full-duplex relaying is potentially more promising than the conventional half-duplex relaying in terms of its communication capacity. In [48] the feasibility of full-duplex relaying has been investigated by comparing the end-to-end capacity with the conventional half duplex relaying for both amplify-and-forward (AF) and decode-and-forward (DF) protocols. The results showed that the full-duplex mode offers capacity improvement over the half-duplex mode if the self-interference is below a certain level. Based on the trade-off between these two modes, a hybrid scheme which switches opportunistically between full-duplex and half-duplex modes has been proposed by the same authors in [46]

and transmit power adaptation at the relay node for maximizing instantaneous and average spectral efficiency is examined. Novel gain control schemes have also been proposed in [45] to maximize the end-to-end SINR for full-duplex AF relaying. In [57], an optimal transmission scheduling scheme is developed for a hybrid system using both full-duplex and half-duplex transmission, in order to achieve the maximum end-to-end throughput.

The optimal resource allocation for conventional half duplex relaying systems has been studied extensively in the literature (refer to [28, 15, 10] and the references therein). However, with the introduction of full transmission at the relay node, it is expected that the optimal transmit power allocation and optimal relay location selection will be distinct for full-duplex relay communications, due to the presence of residual self-interference (RSI) at the relay node. The optimal power allocation and relay location problems for full-duplex DF relaying have been discussed initially in [62] and [61], respectively. In this dissertation, we consider the power optimization problem with two different types of power constraints, namely, the individual power constraint and sum power constraint. The optimal power allocation strategies for relaying systems both with and without a direct source-destination link are then derived analytically. We show that the obtained results can be readily extended to the power optimization problem with the two types of constraints jointly considered. For location optimization, we extend our previous analysis in [61] to a more general network topology. Specifically, a two-dimensional (2D) network topology is considered instead of the simple line topology. We further analyze the joint power-location

optimization problem.

1.4   Dissertation Organization

The organization of this dissertation is as follows. We will first investigate the performance of dynamic TDD for spectrum enhancement in a macro-assisted small cell architecture in Chapter 2. In Chapter 3, dynamic 3D beamforming is exploited as a feasible and effective technique for both traffic load balancing and capacity enhancement in the macro-assisted small cell architecture. Then we study the possibility and potential gain of combining full-duplex transmission and cooperative communication to further enhance the spectrum efficiency in Chapter 4. Finally, the concluding remarks are given in Chapter 5.

CHAPTER 2

DYNAMIC TDD SUPPORT IN MACRO-ASSISTED SMALL CELL ARCHITECTURE

In this chapter, we investigate the performance of dynamic TDD in a macrocell-assisted small cell architecture. In Section 2.1, we briefly describe the proposed macrocell-assisted phantom cell architecture and the feasibility of dynamic TDD. For theoretical analysis purposes, the system model is provided in Section 2.2. In Sections 2.3.1 and 2.3.2 we present the basic analytic results on the distribution of the SINR on the UL and DL between an arbitrary UE and its serving BS. The analytic results are verified by system level snapshot simulations. Furthermore, a frequency domain interference coordination technique is proposed in Section 2.4. System level simulation results based on more general and realistic system assumptions are provided in Section 2.5, followed by concluding remarks in Section 2.6.

2.1 Macro-assisted small cell architecture

2.1.1 Phantom cell architecture

Phantom cell is a small cell architecture for enhanced local area networks proposed by DOCOMO [41, 27]. The aim of phantom cell architecture is to provide high system capacity and robust mobility while reducing the cell planning efforts, which is also the goal of local area enhancement for LTE Release 12 onward. One of the key

features for phantom cell architecture is the Control plane/User plane (C-plane/U-plane) Split configuration. According to [27], C-plane is supported by the macrocell layer to maintain good connectivity and mobility using lower existing frequency bands while the U-plane is supported by small cells to provide higher throughput and more flexible and energy efficient operations using higher frequency bands (e.g., 3.5 GHz band), as shown in Fig.2.1.
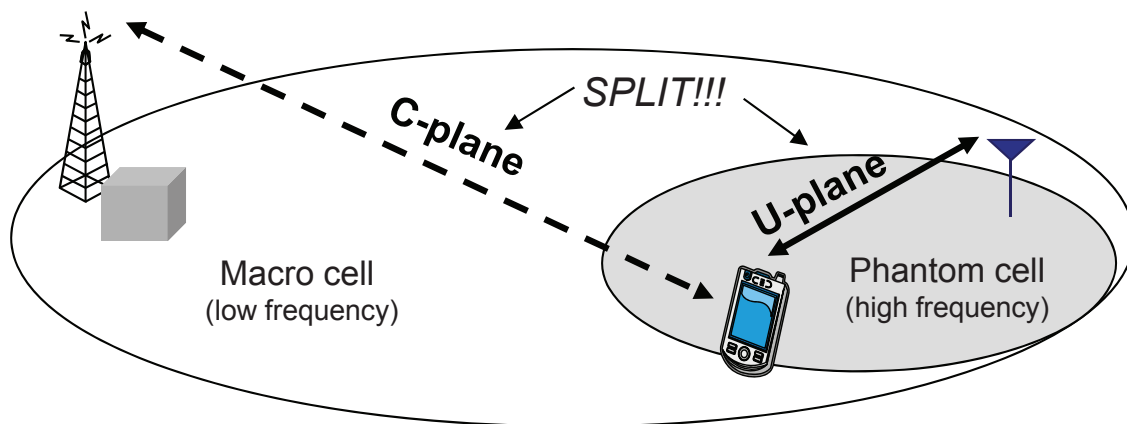
Figure 2.1: C-plane/U-plane Split and Phantom Cell.

However, the small cells are not conventional 'cells' (such as picocells and femtocells) because they are not configured with cell specific signals/channels, i.e., primary/secondary synchronization signals (PSS/SSS), cell-specific reference signals (CRS), master information block/system information blocks (MIB/SIB), etc. Hence they are called Phantom Cells which are only intended to carry user traffic. The Radio Resource Control (RRC) connection procedures between the UE and phantom cells such as channel establishment and release are managed by the macrocells. With such configurations in phantom cells and the assistance from macrocells, the phantom cells are expected to achieve robust mobility, reduction in cell-planning efforts, less interference, and high energy efficiency, etc.

2.1.2 Dynamic TDD

In typical TDD systems, the DL/UL slot assignment is fixed and aligned among the neighboring cells, which is the so-called static and synchronized TDD. Here we focus on dynamic TDD (asynchronized TDD), in which case, for each phantom cell the DL/UL assignment is dynamically changing depending on the traffic, without coordination and time slot synchronization among the phantom cells. It is considered for the following reasons. First, in most user applications, such as web browsing, massive file downloading, and video streaming, the DL/UL traffic is asymmetric and dynamically variable. Dynamic TDD would be more flexible in terms of resource utilization than static TDD. Secondly, in dense small cell deployment scenarios, it would be bothersome to realize complete time synchronization for all small cells. This is because using GPS for each small cell (especially for indoor small cells) would be very costly and thus it is desirable to be able to avoid the time synchronization. Furthermore, in future cellular networks, device-to-device (D2D) communications and small cells may co-exist. Then dynamic TDD would be more realistic in this case. In addition, in the *Phantom Cell* small cell architecture, the dynamic DL/UL slot reconfigurations can be easily realized since there are no (or much less) cell-specific signals/channels. Also the macrocells can assist the phantom cells regarding dynamic interference coordination in a more advanced manner by utilizing the C-plane/U-plane split. So this kind of dynamic and flexible spectrum sharing between DL and UL would be favorable in phantom cells.

2.2 System model

In this section, we present the analytic models and assumptions, based on which the distributions of both DL and UL SINRs are derived in dynamic TDD.

2.2.1 BS and UE Location Model

A certain number of phantom cell BSs are located over each macrocell sector. For a (sufficiently large) deployment, we model the locations of the phantom cell BSs (the tier-1 nodes) and the locations of the UEs (the tier-2 nodes) by the points of two *independent* Poisson Point Process (PPP) [7] Φ_1 and Φ_2 with (constant) intensities λ_1 and λ_2 respectively (in units of nodes per km^2 with $\lambda_2 > \lambda_1$):

1. The number of tier-i nodes $N_i(\mathcal{B})$ in any finite region $\mathcal{B}$ is a Poisson random variable with mean $\lambda_i \times \text{area}(\mathcal{B})$;

2. $\forall \mathcal{B}, \mathcal{B}' : \mathcal{B} \cap \mathcal{B}' = \emptyset \Rightarrow N_i(\mathcal{B}), N_i(\mathcal{B}')$ independent;

3. $\forall \mathcal{B}$, given $N_i(\mathcal{B}) = n$, these n tier-i nodes are *independent identically distributed* over $\mathcal{B}$ uniformly, $i = 1, 2$.

Note that the intensity of the PPP Φ_i applies to the nodes that actively transmit in the band (or over the subcarriers) of interest during the subframe of interest.

2.2.2   BS and UE Activity Model under Dynamic TDD

Any deployment of BSs creates a *Voronoi tessellation* [38] of the plane into *Voronoi cells* with *nuclei* given by the BSs[1]. We assume that each UE is served by the *nearest* BS. Each Voronoi cell containing *at least one* UE, together with the UE(s) within it, forms a *phantom cell* (defined as the geographical area, and all UEs therein, served by a single BS).

We focus on a single LTE subframe in a phantom cell of interest. For analytic tractability, we assume that the starting and ending time of subframes are aligned exactly across the phantom cells although this may not be the case without any time synchronization among the phantom cells. We focus on modeling dynamic TDD with no coordination of the sequences of UL and DL subframes in the radio subframes across the phantom cells. The full-buffer traffic model is assumed so that at any subframe in any phantom cell, there is exactly one active transmission, either on the DL (i.e., from the BS to one UE) with probability $1 - \eta$, or on the UL (i.e., from one UE to the BS) with probability η, using the entire bandwidth.

In other words, at any subframe in any phantom cell, that BS, independently of any other BS, transmits (to some UE in the phantom cell) with probability $1 - \eta$. From the Coloring Theorem [32, (5.1)], this means that the set of *transmitting* BSs at the subframe of interest is described by a PPP $\tilde{\Phi}_1$ with intensity $\tilde{\lambda}_1 = \lambda_1(1 - \eta)$.

The set of transmitting UEs at any subframe under the full buffer assumption is harder to model mathematically because of the constraint that the number of

---

[1]A Voronoi cell with nucleus $b \in \Phi_1$ is the region of $\mathbb{R}^2$ such that all points in this region are closer to b than to any other $b' \in \Phi_1$.

transmitting UEs per phantom cell is either zero (with probability $1-\eta$) or one (with probability η). Instead of modeling this constraint exactly, we propose a model that satisfies this constraint in the mean, i.e., the expected number of transmitting UEs per Voronoi cell is η, as follows: since the mean number of BSs per unit area is λ_1, the mean area of a Voronoi cell is $1/\lambda_1$, hence the mean number of UEs per Voronoi cell is $\mu = \lambda_2/\lambda_1$ (refer to [23] for a more rigourous derivation). If we relax the original constraint and allow every UE, independently of all other UEs, to transmit on the UL with probability η/μ in any subframe, then the mean number of *active* UEs per Voronoi cell at any subframe is η. Though this only approximately models the operation of the phantom cells, it should be accurate if the UE activity is moderate and the probability that a Voronoi cell contains no UE is negligible. Note also that with this model, the Coloring Theorem says that the set of transmitting UEs at the subframe of interest is described by a PPP $\tilde{\Phi}_2$ with intensity $\tilde{\lambda}_2 = \lambda_2\eta/\mu = \lambda_1\eta$.

2.2.3 The UE-to-serving-BS Distance Model

In [56], the cumulative distribution function (CDF) of the distance D^* from an arbitrarily-located UE to its serving BS is calculated for several location models for the UEs and BSs. In particular, when the UE and BS locations are independent PPPs, the CDF is [56, Sec. III.A]

$$\mathbb{P}\{D^* \leq x\} = 1 - \exp(-\pi\lambda_1 x^2),\ x \geq 0. \tag{2.1}$$

In the present work, we are interested in a related, but different random variable

$R_{1,u}$, namely, the distance from an arbitrary BS to a randomly-chosen UE $u \in \Phi_2$ *served by* this BS. Note that by definition, each phantom cell has exactly one nucleus (BS). This induces coupling [19] across cells, such that for two arbitrary UEs u and u', the corresponding distances to their serving BSs, $R_{1,u}$ and $R_{1,u'}$, are *not indepen-dent* (though they are identically distributed). Here, we ignore this dependence and propose the following simple model (see Appendix 2-I): $\{R_{1,u}\}_{u \in \Phi_2}$ are *i.i.d.* with common distribution

$$\mathbb{P}\{R_{1,u} \leq x\} = 1 - \exp(-\pi c \lambda_1 x^2), \ x \geq 0, \quad c = 1.25. \tag{2.2}$$

We use (2.2), instead of (2.1), in the subsequent analysis.
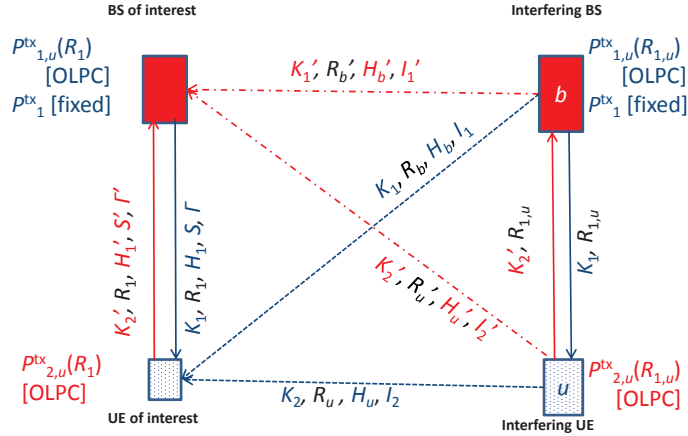
Figure 2.2: Notation for interference and SINR calculation for the link of interest, and one interfering link with BS b and UE u (The solid curves denote the signal part while the dashed curves denote the interference part).

2.2.4   UL and DL Transmit Power Allocation

For the modeling of radio propagation and interference, all relevant parameters and notation are defined in Fig. 2.2 and Table 2.1. Note that the model in Fig. 2.2

Table 2.1: Symbol Notation (quantities pertaining to an uplink, i.e., where the receiver is a BS, are indicated with a prime)

Symbol	Definition
K	The intercepts in linear scale in the path loss model for different links: BS-to-BS (K_1'), BS-to-UE (K_1), UE-to-UE (K_2), UE-to-BS (K_2')
δ	The path loss exponent (slope) in linear scale in the path loss model
R	Distances for different links: BS-to-BS (R_b'), BS-to-UE (R_b), UE-to-UE (R_u), UE-to-BS (R_u') $R_{1,u}$ for distance between an arbitrary UE and its serving BS R_1 for distance between the BS and UE pair of interest
H	Link power gains due to Rayleigh fading for different links: BS-to-BS (H_b'), BS-to-UE (H_b), UE-to-UE (H_u), UE-to-BS (H_u') BS-to-UE (H_1), UE-to-BS (H_1') for the BS-UE pair of interest
I	Total interference power for different interference links: BS-to-BS (I_1'), BS-to-UE (I_1), UE-to-UE (I_2), UE-to-BS (I_2')
S	DL/UL received signal power (S/S')
N_0	Thermal noise power at all receivers
Γ	DL/UL SINR (Γ/Γ')
$P_{2,u}^{\text{tx}}(R_{1,u})$	Transmit power for UE at distance $R_{1,u}$ from its serving BS with OLPC
$P_{1,u}^{\text{tx}}(R_{1,u})$	Transmit power for BS at distance $R_{1,u}$ from its served UE with OLPC
P_1^{tx}	Transmit power for BS with fixed power transmission
θ	Desired received signal at BS with UL OLPC
ζ	Desired received signal at UE with DL OLPC

allows simultaneous interference from both the UE u and its serving BS b. This is prohibited by TDD, which requires *exactly one* transmitter (BS or UE) per phantom cell. We ignore the TDD constraint for tractability, yielding independence of the aggregate interference (at the UE or BS of interest) from other UEs and BSs.

For UL, every UE u at distance $R_{1,u}$ from its serving phantom cell BS applies *open loop power control* (OLPC) to transmit with power $P_{2,u}^{\text{tx}}(R_{1,u})$ such that in the absence of fading and interference, the desired target SINR of θ/N_0 is achieved:

$$K_2' P_{2,u}^{\text{tx}}(R_{1,u})/R_{1,u}^{\delta} = \theta \Leftrightarrow P_{2,u}^{\text{tx}}(R_{1,u}) = (\theta/K_2')R_{1,u}^{\delta}. \qquad (2.3)$$

For DL, we study two alternative modes of operation: (i) fixed power transmission, where every BS transmits with fixed power P_1^{tx}, and (ii) OLPC, where every BS transmits to a served UE u at distance $R_{1,u}$ with power $P_{1,u}^{\text{tx}}$ such that in the absence of fading and interference, the desired target SINR of ζ/N_0 is achieved:

$$K_1 P_{1,u}^{\text{tx}}(R_{1,u})/R_{1,u}^\delta = \zeta \Leftrightarrow P_{1,u}^{\text{tx}}(R_{1,u}) = (\zeta/K_1)R_{1,u}^\delta. \tag{2.4}$$

2.2.5 Interference Modeling

Based on the previous models and assumptions, we model the interference in dynamic TDD in this section. The symbols denoting interference to UL transmission are indicated with a prime.

2.2.5.1 Interference from UL Transmissions

From the discussion in Sec. 2.2.2, the notation of Fig. 2.2, and the constraint $R_{1,u} < R'_u$ for all $u \in \tilde{\Phi}_2$ (which is resulted from the assumption that each UE is served by its nearest BS), we obtain

$$
\begin{aligned}
I'_2 &\approx \sum_{u \in \tilde{\Phi}_2 : R'_u > R_{1,u}} \frac{K'_2 P_{2,u}^{\text{tx}} H'_u}{(R'_u)^\delta} = \sum_{u \in \tilde{\Phi}_2} \theta \left(\frac{R_{1,u}}{R'_u} \right)^\delta 1\{R_{1,u} < R'_u\} H'_u, & (2.5) \\
I_2 &\approx \sum_{u \in \tilde{\Phi}_2} \frac{\theta K_2}{K'_2} H_u \left(\frac{R_{1,u}}{R_u} \right)^\delta. & (2.6)
\end{aligned}
$$

2.2.5.2   Interference from Fixed Power DL Transmissions

Using the notation of Fig. 2.2, and the constraint that $R_b > R_1$ for all $b \in \tilde{\Phi}_1$, we have

$$I_1(R_1) \quad = \quad \sum_{b \in \tilde{\Phi}_1 : R_b > R_1} \frac{K_1 P_1^{\text{tx}} H_b}{R_b^{\delta}}, \tag{2.7}$$

$$I_1' \quad = \quad \sum_{b \in \tilde{\Phi}_1} \frac{K_1' P_1^{\text{tx}} H_b'}{(R_b')^{\delta}}. \tag{2.8}$$

2.2.5.3   Interference from DL Transmissions with OLPC

Similar to the derivations of (2.7) and (2.8), we can obtain

$$I_1(R_1) \quad = \quad \sum_{b \in \tilde{\Phi}_1} \zeta \left(\frac{R_{1,u}}{R_b} \right)^{\delta} 1\{R_b > R_1\} H_b, \tag{2.9}$$

$$I_1' \quad = \quad \sum_{b \in \tilde{\Phi}_1} \frac{\zeta K_1'}{K_1} \left(\frac{R_{1,u}}{R_b'} \right)^{\delta} H_b'. \tag{2.10}$$

2.3   SINR Distributions

In this section, we present the main analytic results for SINR distributions on the DL and UL in dynamic TDD.

2.3.1   Distribution of UL SINR

From (2.3), the received power at the phantom cell BS of interest from the UE of interest is

$$S' = \theta H_1', \ H_1' \sim \text{Exp}(1). \tag{2.11}$$

From (2.11), it follows that the UL SINR is

$$\Gamma' = \frac{S'}{I_1' + I_2' + N_0} = \frac{\theta H_1'}{I_1' + I_2' + N_0}, \tag{2.12}$$

where I_2' is given by (2.5), and I_1' is given by (2.8) and (2.10) when phantom cell BSs transmit with fixed power and OLPC, respectively. Note that the SINR Γ' does not depend on the distance R_1.

Lemma 2.1 *The Laplace Transform of I_1' is*

$$\mathcal{L}_{I_1'}(s) = \begin{cases} \exp\left[-\frac{\pi\lambda_1(1-\eta)}{\operatorname{sinc}(2/\delta)}\left(K_1' P_1^{\mathrm{tx}} s\right)^{2/\delta}\right], & \text{if fixed transmit power is adopted on DL} \\ \exp\left[-\frac{(1-\eta)}{c\operatorname{sinc}(2/\delta)}\left(\frac{s\zeta K_1'}{K_1}\right)^{2/\delta}\right], & \text{if OLPC is adopted on DL} \end{cases} \tag{2.13}$$

where $\operatorname{sinc}(x) = \sin(\pi x)/(\pi x)$.

Proof. For fixed DL transmit power, the Lapalace transform of I_1' can be obtained from (2.8) and [49, eqn. (23)]. For DL OLPC, the Lapalace transform of I_1' can be obtained using (2.28) with $(\Psi, \lambda, \alpha, \epsilon, d) = (\tilde{\Phi}_1, \tilde{\lambda}_1, \zeta K_1'/K_1, 0, 0)$ and [25, 3.194.6, p. 313]. ∎

Lemma 2.2 *The Laplace Transform of I_2' is*

$$\mathcal{L}_{I_2'}(s) = \exp\left\{-\frac{s\theta\eta}{c}\left[-\frac{1}{1+s\theta} + \frac{1}{1-\frac{2}{\delta}} \times {}_2F_1\left(2, 1-\frac{2}{\delta}; 2-\frac{2}{\delta}; -s\theta\right)\right]\right\}, \tag{2.14}$$

where ${}_2F_1(a,b;c;z) = 1 + \sum_{k=1}^{\infty}\frac{z^k}{k!}\prod_{l=0}^{k-1}\frac{(a+l)(b+l)}{c+l}$ *is the Hypergeometric Function.*

19

Proof. From (2.28), with $(\Psi, \lambda, \alpha, \epsilon, d) = (\tilde{\Phi}_2, \tilde{\lambda}_2, \theta, 1, 0)$, the Lapalace transform of I_2' can be obtained using [25, 3.194.1, p. 313]. ∎

When $\delta = 4$, we use the identity (2.29) (see Appendix 2-III) to simplify (2.14) to get

$$\mathcal{L}_{I_2'}(s) = \exp[-(\eta/c)\sqrt{s\theta}\tan^{-1}\sqrt{s\theta}], \, \delta = 4. \tag{2.15}$$

Thoerem 2.1 *The complementary cumulative distribution function (CCDF) of UL SINR can be obtained by*

$$\mathbb{P}\{\Gamma' > \gamma'\} = \mathbb{E}\exp\left[-\frac{\gamma'}{\theta}(I_1' + I_2' + N_0)\right] = \mathrm{e}^{-sN_0}\mathcal{L}_{I_1'}(s)\mathcal{L}_{I_2'}(s)\big|_{s=\gamma'/\theta}. \tag{2.16}$$

Proof.

$$\begin{aligned}
\mathbb{P}\{\Gamma' > \gamma'\} &= \mathbb{P}\left\{H_1' > \frac{\gamma'}{\theta}[I_1(r_1) + I_2 + N_0]\right\} \\
&\overset{(a)}{=} \mathbb{E}\exp\left[-\frac{\gamma'}{\theta}(I_1' + I_2' + N_0)\right] = \mathrm{e}^{-sN_0}\mathcal{L}_{I_1'}(s)\mathcal{L}_{I_2'}(s)\big|_{s=\gamma'/\theta},
\end{aligned}$$

where (a) follows from the exponential distribution of H_1'. Then based on Lemma 2.1 and Lemma 2.2, the closed form expression for the CCDF of UL SINR can be obtained.

∎

2.3.2 Distribution of DL SINR

2.3.2.1 Distribution of SINR with Fixed DL Transmit Power

The received *signal* power at the UE of interest from its serving phantom cell BS (at a distance of R_1) is $S(R_1) = K_1 P_1^{\text{tx}} H_1 / R_1^\delta$. The SINR at the UE of interest, conditioned on $R_1 = r_1$, is given by

$$\Gamma(r_1) = \frac{S(r_1)}{I_1(r_1) + I_2 + N_0}.$$

Lemma 2.3 *The Laplace Transform of $I_1(r_1)$ is*

$$\mathcal{L}_{I_1(r_1)}(s) = \exp\left[-\pi\lambda_1(1-\eta)(K_1 P_1^{\text{tx}})^{2/\delta} s^{2/\delta} \times G_{2/\delta}\left(\frac{r_1^2}{(K_1 P_1^{\text{tx}})^{2/\delta} s^{2/\delta}} \right) \right], \quad (2.17)$$

where for any $\beta \in (0,1)$, $G_\beta(z) = \int_z^\infty \mathrm{d}x/(1+x^{1/\beta})$, $z \geq 0$:

$$G_\beta(z) = \begin{cases} \cot^{-1} z, & \beta = 1/2, \quad z \geq 0, \\[2mm] \pi\beta/\sin(\pi\beta) = 1/\text{sinc}(\beta), & z = 0, \\[2mm] \dfrac{\beta z \, _2F_1\left(1,1;2-\beta;[1+z^{\frac{1}{\beta}}]^{-1}\right)}{(1-\beta)(1+z^{\frac{1}{\beta}})}, & z > 0. \end{cases}$$

Proof. From (2.7) and [49, eqns. (23), (24)], (2.17) can be obtained. ∎

Lemma 2.4 *The Laplace Transform of I_2 is*

$$\mathcal{L}_{I_2}(s) = \exp\left[-\frac{\eta}{c\,\text{sinc}(2/\delta)}\left(\frac{s\theta K_2}{K} \right)^{2/\delta} \right]. \quad (2.18)$$

Proof. Using (2.6) and (2.28) with $(\Psi, \lambda, \alpha, \epsilon, d) = (\tilde{\Phi}_2, \tilde{\lambda}_2, \theta K_2/K_2', 0, 0)$, (2.18) can be obtained. ∎

Thoerem 2.2 *The unconditional CCDF of DL SINR at an arbitrary UE located at least a distance of $d_{\min}$ from its serving phantom cell BS, and at most a distance of $d_{\max}$ from it, can be found by*

$$\mathbb{P}\{\Gamma > \gamma, d_{\min} \leq R_1 \leq d_{\max}\} = \int_{d_{\min}}^{d_{\max}} 2\pi c \lambda_1 r_1 \mathrm{e}^{-(sN_0 + \pi c \lambda_1 r_1^2)} \mathcal{L}_{I_1(r_1)}(s) \mathcal{L}_{I_2}(s) \, \mathrm{d}r_1,$$
(2.19)

where $s = \gamma r_1^\delta/(K_1 P_1^{\mathrm{tx}})$.

Proof. The CCDF of the DL SINR, conditioned on $R_1 = r_1$, is given by

$$\mathbb{P}\{\Gamma(r_1) > \gamma\} = \mathrm{e}^{-sN_0} \mathcal{L}_{I_1(r_1)}(s) \mathcal{L}_{I_2}(s) \big|_{s=\gamma r_1^\delta/(K_1 P_1^{\mathrm{tx}})}. \tag{2.20}$$

Then the unconditional CCDF of the DL SINR can be obtained by averaging over the distribution of R_1:

$$\mathbb{P}\{\Gamma > \gamma, d_{\min} \leq R_1 \leq d_{\max}\} = \int_{d_{\min}}^{d_{\max}} \mathbb{P}\{\Gamma(r_1) > \gamma\} f_{R_1}(r_1) \, \mathrm{d}r_1, \tag{2.21}$$

where R_1 has the distribution (2.2). Based on Lemma 2.3 and Lemma 2.4, the analytic expression for the unconditional CCDF of DL SINR can be obtained. ∎

Collarory 2.1 *If thermal noise is negligible ($N_0 = 0$), the unconditional CCDF of*

DL SINR is given by

$$\mathbb{P}\{\Gamma > \gamma\} = \frac{e^{-\pi c\lambda_1 d_{\min}^2 A(\gamma)} - e^{-\pi c\lambda_1 d_{\max}^2 A(\gamma)}}{A(\gamma)}, \tag{2.22}$$

where

$$A(\gamma) = 1 + (\gamma^{2/\delta}/c)\{(1-\eta)G_{2/\delta}(\gamma^{-2/\delta}) + \eta/[\pi\lambda_1 c\operatorname{sinc}(2/\delta)][\theta K_2/(K_2' K_1 P_1^{\mathrm{tx}})]^{2/\delta}\}.$$

Collarory 2.2 *When $\delta = 4$, $N_0 > 0$, $d_{\min} = 0$, $d_{\max} = \infty$, the unconditional CCDF of DL SINR is given by*

$$\mathbb{P}\{\Gamma > \gamma\} = \int_0^\infty \exp[-A(\gamma)v - B(\gamma)v^2]\,\mathrm{d}v = \frac{\sqrt{\pi}}{2\sqrt{B(\gamma)}}\exp\left[\frac{A(\gamma)^2}{4B(\gamma)}\right]\operatorname{erfc}\left(\frac{A(\gamma)}{2\sqrt{B(\gamma)}}\right), \tag{2.23}$$

where $B(\gamma) = \gamma N_0/[(\pi\lambda_1 c)^2 K_2' P_1^{\mathrm{tx}}]$, and $\operatorname{erfc}(x) = (2/\sqrt{\pi})\int_x^\infty \exp(-t^2)\,\mathrm{d}t$ is the complementary error function.

2.3.2.2 Distribution of SINR with DL OLPC

From (2.4), the received power at the UE of interest is

$$S = \zeta H_1,\ H_1 \sim \operatorname{Exp}(1). \tag{2.24}$$

The DL SINR is therefore

$$\Gamma(R_1) = \frac{\zeta H_1}{I_1(R_1) + I_2 + N_0}.$$

23

Table 2.2: Simulation Parameters

Parameter	Value	Description
BW	5 MHz	System bandwidth
RB	25	Number of resource blocks
N_0	-174 dBm/Hz	Thermal noise spectral density
NF	5 dB	Noise figure
NS	6 dB	Interference margin for OLPC
$SINR_t$	0.33 dB	Target SINR for OLPC
Path Loss	$140.7 + 40\log_{10}(d)$	Path loss in dB, d in km
Fast Fading	$H \sim \mathrm{Exp}(1)$	All links are i.i.d. Rayleigh
ISD	500 m	Inter macro site dist. (hex. grid)
N_1	4 per macro sector	Number of phantom cells
N_2	80 per macro sector	Number of UEs

Thus the CCDF of this SINR conditioned on $R_1 = r_1$ is

$$\mathbb{P}\{\Gamma(r_1) > \gamma\} = \mathrm{e}^{-sN_0}\mathcal{L}_{I_1(r_1)}(s)\mathcal{L}_{I_2}(s)\,\big|_{s=\gamma/\zeta}\,. \tag{2.25}$$

Here, $I_1(R_1)$ is given by (2.9). From (2.28) with $(\Psi, \lambda, \alpha, \epsilon, d) = (\tilde{\Phi}_1, \tilde{\lambda}_1, \zeta, 0, r_1)$, we obtain

$$\mathcal{L}_{I_1(r_1)}(s) = \exp\left[-\frac{s\zeta(1-\eta)}{c}\int_0^\infty \frac{\exp\left(-\pi c\lambda_1 r_1^2 y^{2/\delta}\right)}{y^{2/\delta}(1+s\zeta y)^2}\,\mathrm{d}y\right]. \tag{2.26}$$

Substituting (2.26) into (2.25), using (2.18) then evaluating (2.19) numerically gives the DL SINR CCDF.

2.3.3 Numerical Results

In this section, simulation results are provided to verify the analytic results. The SINR performance under dynamic TDD for different levels of asynchronism in the phantom cell network is investigated. System level snapshot simulations are conducted with the full buffer traffic model. Phantom cells and UEs are deployed inde-

pendently and uniformly in a regular 19-cell wrap-around hexagonal grid. At each snapshot, one UE in each phantom cell is chosen at random for communication, either on DL (with probability $1 - \eta$) or UL (with probability η). UEs employ OLPC while for DL transmission, both fixed transmit power and OLPC are considered. Shadow fading is not simulated for simplicity. The other simulation parameters are provided in Table 2.2. The corresponding analytic parameters are $\theta = \zeta = -96.14$ dBm, and $\lambda_1 = 8\sqrt{3}/(ISD)^2$.

2.3.3.1 Fixed DL Transmit Power

(a) 23 dBm, DL   (b) 23 dBm, UL
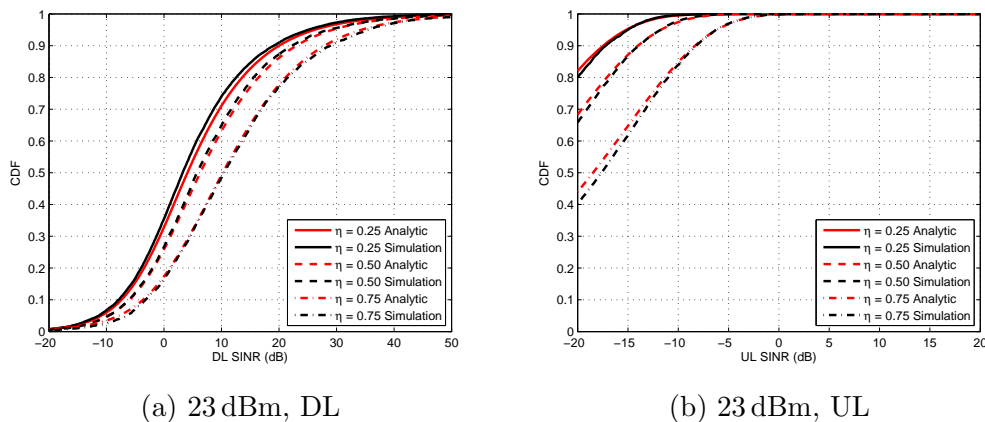
Figure 2.3: SINR comparisons for different η when DL transmissions have fixed power of 23 dBm.

In Figs. 2.3a and 2.3b we plot both simulation and analytic results for DL and UL SINR CDFs for several choices of η when all BSs transmit with fixed power of 23 dBm, which is in the range of picocell transmit powers. It is seen that the analytic results match the simulations quite well.[2] For this value of DL transmit power, we observe that DL-to-DL interference is strong, accounting for the improvement of both

---

[2]Note that the SINR outages are higher than desirable for LTE operation. This is a consequence of the assumption of full buffer traffic and no minimum coupling loss between BSs.

DL and UL SINR as η increases, i.e., there are fewer DL and more UL transmissions. However, the UL SINR is poor, as seen in Fig. 2.3b. This is because on the UL, the DL-to-UL interference is more severe than the UL-to-UL interference since the DL has fixed transmit power and we have imposed no minimum distance constraint between phantom cell BSs.

(a) 5 dBm, DL

(b) 5 dBm, UL
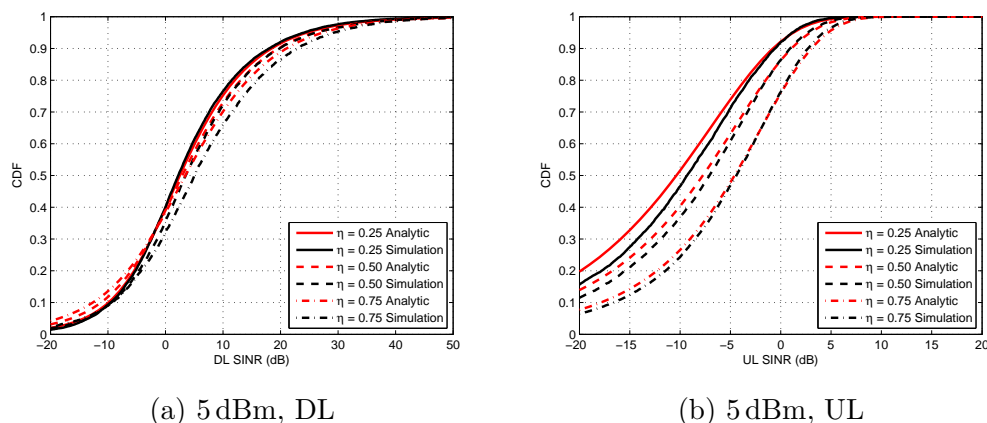
Figure 2.4: SINR comparisons for different η when DL transmissions have fixed power of 5 dBm.

One way to improve the UL SINR is to decrease the DL transmit power. In Figs. 2.4a and 2.4b, we plot the same curves when DL transmit power is fixed at 5 dBm. In Fig. 2.4a, we observe a crossover of the DL SINR CDF curves for different η. The reason for this is that with the reduced DL transmit power, the DL-to-DL interference no longer dominates the UL-to-DL interference. Note that the UL-to-DL interference can be strong since the UEs can be close to each other. With the reduction in DL transmit power from 23 dBm to 5 dBm, we observe from Fig. 2.4b that the degradation of UL SINR is mitigated as η increases, but is still significant. In the actual network operations, however, it may be quite cumbersome to optimize the fixed DL transmit power cell by cell or case by case to mitigate interference problems.

Path loss based OLPC on DL transmission might be another option to improve the UL SINR, as studied next.

2.3.3.2 OLPC on DL

(a) OLPC, DL   (b) OLPC, UL
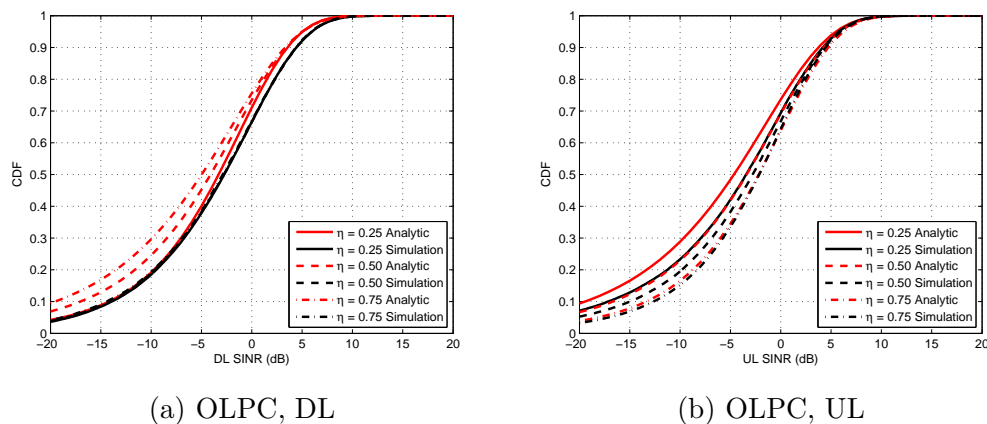
Figure 2.5: SINR comparisons for different η when DL transmissions have OLPC.

As mentioned in Section 2.1, a key feature of the phantom cell architecture is that since there are no cell-specific signal transmissions by the BSs, autonomous dynamic DL power control in each phantom cell is feasible and easily implementable. In Figs. 2.5a and 2.5b we plot the simulation and analytic results for DL and UL SINR CDFs for several choices of η when all DL transmissions employ OLPC. Compared with the DL fixed transmit power case, the UL SINR performance is improved greatly while the DL SINR performance is degraded to some extent. This is because with OLPC on DL, both the DL-to-UL interference and desired DL signal power are decreased compared to the fixed DL transmit power case. We also note that with OLPC, the DL SINR range decreases compared to the fixed transmit power case. This degradation in DL SINR may result in DL throughput loss, which will be investigated more carefully in the following dynamic system level simulations. Similar to

the fixed DL power case, the analytic results follow the simulation results reasonably well for UL while for DL they are less accurate for higher η due to the approximation in (2.6).

2.4   Proposed interference coordination method for dynamic TDD

We have observed that the ICI poses such severe challenges that interference coordination methods are required in order to make dynamic TDD feasible. In this paper, we focus on the frequency domain inter-cell interference coordination (ICIC) techniques. One of the most classic techniques is frequency reuse. By frequency reuse factor of more than 1, it is expected that the inter-cell interference can be mitigated to some extent. Thus we will use the frequency reuse technique as a benchmark for frequency domain ICIC. We further propose a half-duplex FDD-like radio resource assignment technique in this section.

2.4.1   Proposed half-duplex FDD-like ICIC
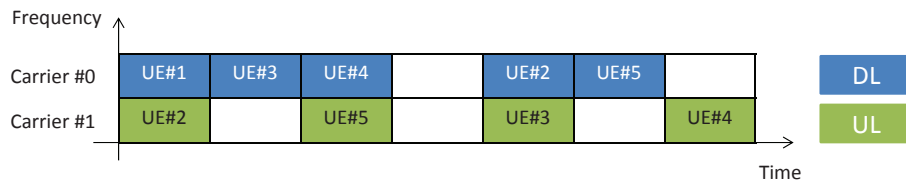
Figure 2.6: An example of half-duplex FDD-like radio resource assignment in TDD band.

In half-duplex FDD-like radio resource assignment technique, the total system bandwidth is divided into a certain number of carriers. The basic idea is that DL and UL transmissions take place on distinct carriers such that the DL-to-UL and

UL-to-DL interference can be mitigated. Note that the DL-to-UL interference is the dominating interference which results in poor UL performance in dynamic TDD. Specifically, DL and UL transmissions can take place at the same subframe at BSs. However, for one particular UE, at one subframe, only DL or UL transmission can be scheduled. The number of carriers for DL and UL (partition of frequency resources for DL and UL) can be configured flexibly and dynamically based on the traffic load. A simple example of the scheme for one particular phantom cell is shown in Fig.2.6. In this example, the system bandwidth is divided into two carriers. Each cell uses both carriers with DL only on carrier 0 and UL only on carrier 1 at the same subframe. For one particular UE, at one subframe, it can use either DL or UL resource, but not both. For example, UE 1 and UE 2 are scheduled at the first subframe, with UE 1 on the DL and UE 2 on the UL. Basically, the half-duplex FDD-like technique can be regarded as a hybrid combination of TDD and FDD. It is noted that, the base station is full-duplex while the UEs are half-duplex. Compared to full duplex FDD, half-duplex FDD has the advantage that there will be no need for duplexer for the UEs, thus conventional TDD UEs can be used for both TDD system and the proposed half-duplex FDD-like operation system. It should also be noted that there may be some spacing needed between the two carriers (which is not shown in the Fig.2.6). The spacing is related to the adjacent channel interference ratio (ACIR), which may affect the system performance, as we shall see in the simulation evaluations.

With this half-duplex FDD-like scheme, for the UL SINR calculation in (2.12), I_1' becomes the inter-carrier DL-to-UL interference instead of intra-carrier DL-to-

UL interference as in the case of dynamic TDD without ICIC. Similarly, for DL, the intra-carrier UL-to-DL interference becomes inter-carrier UL-to-DL interference. The inter-carrier interference is effectively attenuated by ACIR (which takes into account both adjacent-carrier-leakage ratio (ACLR) and adjacent channel selectivity (ACS)) compared to intra-carrier interference. For example, the UE ACLR and ACS are specified as 30 dB and 33 dB, respectively, in [4].

2.4.2 Feasibility of half-duplex FDD-like ICIC for phantom cell architecture

The half-duplex FDD-like scheme is suitable for phantom cells for the following reasons. Firstly, since there is no (or much less) system information (broadcast signals) or paging signals in phantom cells, it increases the scheduling flexibility of half-duplex FDD. If a UE has to receive such important DL signals, then it can not transmit UL packet in the queue at the same subframe due to the characteristics of half-duplex FDD. Secondly, the partition of DL and UL frequency resources (e.g., the number of carriers and the bandwidth of each carrier) can be easily adjusted according to the traffic load. This is because the phantom cells can have flexible transmission/reception bandwidth due to the characteristics of having no (or much less) cell-specific channels/signals such as PSS/SSS, CRS, MIB/SIB, etc. That is, if DL traffic is heavier than UL traffic, the partition of DL and UL frequency frequency resources can be adjusted with the assistance of macrocells so that the DL bandwidth can be larger than the UL bandwidth. This is very beneficial in terms of handling asymmetric and dynamic DL/UL traffic.

Table 2.3: Simulation Parameters

Parameter	Value
Carrier frequency	3.5 GHz
System bandwidth	10 MHz in total, 5 MHz per carrier
Inter macro site distance	500 m (3GPP case 1)
Phantom cell layout	Uniformly and randomly distributed
Number of resource blocks	50
Thermal noise spectral density	-174 dBm/Hz
Noise figure	5 dB
Phantom BS TX power	24 dBm for 10 MHz
Interference margin for OLPC	6 dB
Target SINR for OLPC	0.33 dB
Antenna gain	0 dBi (UE)/ 5 dBi (Phantom BS)
ACIR	30 dB specified in Section 12.1.3 in [3]
Path Loss model	Urban Micro in Table A1-2 in [29]
Fast Fading	6-ray Typical Urban
Lognormal shadowing	All links are correlated with coefficient 0.5
Penetration Loss	0 dB
Number of phantom cells	4 per macro sector
Number of UEs	40 per macro sector
Antennas	1TX / 2RX
Aadaptive modulation and coding	6 ms feedback delay with transport formats specified in [2]
Hybrid automatic repeat request	8 ms round trip delay with chase combining
Traffic model	FTP Model 1 in [1]
Scheduler	Round robin

2.5   System level simulations

System level dynamic simulations are conducted to evaluate the performance of dynamic TDD and our proposed frequency domain ICIC technique with the partial load traffic model taken into consideration. Table 2.3 lists the detailed simulation parameters. The simulation setup, results and analysis are provided as follows.

2.5.1 Simulation setup

2.5.1.1 System deployment

We consider a regular 19-macrocell hexagonal grid area (with each macrocell serving 3 sectors). 4 phantom cells and 40 UEs are independently and uniformly distributed in each macro sector. Since the conventional macrocells operate in 2 GHz and we assume that the carrier frequency for phantom cells is 3.5 GHz, there is no interference between conventional macrocells and the phantom cells. We will focus on the phantom cells. Omni-directional antenna pattern is assumed for each of the phantom cells with antenna gain of 5 dBi. The UEs are assumed to be static with a maximum Doppler shift of 10 Hz. The total system bandwidth is 10 MHz. For frequency domain ICIC, the total 10 MHz is partitioned into 2 carriers (5 MHz each). A frequency reuse factor of 2 is implemented assuming that each phantom cell only uses one carrier and two closest neighboring cells should use different carriers. For the half-duplex FDD-like scheme, one carrier is used only for DL and the other one for UL for each phantom cell. Note that for the purpose of simplicity of the system level simulations, the time slot boundaries are aligned across the phantom cells and we mainly would like to investigate the effect of BS-to-BS and UE-to-UE interference.

2.5.1.2 DL and UL transmit power allocation

For UL, every UE at distance $R_{1,u}$ applies OLPC to transmit with power $P_{2,u}^{tx}(R_{1,u})$ as follows:

$$P_{2,u}^{tx}(R_{1,u}) = SINR_t + PL(R_{1,u}) + N_0 + N_s, \tag{2.27}$$

where $SINR_t$ is the target SINR for OLPC, $PL(R_{1,u})$ is the distance based path loss and lognormal shadowing, N_0 is the thermal noise power, and N_s is the interference margin for OLPC (all in dB). For DL, since phantom cells can support flexible DL power control with removal of cell specific signals, two alternative modes of operation are considered: (i) fixed power transmission, where every BS transmits with fixed power P_1^{tx} (same fixed power per bandwidth), and (ii) OLPC, which is similar to the UL OLPC case.

(a) UL SINR   (b) DL SINR
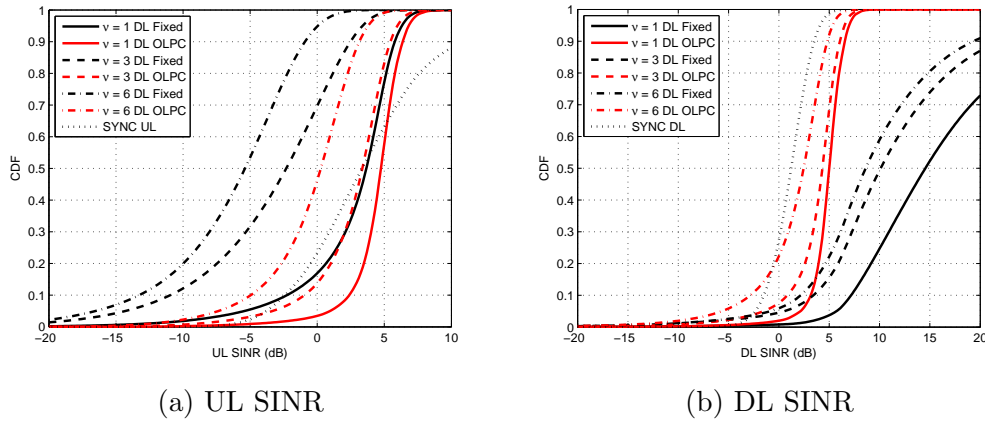
Figure 2.7: SINR comparisons for different ν between DL fixed and DL OLPC.

2.5.1.3   Path loss model

The path loss model for scenario Urban Micro (UMi) in Table A1-2 in [29] is adopted. Specifically, we consider two different propagation scenarios. In the first scenario, all links are NLOS (Non-Line-of-Sight). In the second scenario, both NLOS and LOS are considered with LOS probability specified in Table A1-3 in [29]. We aim to study the effect of NLOS and LOS on the performance of dynamic TDD.

2.5.2 Simulation results and analysis

2.5.2.1 Dynamic TDD without ICIC in NLOS
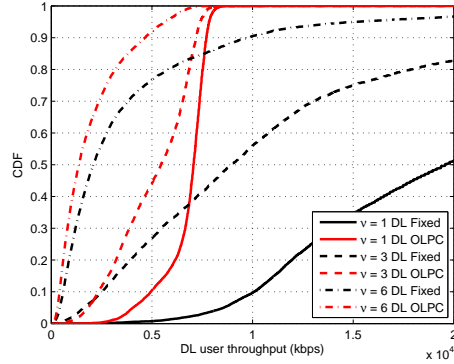
Figure 2.8: DL user throughput comparison for different ν between DL fixed and DL OLPC.

The SINR performance comparisons between fixed DL and OLPC DL with different traffic levels in NLOS are shown in Fig. 2.7. We include the results from synchronized TDD systems (DL fixed, UL OLPC with full buffer traffic) for reference. Fig. 2.7a shows that compared with DL OLPC case, the UL SINR in fixed DL case suffers from significant degradation, especially when the traffic load is high ($\nu = 6$), but the DL SINR shows better performance. The poor UL SINR performance is resulted from the fact that under dynamic TDD, the UL transmission may encounter interference from the DL transmissions (BS-to-BS interference) and this interference would be very strong when the DL is transmitting with fixed transmit power. For DL OLPC, the UL SINR seems acceptable compared with the reference UL SINR, especially at low traffic load levels ($\nu = 1$). However, this is achieved at the cost of degradation in DL user throughput, as shown in Fig. 2.8. The DL user throughput is degraded significantly by using OLPC compared with using fixed transmit power in

DL. So dynamic TDD without any interference coordination is problematic in either fixed DL transmit power case or DL OLPC case.

2.5.2.2 Dynamic TDD without ICIC in both NLOS and LOS

(a) DL fixed   (b) DL OLPC
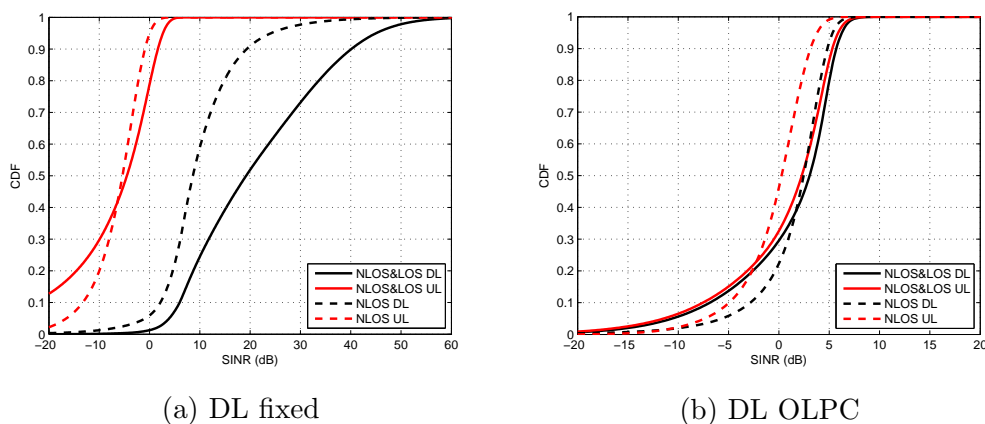
Figure 2.9: SINR comparisons for $\nu = 6$ between NLOS and NLOS+LOS.

The SINR comparisons between the two propagation scenarios with both fixed DL and OLPC DL for $\nu = 6$ are shown in Fig. 2.9. As depicted in Fig. 2.9a, with fixed DL transmit power, the DL SINR in the scenario with both NLOS and LOS is improved significantly. This is because the received power is improved since the link between each UE and its serving BS is highly possible to be in LOS condition (due to short distance range). However, with OLPC adopted (on either DL or UL), we observe performance degradation in the lower SINR region in the scenario with both NLOS and LOS. This SINR degradation is caused by the effect of NLOS and LOS on interference. Specifically, it is possible that the link between a UE at cell edge and its serving BS is in NLOS condition while some of the interference links are in LOS condition (for example, the interference links between the UE and some interfering UEs at the cell edge of the neighboring cells). In this case, the interference would be

35

stronger than the interference in the scenario with only NLOS links. On the other hand, since it is highly possible that the link between each UE and its serving BS is in LOS condition, the transmit power with OLPC would be lower, which will cause less interference especially to the UEs near their serving BSs. This results in the SINR improvement in the higher SINR region in the scenario with both NLOS and LOS. So it is evident that the performance of dynamic TDD can be affected significantly by the propagation model.

2.5.2.3 Dynamic TDD with frequency domain ICIC

(a) $\nu = 1$ (b) $\nu = 6$
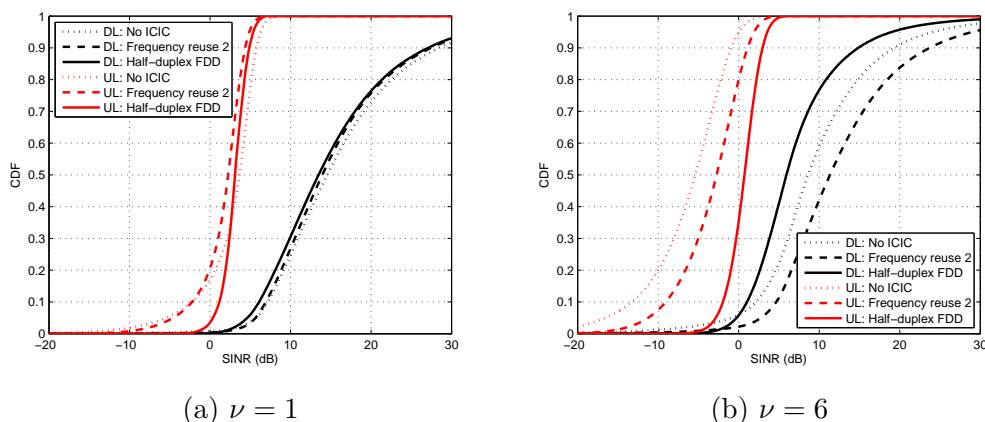
Figure 2.10: SINR comparisons for different interference coordination methods.

The SINR comparisons in low traffic ($\nu = 1$) and high traffic ($\nu = 6$) scenarios for dynamic TDD without ICIC and with two different frequency domain ICIC techniques in NLOS are shown in Fig. 2.10. The DL transmit power is fixed here and 30 dB ACIR is adopted for the proposed half-duplex FDD-like ICIC scheme. In this case, the DL is not a problem and the UL is the bottleneck for dynamic TDD. It is seen obviously that in both traffic scenarios, the half-duplex FDD-like radio resource assignment technique provides very good UL SINR performance even with fixed DL transmit

power while both dynamic TDD without ICIC and dynamic TDD with frequency reuse suffer in the UL SINR. Note that the frequency reuse 2 method can also improve the UL SINR to some extent, but not very significantly. The UL SINR comparisons for dynamic TDD without ICIC and with half-duplex FDD-like ICIC in different propagation scenarios are shown in Fig. 2.11. We observe that half-duplex FDD-like ICIC can greatly improve the poor UL SINR even in the scenario with both NLOS and LOS.

(a) $\nu = 1$ (b) $\nu = 6$

Figure 2.11: UL SINR comparisons for NLOS and NLOS+LOS with and without ICIC.

(a) $\nu = 1$ (b) $\nu = 6$

Figure 2.12: SINR comparisons for different ACIR values.

For the half-duplex FDD-like radio resource assignment, the SINR comparisons

for different ACIR values and for both low and high traffic load are shown in Fig. 2.12. We see that the effect of ACIR to DL SINR performance in both low and high traffic cases is almost negligible. On the other hand, as ACIR decreases, the UL SINR performance is degraded, especially for high traffic load case. This is because for DL, the intra-carrier DL-to-DL interference is dominant while the inter-carrier DL-to-UL interference is dominant for UL. So with ACIR introduced between two different carriers, it has more effect on the inter-carrier DL-to-UL interference. Thus UL SINR is affected more by ACIR, as shown in the results.

2.6 Conclusions

In this paper, the performance of dynamic TDD in phantom cells has been studied. Both analytic and simulated results for the SINR distributions have been presented and shown to match reasonably well. We also observe from the results that UL performs worse than DL in terms of SINR when DL uses fixed transmit power. A novel frequency domain ICIC technique, namely, the half-duplex FDD-like radio resource assignment scheme has been proposed to mitigate the ICI. System level simulations were conducted to evaluate the performance of dynamic TDD and the proposed ICIC scheme under different propagation scenarios, traffic load levels and ACIR settings. Simulation results demonstrate that the performance of dynamic TDD can be affected significantly by the propagation model. Also remarkable performance improvement especially on UL with fixed DL transmit power can be achieved even under very high traffic load conditions with the proposed ICIC scheme. It is noted that this UL

performance improvement can be largely affected by ACIR.

Appendix 2-I: The eLA BS to UE Distance Distribution Model

For identically distributed $\{R_{1,u}\}_{u\in\Phi_2}$, the common CDF is estimated empirically from the following experiment $\mathcal{S}$:

1. For each of a large number of independent deployments of (not too few) eLA BSs and (many) UEs located i.i.d. uniformly over a (fixed) sufficiently large region, do:

2. For each Voronoi cell with at least one UE in it, choose one of these UEs at random and compute its distance from the nucleus (BS) of this Voronoi cell.

3. Finally, compute the empirical CDF of all the distance samples obtained from the above steps.
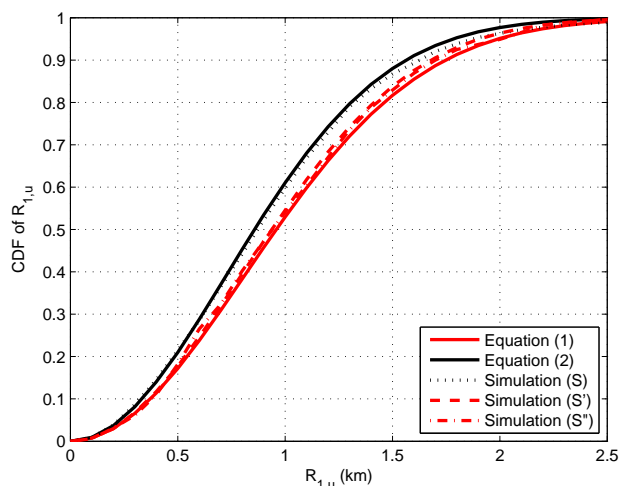
Figure 2.13: Plot of the empirical CDF from method $\mathcal{S}$, for deployments of BSs and UEs on a large square. It is seen to be well approximated by (2.2). Also shown is the theoretical CDF (2.1) of D^*, which is closely matched by two empirical CDFs from distance samples collected using methods $\mathcal{S}'$ and $\mathcal{S}''$ respectively.

We now make the following observations:

- The empirical CDF calculated in step 3 above should not be expected to converge to the marginal CDF (2.1) because these are the distributions of two different random variables. However, these two random variables are closely related, as follows:

- Changing 'one of these UEs at random' in step 2 to 'all these UEs,' the empirical CDF from the new experiment $\mathcal{S}'$ does converge to (2.1). Also, $\mathcal{S}'$ is equivalent to (but more efficient than) the experiment $\mathcal{S}''$ where we simply collect the distance of the nearest BS to the origin (an 'arbitrary point in the plane') instead of step 2.
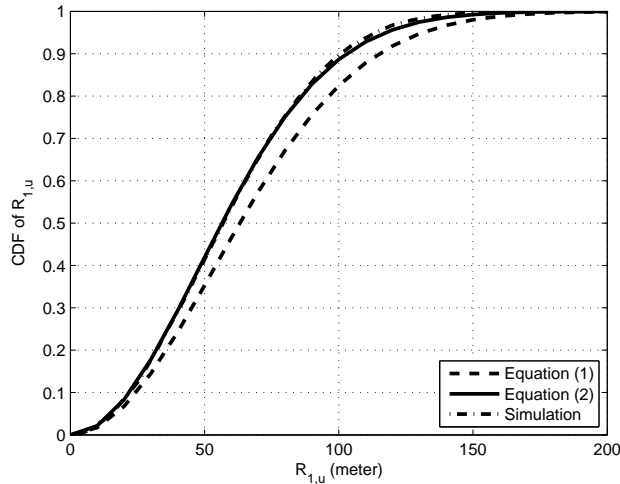
Figure 2.14: Plot of empirical CDF obtained from method $\mathcal{S}$ for distance $R_{1,u}$ between a phantom cell BS and one of the UEs in the phantom cell, chosen at random, for the scenario in Table 2.2. It is seen to be accurately approximated by (2.2). The exact theoretical marginal CDF (2.1) is also shown for comparison.

All these observations are supported by the results (shown in Fig. 2.13) from a simulation with 24 BSs and 720 UEs distributed i.i.d. uniformly over a $10\,\mathrm{km} \times 10\,\mathrm{km}$

square, with distance samples collected only from BSs and UEs in the central $5\,\text{km} \times$ $5\,\text{km}$ region to avoid any bias due to edge effects. We note that the empirical CDFs obtained from $\mathcal{S}'$ and $\mathcal{S}''$ match the theoretical CDF (2.1), while the empirical CDF obtained from $\mathcal{S}$ is closely approximated by (2.2).

Fig. 2.14 shows the results for the 3GPP deployment scenario of a 19-macrocell region with wraparound [44, Fig. 7.10], where each macrocell is a hexagon with the details of the geometry as specified in Table 2.2. We see that the empirical CDF obtained from $\mathcal{S}$ continues to be accurately approximated by (2.2) for $(N_1, N_2) = (4, 80)$ eLA BSs and UEs respectively per macrocell sector as given in Table 2.2. The same also holds with excellent accuracy for $(N_1, N_2) = (4, 60), (4, 160), (6, 120), (8, 80)$, and $(8, 160)$ (plots not shown for lack of space).
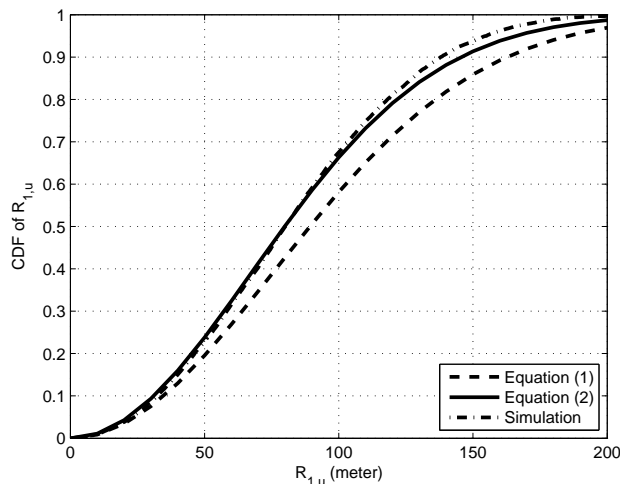
Figure 2.15: Same empirical CDF as plotted in Fig. 2.14, but with parameters $(N_1, N_2) = (2, 60)$ in Table 2.2. Note that (2.2) no longer accurately approximates the CDF over the entire range. The exact theoretical marginal CDF (2.1) is also shown for comparison.

However, for $(N_1, N_2) = (2, 60)$, we notice (see Fig. 2.15) a discrepancy between (2.2) and the empirical CDF obtained from $\mathcal{S}$, which seems to indicate that

41

the model (2.2) is only accurate if the density of eLA BSs is not too low. Finally, we remark that there is both theoretical [56] and empirical [24] support for modeling various distances in Voronoi tessellations by Weibull distributions, of which (2.2) is an example.

Appendix 2-II

For each point x of a PPP Ψ with intensity λ, let its distance from $(0,0)$ be R_x. For $\{H_x\}_{x\in\Psi}$ with i.i.d. Exp(1) and $\alpha > 0$, define

$$I = \sum_{x\in\Psi:R_x>d} \alpha \frac{R_{1,u}^{\delta}}{R_x^{\delta}} H_x [1 - \epsilon 1\{R_x \leq R_{1,u}\}], \ \epsilon \in \{0,1\}.$$

Then, following steps similar to [49, (19)], we can show that

$$\mathcal{L}_I(s) = \exp\left\{ -2\pi\lambda \int_d^\infty r\, \mathbb{E}\left[\frac{1}{1 + \frac{(r/R_{1,u})^\delta}{s\alpha[1-\epsilon 1\{r\leq R_{1,u}\}]}} \right] \mathrm{d}r \right\}.$$

From integration by parts, we obtain

$$\int_0^\infty r\, \mathbb{E}\left[\frac{1}{1 + \frac{(r/R_{1,u})^\delta}{s\alpha[1-\epsilon 1\{r\leq R_{1,u}\}]}} \right] \mathrm{d}r = \left[\frac{1}{1 + \frac{1}{s\alpha(1-\epsilon)}} - \frac{1}{1 + \frac{1}{s\alpha}} \right] \int_d^\infty r\, \mathbb{P}\{R_{1,u} > r\}\, \mathrm{d}r$$

$$+ s\alpha \left\{ \int_1^\infty \frac{(1-\epsilon)}{[1+s\alpha(1-\epsilon)y]^2} \int_d^\infty r\, \mathbb{P}\{R_{1,u} > ry^{1/\delta}\}\, \mathrm{d}r\, \mathrm{d}y \right.$$

$$\left. + \int_0^1 \frac{1}{(1+s\alpha y)^2} \int_d^\infty r\, \mathbb{P}\{R_{1,u} > ry^{1/\delta}\}\, \mathrm{d}r\, \mathrm{d}y \right\}.$$

Given the distribution (2.2), we then obtain

$$\mathcal{L}_I(s) = \exp\left\{ -\frac{\lambda}{c\lambda_1}\left[\frac{1}{1+\frac{1}{s\alpha(1-\epsilon)}} - \frac{1}{1+\frac{1}{s\alpha}} + (1-\epsilon)s\alpha \int_1^\infty \frac{y^{-2/\delta}\exp(-\pi c\lambda_1 d^2 y^{2/\delta})}{[1+s\alpha(1-\epsilon)y]^2}\, dy \right.\right.$$
$$\left.\left. + s\alpha \int_0^1 \frac{y^{-2/\delta}\exp(-\pi c\lambda_1 d^2 y^{2/\delta})}{(1+s\alpha y)^2}\, dy \right]\right\}. \tag{2.28}$$

Appendix 2-III

From [25, 9.121.27, p. 997], we have

$$_2F_1\left(1,\frac{1}{2};\frac{3}{2};-x\right) = \frac{\tan^{-1}\sqrt{x}}{\sqrt{x}}, \; x > 0.$$

Also

$$_2F_1\left(0,\frac{1}{2};\frac{3}{2};-x\right) = 1.$$

Based on [25, 9.137.2, p. 1000], we obtain

$$_2F_1\left(2,\frac{1}{2};\frac{3}{2};-x\right) = \frac{1}{2}\left(\frac{1}{1+x} + \frac{\tan^{-1}\sqrt{x}}{\sqrt{x}}\right), \; x > 0. \tag{2.29}$$

CHAPTER 3

3D BEAMFORMING IN MACRO-ASSISTED SMALL CELL ARCHITECTURE

In this chapter, we exploit 3D beamforming for traffic load balancing and capacity enhancement in the macro-assisted small cell architecture as described in Chapter 2. In Section 3.1, we provide the motivation and feasibility of 3D beamforming for phantom cell architecture together with the antenna, channel and link models. Then the traffic load balancing problem is investigated in Section 3.2 and the capacity enhancement problem is examined in Section 3.3. Finally the concluding remarks are given in Section 3.4.

3.1 System model

3.1.1 3D beamforming for phantom cell architecture

Linear antenna arrays with fixed radiation patterns in the vertical domain are used at BSs in conventional macrocells. The transmitted beamwidth in the vertical dimension and the antenna down-tilt are usually fixed. Occasional adjustment of the down-tilt angle can be achieved mechanically or electronically, for example by Remote Electrical Tilt (RET) devices, to direct the main lobe of the antenna response towards the ground. The reason for not using dynamic 3D beamforming in conventional macrocells is that the broadcast signals/paging signals can not be transmitted in

dynamic beamforming manner with narrow beamwidth, otherwise, the coverage and mobility issues would occur. However, this is not the case for phantom cells. In phantom cell architecture, since macrocells can provide basic service coverage and mobility robustness, conventional cellular network problems, such as coverage holes or handover failure, do not occur in the flexible 3D beamforming operations. With 3D beamforming, the antenna radiation pattern can be dynamically controlled in full dimensions by adaptively weighting the elements in the 2D or 3D antenna array. With the dynamic and flexible beam pattern adaptation, the received signal quality can be improved and the interference can also be controlled more effectively. So 3D beamforming would be very useful especially for the dense small cell deployment scenario, in which the interference issue is one of the major concerns.

3.1.2   Antenna and channel model

The BS antenna radiation pattern from [1] is applied and given by

$$A(\phi, \theta) = -\min\left\{-[A_H(\phi) + A_V(\theta)], A_m\right\}, \qquad (3.1)$$

where $A(\phi, \theta)$ is the overall radiation pattern in dB with azimuth angle ϕ and elevation angle θ. $A_H(\phi)$ and $A_V(\theta)$ are the horizontal pattern and vertical pattern given, respectively, by

$$A_H(\phi) = -\min\left[12\left(\frac{\phi - \phi_{st}}{\phi_{3dB}}\right)^2, A_m\right], \qquad (3.2)$$

and

$$A_V(\theta) = -\min\left[12\left(\frac{\theta - \theta_{tilt}}{\theta_{3dB}}\right)^2, SLA_V\right],\qquad(3.3)$$

where ϕ_{st} is the horizontal steering angle, θ_{tilt} is the vertical down-tilt angle, ϕ_{3dB} is the horizontal 3 dB beamwidth, θ_{3dB} is the vertical 3 dB beamwidth, $A_m = 25$ dB is the front-back ratio, and $SLA_V = 20$ dB is the side-lobe level limit. The quadruple $\{\phi_{st}, \theta_{tilt}, \phi_{3dB}, \theta_{3dB}\}$ essentially defines the beam pattern.

The channel coefficient between sector s and UE k is then given by

$$h_{k,s} = \sqrt{G \cdot A_{k,s}(\phi, \theta) \cdot PL(d_{k,s}) \cdot Z_{k,s}} \cdot \alpha_{k,s},\qquad(3.4)$$

where G is the BS antenna gain, $A_{k,s}(\phi, \theta)$ is the antenna radiation pattern in linear scale, $PL(d_{k,s})$ is the path loss depending on the distance $d_{k,s}$ between sector s and UE k, $Z_{k,s}$ is the log-normal shadowing, and $\alpha_{k,s}$ is the small-scale fading between sector s and UE k. Apparently, with different beamforming schemes, the antenna radiation pattern will be different since the beam patterns are different, which will result in different system performance. For the conventional sectorization with fixed down-tilt beamforming scheme, the down-tilt angle for each sector is fixed and cannot be adjusted dynamically. The optimal down-tilt angle θ_{tilt} can be determined based on cell coverage area to maximize the system capacity. The default values for 3 dB beamwidth in horizontal and vertical domain from 3GPP [1] are adopted, that is, $\phi_{3dB} = 70°$ (for 3 horizontal sectors per cell site) and $\theta_{3dB} = 10°$.

3.1.3 Link model

We consider downlink transmission in a homogeneous network of M small cell sites and L UEs. It is noted that we assume the small cells are operated in higher frequency bands, such as 3-60 GHz, in which it is more likely that no macro cells are deployed. The small cells are assumed to be deployed randomly and uniformly while the UEs are deployed non-uniformly. Each small cell site is further divided into N sectors and each UE is only allowed to be associated with one small cell sector. Then the total number of sectors in the system is $S = N \times M$. We denote the set of small cell sites by $\mathcal{M} = \{1, 2, ..., M\}$, the set of sectors per small cell site by $\mathcal{N} = \{1, 2, ..., N\}$, and the set of UEs by $\mathcal{L} = \{1, 2, ..., L\}$. In each sector $n \in \mathcal{N}$ of small cell $m \in \mathcal{M}$, *3D beamforming* is realized to serve the associated UE set, denoted by $\mathcal{K}_{mn}$. The frequency reuse factor is 1 for all the sectors. Then the signal to interference plus noise ratio (SINR) for UE $l \in \mathcal{K}_{mn}$ is:

$$\gamma_{l,mn} = \frac{P|h_{l,mn}|^2}{P \sum_{s \in \mathcal{M} \backslash m} \sum_{t \in \mathcal{N}} |h_{l,st}|^2 + P \sum_{t \in \mathcal{N} \backslash n} |h_{l,mt}|^2 + N_o}, \qquad (3.5)$$

where $h_{l,mn}$ is the channel coefficient between UE l and sector n in small cell m as expressed in (3.4), N_o is the noise power, and P is the BS transmit power for each sector. The operator $|\cdot|$ denotes the absolute value of a number. So the first term in the denominator denotes the inter-cell interference while the second term denotes the intra-cell interference. The instantaneous achievable rate for UE $l \in \mathcal{K}_{mn}$ is then

given by

$$r_{l,mn} = \log_2(1 + \gamma_{l,mn}) \text{ [bps/Hz]}. \tag{3.6}$$

3.2   3D beamforming for traffic load balancing

3.2.1   Problem formulation

Since the small cell coverage is usually very limited compared to the macrocell, thus the traffic load distribution would be more likely to be non-uniform and fluctuate dynamically. Due to the non-uniform traffic distribution, the UEs connected to an overloaded cell will experience performance degradation due to the limited time-frequency resource. This performance degradation is even more serious for the cell edge UEs due to the severe inter-cell interference. So the objective of load balancing is to associate each UE to one small cell sector intelligently such that the cell edge user throughput can be improved while maintaining the overall cell throughput.

Define the association indicator as follows:

$$c_{l,mn} = \begin{cases} 1, & \text{if UE } l \text{ is associated with sector } n \text{ in cell } m \\ 0, & \text{otherwise} \end{cases} . \tag{3.7}$$

Then the number of UEs associated with sector n in cell m is $K_{mn} = \sum_{l \in \mathcal{L}} c_{l,mn}$. Assume that all UEs have the same traffic statistics and the time-frequency resources are allocated equally to each UE in each cell site, then the long-term average achievable

rate of UE l can be approximated by

$$R_l = \sum_{m \in \mathcal{M}} \sum_{n \in \mathcal{N}} c_{l,mn} \frac{r_{l,mn}}{K_{mn}}. \tag{3.8}$$

We try to find the optimal cell sector association strategy $C = \{c_{l,mn}, l \in \mathcal{L}, m \in \mathcal{M}, n \in \mathcal{N}\}$ such that the aggregate system utility is maximized:

$$\begin{aligned} \max_{C} \quad & \sum_{m \in \mathcal{M}} \sum_{n \in \mathcal{N}} \sum_{l \in \mathcal{K}_{mn}} U_l(R_l) \\ \text{s.t.} \quad & \sum_{m \in \mathcal{M}} \sum_{n \in \mathcal{N}} c_{l,mn} = 1, \forall \ l \in \mathcal{L}, \end{aligned} \tag{3.9}$$

where $U_l(\cdot)$ is a differentiable, concave, and non-decreasing utility function of the average achievable rate R_l of UE l. The logarithmic utility function is adopted here for the purpose of traffic load balancing.

3D UE-specific beamforming method is realized for traffic load balancing. For UE-specific beamforming, the beam direction $\{\phi_{st}, \theta_{tilt}\}$ is adjusted on a per-UE basis such that the beam peak points towards the active UE. In this way, the received signal power is maximized. It is worth noting that narrower beamwidth $\{\phi_{3dB}, \theta_{3dB}\}$ is desired for both vertical and horizontal dimensions in order to alleviate the interference leakage to the neighboring cells without any complicated coordination. This unique feature of UE-specific beamforming makes it very effective for traffic load balancing and capacity enhancement compared to the conventional beamforming schemes. However, there are some implementation issues that need to be taken into consideration for UE-specific beamforming, as we will elaborate later.

3.2.2 Proposed load balancing algorithms

We propose to solve the load balancing problem in Section 3.2.1 with *UE-specific beamforming* in two steps:

- Step 1 (Inter-cell load balancing/cell association): each UE is associated with a unique small cell site based on the log utility optimization.

- Step 2 (Intra-cell load balancing/cell sectorization): based on the cell association results in step 1, optimal cell sectorization is conducted for each small cell site based on the log utility optimization.

3.2.2.1 Inter-cell load balancing

The inter-cell load balancing problem can be formulated as follows:

$$\max_{C_1} \quad \sum_{m \in \mathcal{M}} \sum_{l \in \mathcal{K}_m} \log(R_l) \qquad (3.10)$$
$$\text{s.t.} \quad \sum_{m \in \mathcal{M}} c_{l,m} = 1, \forall\, l \in \mathcal{L},$$

where $C_1 = \{c_{l,m}, l \in \mathcal{L}, m \in \mathcal{M}\}$ is the cell association indicator, and $\mathcal{K}_m = \{l \in \mathcal{L}, c_{l,m} = 1\}$ denotes the UEs associated with small cell m.

Proposed inter-cell load balancing algorithm:

Centralized solution for the above optimization problem requires global network information and it is not very realistic, especially in the high density small cell networks. Distributed algorithms have been proposed in the literature, known as load-aware cell-site selection in [50] and rate biasing in [59]. In contrast to the conventional

best cell association scheme, where the cell with the best radio link quality in terms of signal to interference plus noise ratio (SINR) is selected as the serving cell, the proposed algorithms adopt the following metric:

$$s_m = \frac{B}{K_m} \cdot \log_2(1 + \gamma_m), \qquad (3.11)$$

where B is the total system bandwidth, K_m is the number of active users in small cell m, and γ_m is the signal to interference plus noise ratio if cell m is selected as the serving cell. It is straightforward from (3.11) that this metric takes into account both the radio link quality and the cell load conditions (available frequency resource). However, in [50, 59], 3D beamforming is not considered for traffic load balancing. We propose a load balancing based cell association algorithm with UE-specific beamforming. In the proposed algorithm, the best cell association is conducted first. Then based on the best cell association results, the overloaded cells are identified. For the UEs in the overloaded cells, cell re-association is conducted based on the above metric. We term it *load balancing based cell association* and the detailed algorithm is illustrated in Algorithm 1.

Effect of beamforming schemes:

To illustrate the effect of 3D UE-specific beamforming on the above log utility optimization for traffic load balancing, we consider a simple scenario with two small cells. Assume cell 1 is overloaded with L_1 UEs and cell 2 is underloaded with L_2 UEs ($L_2 < L_1$). We further assume that the UEs in each cell are ordered according to their SINRs, with UE 1 having the lowest SINR. Without load balancing, the system

51

Algorithm 1: Load balancing cell association
---

1. For each UE l, calculate the SINR $\gamma_{l,m}$ from all the cells and select the cell C_l with maximum SINR:

$$C_l = \arg\max_m \gamma_{l,m}.$$

2. For each small cell m, the load can be determined as follows:

$$K_m = \sum_{l=1}^{L} I(C_l = m),$$

where $I(C_l = m) = \begin{cases} 1, & \text{if } C_l = m \\ 0, & \text{if } C_l \neq m \end{cases}$.

3. For each small cell m, it is overloaded if $K_m > K_{th}$, where K_{th} is the overload threshold.

4. For each UE l associated with the overloaded small cell, cell reassociation is conducted as follows:

$$\tilde{C}_l = \arg\max_m \begin{cases} \frac{B}{K_m} \cdot \log_{10}(1 + \gamma_{l,m}), & \text{if } C_l = m \\ \frac{B}{K_m+1} \cdot \log_{10}(1 + \gamma_{l,m}), & \text{if } C_l \neq m \end{cases}.$$

If $\tilde{C}_l \neq C_l$, then $K_{\tilde{C}_l} = K_{\tilde{C}_l} + 1, K_{C_l} = K_{C_l} - 1$.

---

utility is given by

$$
\begin{aligned}
t_1 &= \sum_{i=1}^{L_1} \log\left(\frac{1}{L_1} \log\left(1 + \gamma_i\right)\right) + \sum_{j=1}^{L_2} \log\left(\frac{1}{L_2} \log\left(1 + \beta_j\right)\right) \\
&= \log\left(\left(\frac{1}{L_1}\right)^{L_1} \left(\frac{1}{L_2}\right)^{L_2} \prod_{i=1}^{L_1} \log(1 + \gamma_i) \prod_{j=1}^{L_2} \log(1 + \beta_j)\right),
\end{aligned}
$$

where γ_i is the SINR of UE i in cell 1 and β_j is the SINR of UE j in cell 2.

For traffic offloading, it is intuitive that the low SINR UEs in overloaded cells should be offloaded to the neighboring underloaded cells. Suppose that Q UEs (la-

belled from 1 to Q) are offloaded from cell 1 to cell 2, then the system utility becomes

$$
\begin{aligned}
t_2 &= \sum_{i=Q+1}^{L_1} \log\left(\frac{1}{L_1 - Q} \log\left(1 + \gamma_i\right)\right) + \sum_{j=1}^{L_2} \log\left(\frac{1}{L_2} \log\left(1 + \beta_j\right)\right) \\
&+ \sum_{k=1}^{Q} \log\left(\frac{1}{L_2 + Q} \log\left(1 + \theta_k\right)\right) \\
&= \log\left(\frac{1}{(L_1 - Q)^{L_1 - Q}(L_2 + Q)^{L_2 + Q}} \prod_{i=Q+1}^{L_1} \log(1 + \gamma_i) \prod_{j=1}^{L_2} \log(1 + \beta_j) \prod_{k=1}^{Q} \log(1 + \theta_k)\right),
\end{aligned}
$$

where θ_k is the SINR of UE k after overloaded to cell 2 from cell 1.

We define

$$
T = \frac{\exp(t_2)}{\exp(t_1)} = \frac{L_1{}^{L_1} L_2{}^{L_2}}{(L_1 - Q)^{L_1 - Q}(L_2 + Q)^{L_2 + Q}} \cdot \prod_{k=1}^{Q} S_k, \tag{3.12}
$$

where $S_k = \frac{\log(1+\theta_k)}{\log(1+\gamma_k)}$ is the ratio between data rate after and before offloading for UE k. Then we aim to find Q UEs to be offloaded from cell 1 to cell 2 such that T is maximized.

(a) CDF of data rate ratio S_k (b) CDF of number of UEs per cell
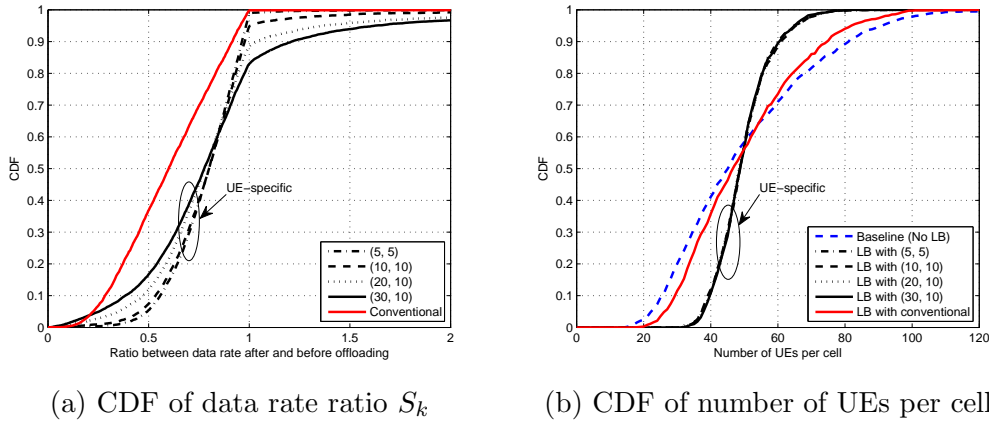
Figure 3.1: Inter-cell load balancing comparison between conventional and UE-specific beamforming with different horizontal and vertical beamwidths $(\phi_{3dB}, \theta_{3dB})$.

From (3.12), we observe that the number of UEs that can be offloaded from cell 1

to cell 2 depends on the load of each cell (L_1 and L_2) and the SINR before and after traffic offloading. If $\prod_{k=1}^{Q} S_k = 1$, then the optimal number of UEs to be offloaded from cell 1 to cell 2 is $Q_{opt} = \frac{1}{2}(L_1 - L_2)$ such that the number of UEs in cell 1 and 2 is equal. However, in real systems, $\prod_{k=1}^{Q} S_k$ is usually less than 1, which will lower the number of UEs offloaded from cell 1 to cell 2. In addition, with different antenna pattern and beamforming schemes, the characteristics for S_k will be different. Fig. 3.1a shows the CDF comparison between the conventional sectorization with fixed down-tilt and 3D UE-specific beamforming with different beamwidths $(\phi_{3dB}, \theta_{3dB})$ for the ratio between UE data rate after and before load balancing. It is seen that the ratio for UE-specific beamforming is larger than that for the conventional case. This is due to the unique feature of UE-specific beamforming that the signal is maximized and interference is limited due to narrower beamwidth. The corresponding CDF curves for the number of UEs per cell are shown in Fig. 3.1b. As expected, load balancing based cell association with UE-specific beamforming can make the load per cell more uniform compared to the conventional sectorization with fixed down-tilt case, which results in more load balancing gain. For UE-specific beamforming with different horizontal and vertical beamwidths, the performance in terms of cell association is almost the same as shown in Fig. 3.1b. This can be inferred from Fig. 3.1a that, with wider beamwidths, the probabilities of S_k being in the lower value range and the higher value range are both larger. So the overall product $\prod_{k=1}^{Q} S_k$ would be similar for different beamwidths. The throughput gain of UE-specific beamforming with narrower beamwidth over wider beamwidth mainly comes from the SINR gain

as shown in Fig. 3.3a, instead of the load balancing gain.

(a) CDF of SINR   (b) CDF of data rate ratio
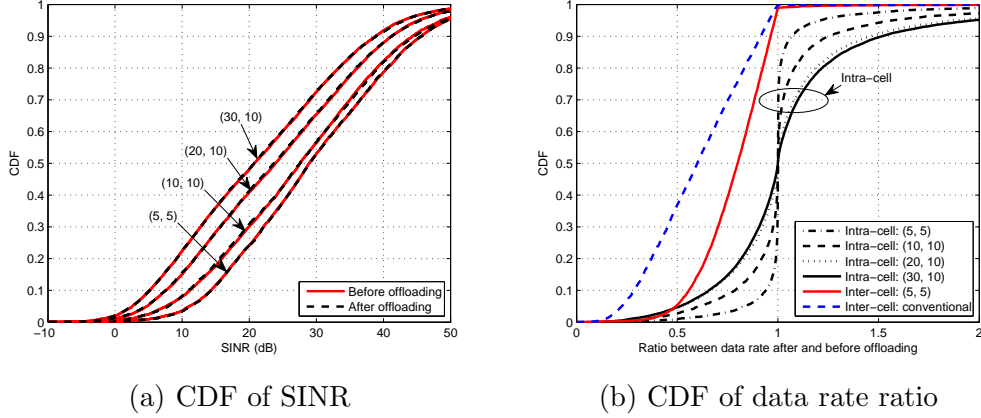
Figure 3.2: Intra-cell load balancing comparison for UE-specific beamforming with different horizontal and vertical beamwidths $(\phi_{3dB}, \theta_{3dB})$.

3.2.2.2   Intra-cell load balancing

Based on the cell association results in inter-cell load balancing, each cell site is further sectorized to serve the UEs associated with the cell site. Since the UEs are usually non-uniformly distributed, the conventional way to sectorize the cell in equal width uniformly (regular sectorization) is obviously not the best strategy. Here we aim to find the optimal sectorization scheme for the purpose of traffic load balancing. For each cell site m, the intra-cell load balancing can be formulated as follows:

$$\max_{C_m} \quad \sum_{n \in \mathcal{N}} \sum_{l \in \mathcal{K}_{mn}} \log \left(\frac{B}{K_{mn}} \cdot \log_2(1 + \gamma_{l,mn}) \right) \tag{3.13}$$
$$\text{s.t.} \quad \sum_{n \in \mathcal{N}} K_{mn} = K_m,$$

where $C_m = \{c_{l,mn}, l \in \mathcal{K}_m, n \in \mathcal{N}\}$ is the sector association indicator in cell m, and $\mathcal{K}_{mn} = \{l \in \mathcal{K}_m, c_{l,mn} = 1\}$ denotes the UEs associated with sector n in small cell m.

The objective function in (3.13) can be rewritten as:

$$\sum_{n \in \mathcal{N}} \sum_{l \in \mathcal{K}_{mn}} \log \left(\frac{B}{K_{mn}} \cdot \log_2(1 + \gamma_{l,mn}) \right) \tag{3.14}$$

$$= \sum_{l=1}^{K_m} \log \left(B \cdot \log_2(1 + \gamma_{l,mn}) \right) - \sum_{n=1}^{N} K_{mn} \log(K_{mn})$$

Fig. 3.2a demonstrates that the UE SINR performance before and after intra-cell offloading is almost the same for UE-specific beamforming with different beamwidths. Then it is reasonable that we can neglect the first term in the right hand side of Eq. (3.14) and the optimization problem in (3.13) is equivalent to

$$\min_{C_m} \quad \sum_{n=1}^{N} K_{mn} \log(K_{mn}) \tag{3.15}$$

$$\text{s.t.} \quad \sum_{n \in \mathcal{N}} K_{mn} = K_m.$$

It is easy to find that the optimal solution is

$$K_{mn} = \frac{K_m}{N}, \forall \ m \in \mathcal{M} \text{ and } n \in \mathcal{N}. \tag{3.16}$$

This implies that, given a certain number of sectors per small cell N, each cell should be sectorized such that the number of UEs in each sector is the same. Note that when $\frac{K_m}{N}$ is not an integer, it would be natural to place $\lfloor \frac{K_m}{N} \rfloor$ UEs in each sector, and distribute the remaining UEs evenly to the sectors. It is also noted that, for intra-cell load balancing, the ratios between data rate after and before offloading are located more around 1 as shown in Fig. 3.2b compared to inter-cell load balancing. This also

indicates that more load balancing gain can be achieved by intra-cell load balancing, which will be confirmed by simulation results in Section 3.2.4.

3.2.3 Implementation issues for 3D UE-specific beamforming

3.2.3.1 Antenna beamwidth

The antenna beamwidth is limited by the number of antenna elements in the antenna array. Consider a linear uniformly-spaced antenna array with E antenna elements in horizontal dimension and assume that the antenna element spacing is d, then the 3 dB beamwidth at broadside is given by [43]

$$\phi_{3dB} = 50.76° \frac{\lambda}{Ed},\tag{3.17}$$

where λ is the carrier wavelength. Then the linear antenna array length in horizontal dimension for a given ϕ_{3dB} beamwidth can be found by

$$H = (E - 1) \times d = 50.76° \frac{\lambda}{\phi_{3dB}} - d.\tag{3.18}$$

So for a carrier frequency of 3.5 GHz and antenna element spacing of $d = \frac{\lambda}{2}$, the antenna array length required in order to achieve a 3 dB beamwidth of 10°, 5°, and 1° are 0.43, 0.86, and 4.34 meters, respectively. It is obvious that 4.34 meters would be too large for a small cell BS antenna. Therefore, in our following evaluations, the minimum 3 dB beamwidth is set to be 5° in both horizontal and vertical dimensions.

The SINR and IoT comparisons between the conventional sectorization with fixed

down-tilt (as mentioned in Section. 3.1.2) and UE-specific beamforming with different horizontal and vertical beamwidths $\{\phi_{3dB}, \theta_{3dB}\}$ are provided in Figs. 3.3a and 3.3b, respectively. It is seen that the SINR for UE-specific beamforming is improved significantly compared to the conventional beamforming scheme. As the beamwidth increases, the SINR for UE-specific beamforming degrades due to the increased interference as illustrated in Fig. 3.3b.

(a) SINR CDF   (b) IoT CDF
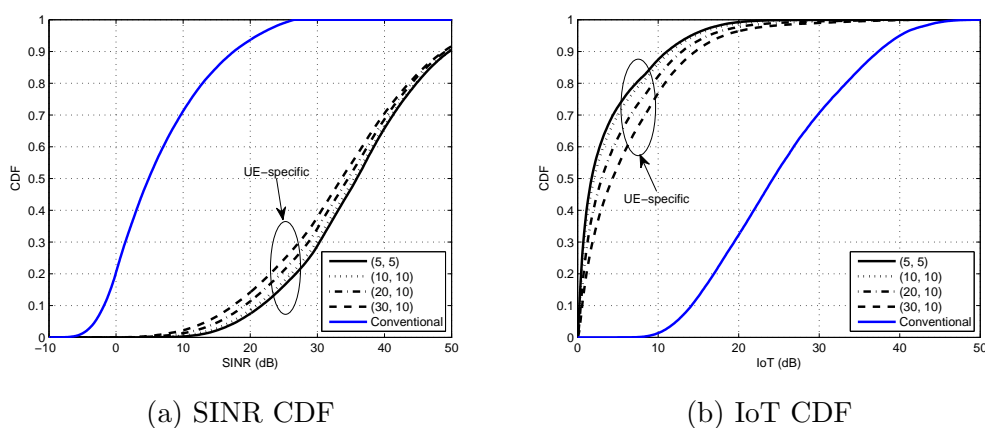
Figure 3.3: SINR and IoT comparisons between conventional and UE-specific beamforming with different horizontal and vertical beamwidths $(\phi_{3dB}, \theta_{3dB})$.

3.2.3.2   Cell association based on UE-specific beamforming

(a) SINR for cell edge UE 1   (b) SINR for cell center UE 2
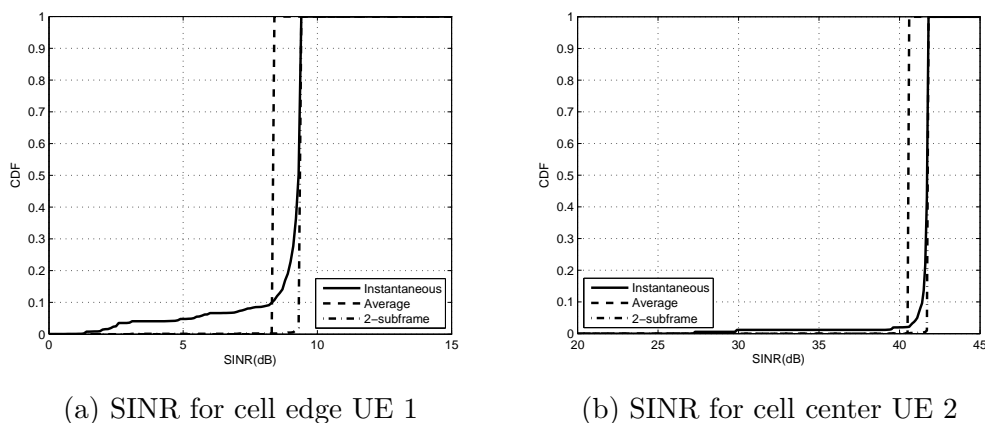
Figure 3.4: Instantaneous and average SINR for UE-specific beamforming.

In contrast to the conventional sectorization with fixed antenna pattern scenario, the interference is dynamically changing for each UE at each subframe depending on the UEs scheduled in the neighboring cells for the dynamic UE-specific beamforming. Therefore, the instantaneous SINR would be dynamically changing for each UE at different subframes as shown in Fig. 3.4. Cell association based on the instantaneous SINR would be problematic. One solution is to average the interference in each neighboring cell for a sufficiently large number of subframes to compute the average SINR. However, this would incur high computational complexity and large delay for cell association. In Fig. 3.4, we show the CDF comparisons for the instantaneous and average SINR for two UEs. UE 1 is at the cell edge and UE 2 is near the cell center. It is seen that the instantaneous SINR is fluctuating and would be lower than the average SINR especially for the cell edge UE with a probability of about 10%. Based on this observation, we propose to compute the interference for cell association with two subframes. We simply choose the lower interference in the previous two subframes for SINR computation for each UE during the cell association stage. In this way, the probability of the computed SINR being lower than the average SINR would be reduced to about 1%, as shown in Fig. 3.4. In addition, both the complexity and delay would be much lower compared to the computation for average SINR.

3.2.4 System level simulations

System level dynamic simulations are conducted to evaluate the performance of the proposed load balancing methods. Table 3.1 lists the detailed simulation parameters. The simulation setup, results and analysis are provided as follows.

Table 3.1: Simulation Parameters

Parameter	Value
Carrier frequency	3.5 GHz
System bandwidth	10 MHz, frequency reuse 1
Inter macro site distance	500 meters (3GPP case 1)
Small cell layout	Uniformly and randomly distributed
Number of resource blocks	50
Thermal noise spectral density	-174 dBm/Hz
Noise figure	5 dB
Small cell BS TX power	24 dBm per sector
UE antenna gain	0 dBi
Small cell BS antenna gain	5 dBi
Small cell BS antenna pattern	3D antenna pattern in Table A.2.1.1-2 in [1]
Antenna height	BS: 10 m, UE: 1.5 m
Path Loss model	UMi NLOS and LOS (Table A1-2 in [29])
Fast Fading	Typical Urban
Lognormal shadowing	All links are correlated with coefficient 0.5 and standard deviation $\sigma = 4$ dB
Penetration Loss	0 dB
Number of small cells	2/4/8 per macro sector
Number of sectors per small cell	3/6/12 per macro sector
Number of UEs	100 per macro sector
Transmitter antennas	1TX
Receiver antennas	2RX
Aadaptive modulation and coding	6 ms feedback delay with transport formats specified in [2]
Hybrid automatic repeat request	8 ms round trip delay with chase combining
Scheduler	Round robin
Traffic model	Full buffer

3.2.4.1   Simulation setup

We consider a regular 19-macrocell hexagonal grid area (with each macrocell serving 3 sectors) as shown in Fig. 3.5. The small cell sites are independently and uniformly distributed in each macro sector. 100 UEs are deployed in each macro sector. To model the non-uniform traffic load, 10% of the 100 users are randomly and uniformly distributed and the remaining 90% are grouped into one cluster. The cluster

is also randomly distributed in each macro sector. Since the conventional macrocells operates at 2 GHz and we assume that the carrier frequency for small cells is 3.5 GHz, there is no interference between conventional macrocells and the small cells. We will focus on the small cells, each of which is divided into three horizontal sectors. For the conventional sectorization with fixed down-tilt beamforming, and the horizontal and vertical beamwidths are set to be $(\phi_{3dB}, \theta_{3dB}) = (70°, 10°)$. For UE-specific beamforming, different 3 dB beamwidths are evaluated, with 5° being the minimum in both horizontal and vertical dimensions, which provides the upper bound on the performance of UE-specific beamforming.
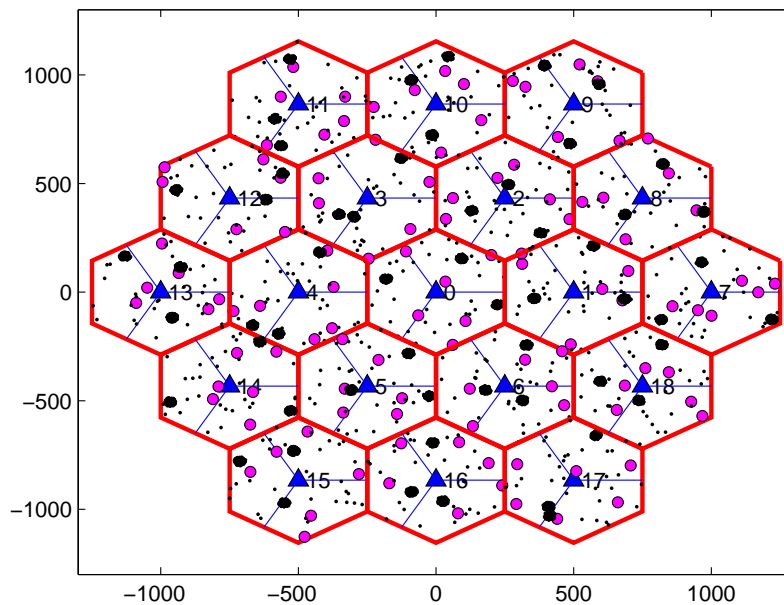
Figure 3.5: An example of system deployment for simulations (black dots: users, magenta dots: small cells, blue triangles: macro cells).

Table 3.2: User throughput and average sector throughput comparisons between conventional sectorization with fixed down-tilt and UE-specific beamforming with different horizontal and vertical beamwidths $(\phi_{3dB}, \theta_{3dB})$.

Performance	Conv.	(30, 10)	(20, 10)	(10, 10)	(5, 5)
5%-ile (Kbps)	54	130 (141%)	178 (230%)	287 (431%)	446 (726%)
20%-ile (Kbps)	122	258 (111%)	313 (157%)	451 (270%)	676 (454%)
50%-ile (Kbps)	254	439 (73%)	548 (116%)	786 (209%)	1017 (300%)
Average (Mbps)	5.41	8.26 (53%)	9.73 (80%)	12.60 (132%)	15.94 (194%)

(a) SINR CDF   (b) User throughput CDF
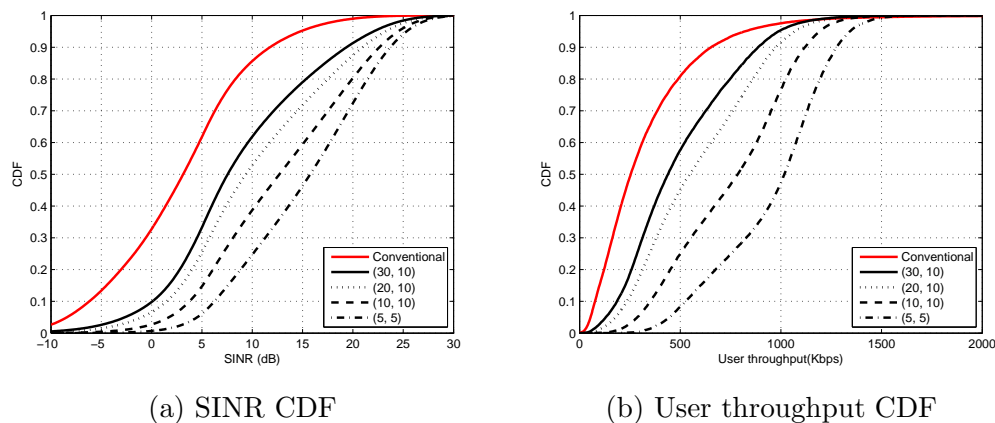
Figure 3.6: Performance comparison for conventional sectorization with fixed down-tilt and UE-specific beamforming with different horizontal and vertical beamwidths $(\phi_{3dB}, \theta_{3dB})$.

3.2.4.2   Simulation results and analysis

<u>Conventional sectorization with fixed down-tilt vs. UE-specific beamforming:</u>

The SINR and user throughput comparisons are shown in Fig. 3.6 for load balancing with conventional sectorization and with UE-specific beamforming. Table. 3.2 also summarizes the 5%-ile, 20%-ile, and 50%-ile user throughput and the average sector throughput comparisons. The 5%-ile user throughput is used as an indicator for the cell edge user throughput. It is observed that significant performance gains over the conventional scheme can be achieved by UE-specific beamforming in terms of both average sector throughput (up to 194% gain) and cell edge user throughput (up

62

Table 3.3: User throughput and average sector throughput comparisons for different load balancing schemes with UE-specific beamforming with $(\phi_{3dB}, \theta_{3dB}) = (5°, 5°)$.

Performance	Baseline	Inter-cell	Intra-cell	Inter-cell & Intra-cell
5%-ile (Kbps)	260	283 (9%)	407 (57%)	446 (72%)
20%-ile (Kbps)	399	473 (19%)	622 (56%)	676 (69%)
50%-ile (Kbps)	620	644 (4%)	874 (41%)	1017 (64%)
Average (Mbps)	12.86	12.28 (-5%)	16.3 (29%)	15.94 (24%)

(a) SINR CDF   (b) User throughput CDF
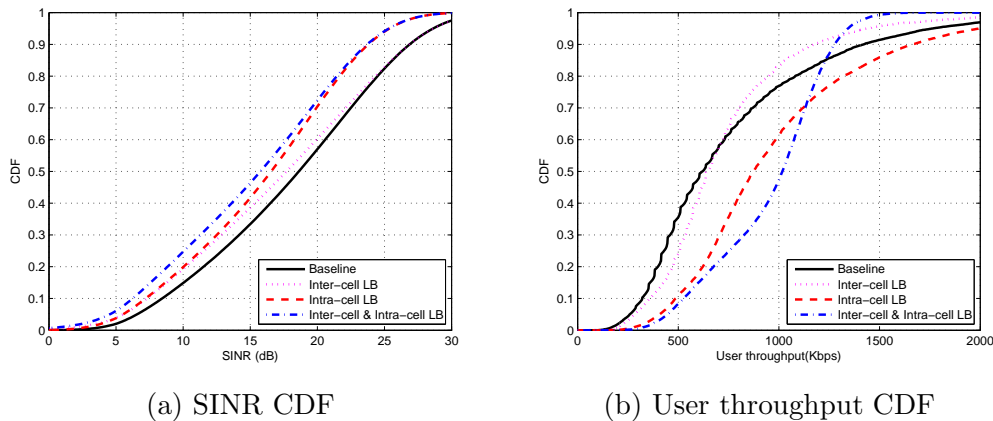
Figure 3.7: Performance comparison for different load balancing schemes with UE-specific beamforming with $(\phi_{3dB}, \theta_{3dB}) = (5°, 5°)$.

to 726% gain). This throughput gain results from both the SINR gain and the load balancing gain as discussed in Sections 3.2.3 and 3.2.2, respectively. For UE-specific beamforming, as the beamwidth increases, the performance degrades due to the SINR degradation caused by interference.

Inter-cell vs. Intra-cell load balancing with UE-specific beamforming:

In Fig. 3.7, the SINR and user throughput comparisons are shown for different load balancing schemes, namely, the baseline system without load balancing, the intra-cell load balancing, the inter-cell load balancing, and both the inter-cell and

Table 3.4: User throughput and average sector throughput comparisons for different number of small cells for conventional beamforming with fixed down-tilt.

Beamforming scheme	Load balancing with conventional beamforming			
Number of small cells	2	4	6	8
5%-ile (Kbps)	56	54 (-4%)	42 (-25%)	25 (-55%)
20%-ile (Kbps)	123	182 (48%)	190 (54%)	176 (43%)
50%-ile (Kbps)	252	406 (61%)	458 (82%)	484 (92%)
Average (Mbps)	5.54	9.80 (77%)	13.86 (150%)	17.92 (223%)
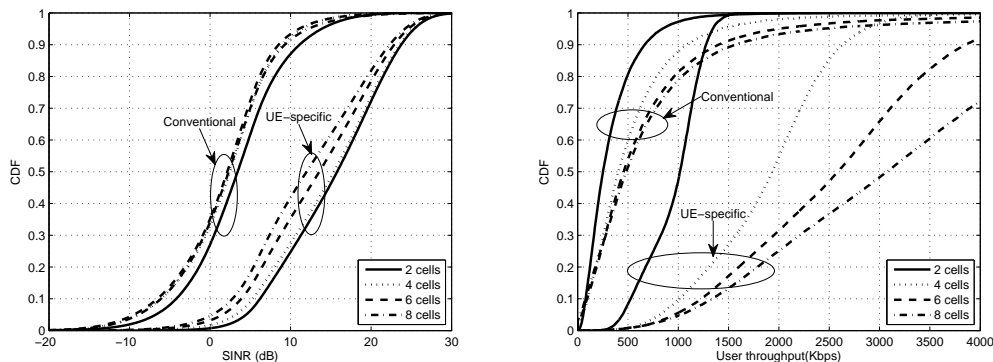
(a) SINR CDF

(b) User throughput CDF

Figure 3.8: Performance comparison for different number of small cells between conventional beamforming with fixed down-tilt and UE-specific beamforming.

intra-cell load balancing for UE-specific beamforming with $(\phi_{3dB}, \theta_{3dB}) = (5°, 5°)$. In Table. 3.3, we also summarize the 5%-ile, 20%-ile, and 50%-ile user throughput and the average sector throughput comparisons. We observe that with both inter-cell and intra-cell load balancing, the cell edge user throughput can be improved most significantly while maintaining good average cell throughput at the same time. In addition, it is also observed that the intra-cell load balancing (adaptive cell sectorization) is more effective than the inter-cell load balancing scheme, which is consistent with the discussions in Section 3.2.2.

Effect of denser cell deployment:

Table 3.5: User throughput and average sector throughput comparisons for different number of small cells for UE-specific beamforming.

Beamforming scheme	Load balancing with UE-specific beamforming			
Number of small cells	2	4	6	8
5%-ile (Kbps)	446	814 (83%)	962 (116%)	1028 (130%)
20%-ile (Kbps)	675	1306 (93%)	1601 (137%)	1786 (165%)
50%-ile (Kbps)	1018	1934 (90%)	2587 (154%)	3074 (202%)
Average (Mbps)	15.98	31.32 (96%)	42.84 (168%)	52.88 (231%)

The performance comparisons between conventional beamforming with fixed down-tilt and UE-specific beamforming are depicted in Fig. 3.8 for different number of small cells. Tables. 3.4 and 3.5 also summarize the 5%-ile, 20%-ile, and 50%-ile user throughput and the average system throughput for the conventional beamforming and UE-specific beamforming, respectively. It is evident that as the number of small cells increases, the average system throughput also increases for both beamforming methods. However, as the number of small cells increases, the cell edge user throughput gain is much larger for UE-specific beamforming compared to the conventional beamforming. The cell edge user throughput even degrades for the conventional beamforming due to interference as the number of small cells increases. In addition, as the number of small cells increases, the antenna pattern for conventional beamforming need to be optimized while this is not an issue for UE-specific beamforming. So the cell planning efforts are lower for UE-specific beamforming, especially for denser small cell deployment since the planning efforts would linearly increase with the number of small cells.

3.3   3D beamforming for capacity enhancement

3.3.1   Introduction

In this section, we investigate the potential of utilizing the AAS-enabled 3D beamforming techniques for capacity improvement in the macrocell-assisted small cell networks. UE-specific 3D beamforming with the main lobe of the beam steering directly to each specific UE has been studied in [51, 33, 52, 18, 55, 8] mainly in macrocell scenarios and significant performance gain has been observed. However, the main problem with UE-specific beamforming is the high implementation complexity especially in frequency-division duplexing (FDD) systems. In FDD systems, the BS broadcasts the channel state information (CSI) reference signals to UEs with different beam patterns, then the active UE measures the CSI and feeds back to the BS. The BS can then transmit the data to the UE with the most appropriate beam pattern. Considering the overhead of the CSI reference signals and the CSI feedbacks, perfect UE-specific beamforming is not feasible. Therefore, UE group-specific beamforming is proposed with a finite number of beam patterns. In this scheme, the UEs are grouped based on their best beam patterns and the UEs within a group have the same best beam pattern. The UE group-specific beamforming is essentially a quantized version of UE-specific beamforming, where the quantization granularity is determined by the number of beam patterns (UE groups). We first provide the performance comparison between the conventional sectorization with fixed down-tilt and UE-specific beamforming to demonstrate the upper bound on the potential gain of 3D beamforming in small cell scenario. Then the study on the performance for UE

66

group-specific beamforming shows more realistic gain we can obtain and also serves as guideline to determine how much granularity is needed for UE group-specific beamforming. System level simulation results show that UE group-specific beamforming can achieve performance comparable to that of UE-specific beamforming in terms of both the cell average capacity and the cell edge user throughput with a certain number of beam patterns.

3.3.2   Proposed UE group-specific beamforming

As we mentioned in Section 3.3.1, the main concern with the above UE-specific beamforming is the feasibility for implementation. We propose the UE group-specific beamforming as a more realistic operation and still try to maintain good system performance. More specifically, for each sector $s \in \mathcal{S}$, a set of beam patterns $\mathcal{B}$ can be used to serve the associated UEs $\mathcal{K}_s$. The BS broadcasts the CSI reference signals to the active UE with different beam patterns in $\mathcal{B}$, then the UE measures the CSI and feeds back to the BS. The BS can then transmit the data to the UE with the most appropriate beam pattern. It is possible that one beam pattern is appropriate for a group of UEs. The performance and the complexity highly depends on how to design the beam pattern set $\mathcal{B}$. Each beam pattern is characterized by a quadruple $\{\phi_{st}, \theta_{tilt}, \phi_{3dB}, \theta_{3dB}\}$. Intuitively, with a larger size of $\mathcal{B}$, the 3 dB beamwidth $(\phi_{3dB}, \theta_{3dB})$ can be narrower, and the performance should be better, however, the complexity would be higher. When the size of $\mathcal{B}$ approaches to infinity, UE group-specific beamforming becomes UE-specific beamforming.

Given a certain number of beam patterns, say B, we propose a simple method

to determine the beam directions $(\phi_{st}, \theta_{tilt})$ of the beam patterns for each sector as follows:

1. Each small cell sector is equally sectorized into B_h sub-sectors horizontally. Accordingly, for each horizontal sub-sector, B_h horizontal steering angles can be determined as $(\phi_{st}^1, \phi_{st}^2, ..., \phi_{st}^{B_h})$.

2. Each small cell sector is equally sectorized into $B_v = B/B_h$ vertical sub-sectors. Accordingly, for each vertical sub-sector, B_v vertical down-tilt angles can be determined as $(\theta_{tilt}^1, \theta_{tilt}^2, ..., \theta_{tilt}^{B_v})$.

3. The beam directions for B beam patterns can be represented in the following $B_h \times B_v$ matrix form

$$
\begin{bmatrix}
(\phi_{st}^1, \theta_{tilt}^1) & (\phi_{st}^1, \theta_{tilt}^2) & \cdots & (\phi_{st}^1, \theta_{tilt}^{B_v}) \\
\vdots & \vdots & \ddots & \vdots \\
(\phi_{st}^{B_h}, \theta_{tilt}^1) & (\phi_{st}^{B_h}, \theta_{tilt}^2) & \cdots & (\phi_{st}^{B_h}, \theta_{tilt}^{B_v})
\end{bmatrix} .
$$

For the above method, the optimal partition (B_h and B_v) and 3 dB beamwidth $(\phi_{3dB}, \theta_{3dB})$ is also crucial. However, this optimization problem is too complicated to analyze mathematically, and we resort to system level simulations in Section 3.3.3 for performance evaluation.

3.3.3 System Level Simulations

System level dynamic simulations are conducted to evaluate the performance of the proposed beamforming methods. The detailed simulation parameters are listed

in Table 3.1. The simulation setup, results and analysis are provided as follows.

3.3.3.1 Simulation setup

We consider a regular 19-macrocell hexagonal grid area (with each macrocell serving 3 sectors). 2 small cells sites and 200 UEs are independently and uniformly distributed in each macro sector. Since the conventional macrocells operates at 2 GHz and we assume that the carrier frequency for small cells is 3.5 GHz, there is no interference between the conventional macrocells and the small cells. We will focus on the small cells. 3D antenna pattern is assumed for each of the small cells with antenna gain of 5 dBi. Each small cell is divided into three horizontal sectors. The UEs are assumed to be static with a maximum Doppler shift of 10 Hz. Given the network setup, $8°$ is adopted as the down-tilt angle for the conventional sectorization with fixed down-tilt beamforming, and the horizontal and vertical beamwidths are set to be $(\phi_{3dB}, \theta_{3dB}) = (70°, 10°)$. For UE-specific beamforming, different 3 dB beamwidths are evaluated, with $5°$ being the minimum in both horizontal and vertical dimensions, which provides the upper bound on the performance of UE-specific beamforming.

3.3.3.2 Simulation results and analysis

Conventional sectorization with fixed down-tilt vs. UE-specific beamforming

The average sector capacity and cell edge user throughput comparisons are provided in Fig. 3.9a. The 5%-tile user throughput is adopted as an indicator of the cell edge user performance. The performance gain percentages compared to the conventional sectorization with fixed down-tilt scheme are also shown in the figure. From

Fig. 3.9a, we observe that significant performance gains over the conventional sector-ization with fixed down-tilt scheme can be achieved by UE-specific beamforming in terms of both cell average capacity (up to 124.8% gain) and cell edge user throughput (up to 454.3% gain). For UE-specific beamforming, as the beamwidth increases, the performance degrades due to interference. Furthermore, Fig. 3.9b depicts the SINR behaviour for the conventional sectorization scheme and UE-specific beamforming, respectively, for different number of small cells per macro sector. It is obvious that the SINR performance for UE-specific beamforming is much better than the conven-tional sectorization scheme. It is also seen that as the number of small cells increases, the SINR performance degrades for the conventional sectorization with fixed down-tilt due to strong interference. On the other hand, the SINR performance does not degrade for UE-specific beamforming with narrow beamwidth as the number of small cells increases. This confirms that with 3D beamforming, the interference can be effectively mitigated without any complicated coordination even in dense small cell deployment scenario.

(a) Capacity comparison (b) SINR comparison
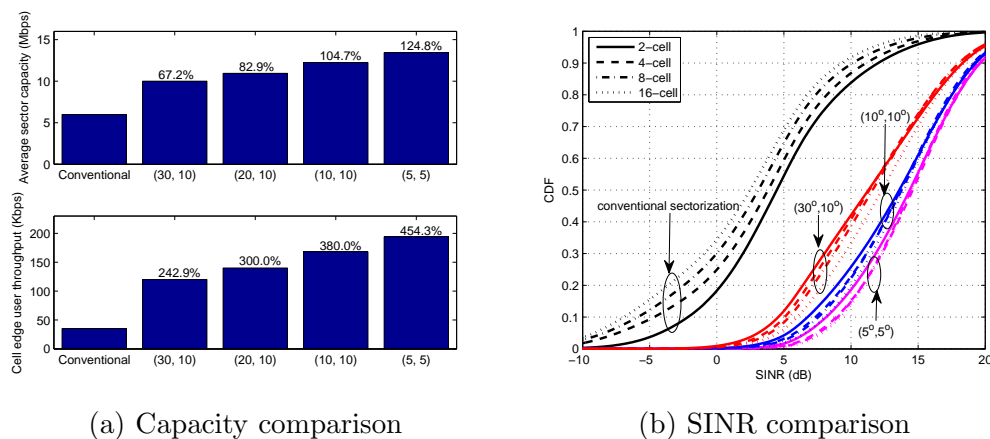
Figure 3.9: Performance comparison between conventional sectorization with fixed down-tilt and UE-specific beamforming with different horizontal and vertical beamwidths $(\phi_{3dB}, \theta_{3dB})$.
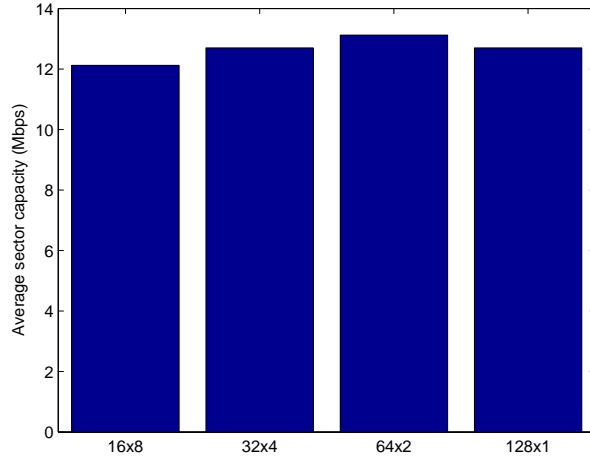
Figure 3.10: Capacity comparison for different partition methods with a given number of 128 beam patterns (the optimal 3 dB beamwidths are $(10°, 5°)$, $(5°, 5°)$, $(5°, 5°)$, and $(5°, 5°)$, respectively).
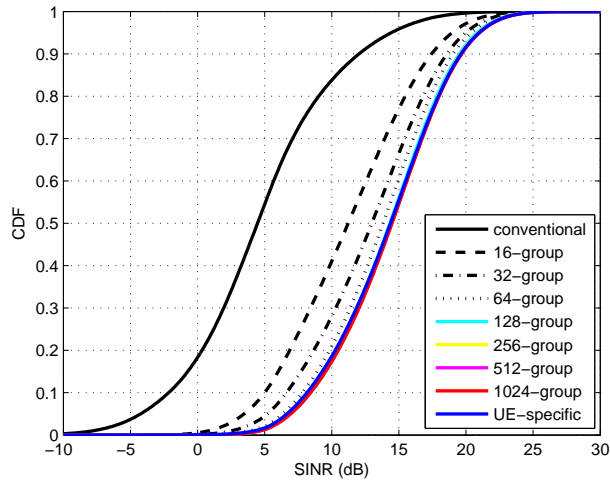
Figure 3.11: SINR comparison for different number of beam patterns (the minimum 3 dB beamwidth is 5° for both UE-specific and UE group-specific beamforming).

Fig. 3.10 shows the average sector capacity comparison for different partition methods with 128 beam patterns. It is seen that the capacity for 64×2 is the best. This indicates that the average capacity increases with more partitions in horizontal domain and less partitions in the vertical domain. However, at least 2

71

partitions in the vertical domain are needed. Figs. 3.11 and 3.12a present the SINR and average sector capacity comparisons for different number of beam patterns. The results for the conventional sectorization scheme and UE-specific beamforming are also included. For each number of beam patterns, the result with the optimal partition method is provided. From Fig. 3.11, it is seen that the SINR performance for UE group-specific and UE-specific beamforming is much better than the conventional sectorization with fixed down-tilt scheme. As the number of beam patterns increases, the SINR performance also improves. With 128 or more beam patterns, the SINR CDF (cumulative distribution function) curves are very similar to that of the UE-specific beamforming.
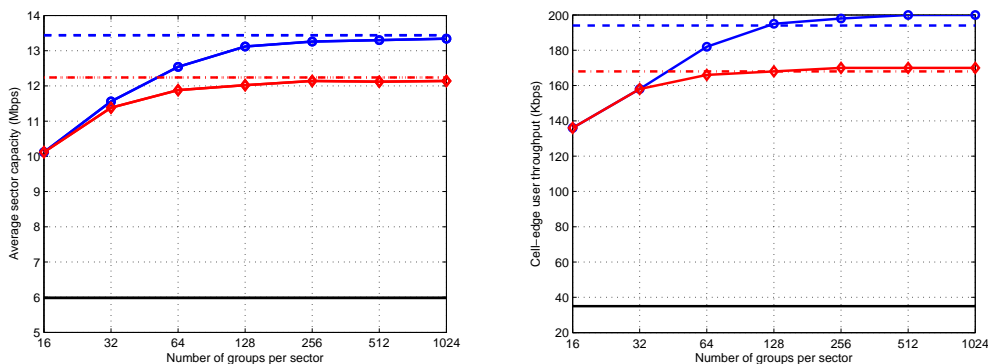
(a) Average sector capacity comparison (b) Cell edge user throughput comparison

Figure 3.12: Performance comparison for different number of beam patterns (the lower solid curve is the result for the conventional sectorization with fixed down-tilt; the blue dashed and the red dash-dotted curves are the results for UE-specific beamforming with $(\phi_{3dB}, \theta_{3dB}) = (5°, 5°)$ and $(10°, 10°)$, respectively; the blue (circle) and the red (diamond) solid curves are the results for UE group-specific beamforming with minimum 3 dB beamwidth of 5° and 10°, respectively).

From Fig. 3.12a, we observe that the capacity gain of UE group-specific beamforming over the conventional sectorization with fixed down-tilt scheme is very significant (about 68% gain for 16 beam patterns). In addition, as the number of beam patterns

increases, the capacity approaches to that of the UE-specific beamforming. Clearly there is a performance-complexity tradeoff. We also observe that when the number of beam patterns are reduced from 1024 to 128, there is only about 2% degradation in the average capacity, but the complexity would be much lower. So 128 beam patterns would be a good option in terms of both capacity and complexity. Furthermore, as the minimum beamwidth increases from 5° to 10°, some capacity degradation is observed due to interference, especially for large number of beam patterns. We also compare the cell edge user throughput for different beamforming methods in Fig. 3.12b and similar behaviour can be observed.

3.4   Conclusions

In this chapter, we addressed the traffic load balancing problem in the macro-assisted small cell architecture. 3D UE-specific beamforming, as a feasible and effective solution in this architecture, has been proposed for traffic load balancing. Novel cell association and sectorization algorithms based on UE-specific beamforming have also been proposed and evaluated in system level simulations. Simulation results demonstrated that the proposed methods can achieve significant improvement for both cell edge user throughput (up to 726% gain) and cell average throughput (up to 194% gain) compared to the conventional beamforming scheme. It is also shown that with denser small cell deployment, UE-specific beamforming can achieve even larger performance gain with less cell planning efforts compared with the conventional beamforming scheme. In addition, we studied different 3D beamforming methods for

capacity improvement in the macrocell-assisted small cell architecture. UE group-specific 3D beamforming has been proposed as a more realistic operation compared to UE-specific beamforming. System level simulations were conducted to evaluate the UE-specific beamforming and UE group-specific beamforming for capacity enhancement in small cell networks. Simulation results confirmed the potential gain of flexible and dynamic 3D beamforming with narrow beamwidth for capacity enhancement compared to the conventional sectorization with fixed antenna down-tilt scheme in terms of both the cell average capacity (up to 124.8% gain) and the cell edge user throughput (up to 454.3% gain). It was also shown that UE group-specific beamforming as a more realistic operation can approach to the performance of UE-specific beamforming.

CHAPTER 4

RESOURCE OPTIMIZATION FOR FULL-DUPLEX RELAYING SYSTEMS

In this chapter, we study the optimal resource allocation for full-duplex DF relaying systems. In Section 4.1, we describe the signal and channel model, based on which the outage probability is provided. In Section 4.2, different resource optimization problems (power optimization, location optimization, and joint optimization) are formulated and analyzed. Numerical results and comparisons are presented in Section 4.3, followed by concluding remarks in Section 4.4.

4.1   System model
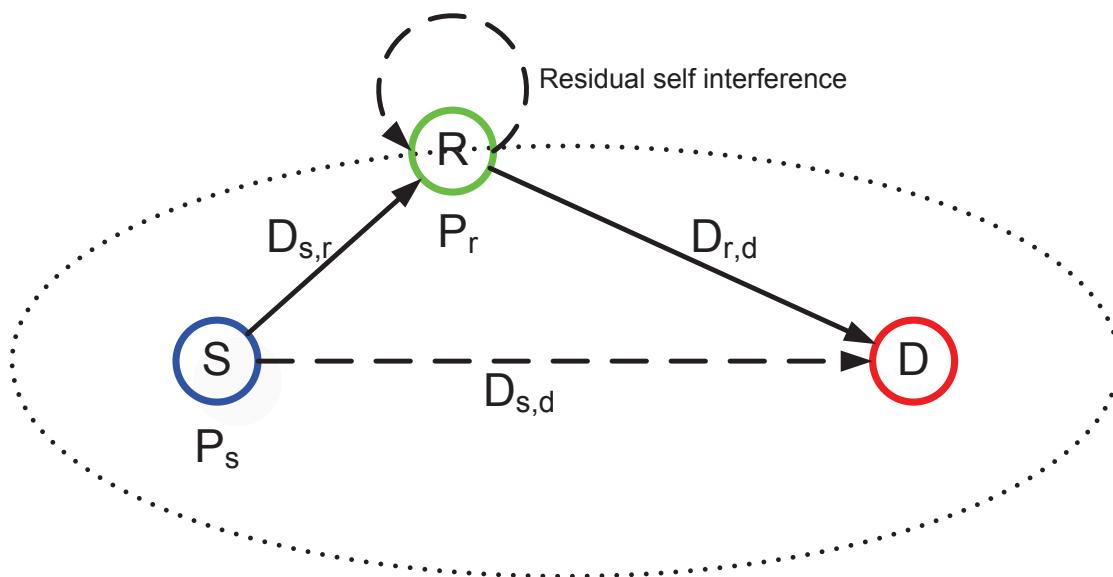
Figure 4.1: Two-hop full-duplex DF system model.

Consider a two-hop relaying system, where a source node (S) communicates with

a destination node (D) via a full-duplex decode-and-forward relay node (R) as shown in Fig. 4.1. In the full-duplex mode, the relay transmits and receives simultaneously at the same frequency, and some interference cancellation methods (such as antenna isolation, analog cancellation, digital cancellation, etc.) are adopted to mitigate the self-interference. However, the interference cannot be completely mitigated. Hence certain amount of RSI has to be considered. Assuming the source-relay channel, source-destination channel, relay-relay RSI channel and relay-destination channel are independent Rayleigh flat fading, we consider relay systems both with and without a direct source-destination link.

4.1.1 Signal and channel model

At time instant n, the source transmits signal x_n^s with power P_s and the relay transmits signal x_n^r with power P_r. Then the received signals at the relay and destination nodes are given, respectively, by

$$y_n^{r,s} = h_n^{r,s} x_n^s + h_n^{r,r} x_n^r + z_n^r, \qquad (4.1)$$

and

$$y_n^{d,r} = h_n^{d,r} x_n^r + h_n^{d,s} x_n^s + z_n^d. \qquad (4.2)$$

In (4.1) and (4.2), the flat fading channel coefficient $h_n^{i,j}$ and noise z_n^i are zero-mean complex Gaussian with variance $\sigma_{h_{i,j}}^2$ and $\mathcal{N}_0$, $\forall\, i \in \{r, d\}, j \in \{s, r\}$, respectively. Specifically, $h_n^{i,j}$ is the relay-relay RSI channel. Accordingly, the channel power gain $|h_n^{i,j}|^2$ is exponentially distributed with mean $\sigma_{h_{i,j}}^2$. Denote $\sigma_{h_{r,s}}^2 = \beta_1, \sigma_{h_{r,r}}^2 =$

$\beta_2, \sigma^2_{h_{d,r}} = \beta_3$ and $\sigma^2_{h_{d,s}} = \beta_4$. The average channel power gain can be represented as $\beta_1 = G \cdot D^{-\nu}_{s,r}$, $\beta_3 = G \cdot D^{-\nu}_{r,d}$, and $\beta_4 = G \cdot D^{-\nu}_{s,d}$ when the direct link is considered, where ν is the path loss exponent of the wireless channel and G is a constant which we set to 1 without loss of generality. In the following, we will evaluate the resource optimization performance in terms of the RSI channel power gain β_2.

Assume that the processing delay at the relay R is 1 time unit, then x^r_n is the decoded information based on the received signal $y^{r,s}_{n-1}$, at the former time instant. The SINR at the relay is computed as

$$\Gamma_r = \frac{|h^{r,s}_n|^2 P_s}{|h^{r,r}_n|^2 P_r + \mathcal{N}_0} = \frac{|h^{r,s}_n|^2 \gamma_s}{|h^{r,r}_n|^2 \gamma_r + 1}, \tag{4.3}$$

and SINRs at the destination for both direct-link (DL) and no-direct-link (NDL) systems are

$$\Gamma_d = \frac{|h^{d,r}_n|^2 P_r}{|h^{d,s}_n|^2 P_s + \mathcal{N}_0} = \frac{|h^{d,r}_n|^2 \gamma_r}{|h^{d,s}_n|^2 \gamma_s + 1}, \tag{4.4}$$

and

$$\Gamma_d = \frac{|h^{d,r}_n|^2 P_r}{\mathcal{N}_0} = |h^{d,r}_n|^2 \gamma_r, \tag{4.5}$$

where $\gamma_s = \frac{P_s}{\mathcal{N}_0}$ and $\gamma_r = \frac{P_r}{\mathcal{N}_0}$ are the transmit signal to noise ratios (SNRs) at the source and relay, respectively.

4.1.2 Outage probability

DF relaying is considered in this study. In this scheme, the relay will decode the source data and retransmit the data to the destination if it is correctly decoded. The

outage probability for DF relaying is given by

$$P_{outage} = \mathbb{P}\{\Gamma_r < \eta\} + (1 - \mathbb{P}\{\Gamma_r < \eta\})\,\mathbb{P}\{\Gamma_d < \eta\}, \qquad (4.6)$$

where η is the required SINR for successful transmission for both the S-R and the R-D link. We can relate the SINR threshold η with a target rate R (in bps/Hz) by $\log_2(1 + \eta) = R$.

The closed form expression for the outage probability can be computed as follows [34]:

$$P_{outage} = 1 - \frac{1}{\left(1 + \eta\frac{\beta_2}{\beta_1}\frac{\gamma_r}{\gamma_s}\right)\left(1 + \eta\frac{\beta_4}{\beta_3}\frac{\gamma_s}{\gamma_r}\right)} \exp\left[-\eta\left(\frac{1}{\beta_1\gamma_s} + \frac{1}{\beta_3\gamma_r}\right)\right]. \qquad (4.7)$$

It is evident that when $\beta_2 = 0$, the full-duplex system works in ideal case without self-interference at the relay node. When $\beta_4 = 0$, the direct link is not considered.

For half-duplex systems, since the S-R and R-D transmissions occur on orthogonal channels, there is no self-interference at the relay node. Also the S-D transmission is used for diversity at the destination node, instead of being treated as interference. The outage probability for half-duplex DF relaying can be obtained as follows [35, 34]:

$$P_{outage}^{HD} = 1 - \frac{1}{\left(1 - \frac{\beta_4}{\beta_3}\frac{\gamma_s}{\gamma_r}\right)} \exp\left[-\eta\left(\frac{1}{\beta_1\gamma_s} + \frac{1}{\beta_3\gamma_r}\right)\right] - \frac{1}{\left(1 - \frac{\beta_3}{\beta_4}\frac{\gamma_r}{\gamma_s}\right)} \exp\left[-\eta\left(\frac{1}{\beta_1\gamma_s} + \frac{1}{\beta_4\gamma_s}\right)\right]. \qquad (4.8)$$

If the direct S-D transmission is not considered, then the outage probability will reduce to

$$P_{outage}^{HD} = 1 - \exp\left[-\eta\left(\frac{1}{\beta_1\gamma_s} + \frac{1}{\beta_3\gamma_r}\right)\right]. \qquad (4.9)$$

For a fair outage performance comparison between the full-duplex and half-duplex systems, we require that the target rate for the half-duplex system is twice that of the full-duplex system.

4.2 Resource optimization for two-hop relaying

In this section, we investigate the optimal resource (both power and location) allocation which provides the minimum outage probability. We define the power ratio between the source and relay nodes as $\rho_\gamma = \frac{\gamma_s}{\gamma_r}$ ($\rho_\gamma > 0$), and the distance ratio as $\rho_D = D_{s,r}/D$ ($0 < \rho_D < 1$). Then the relay location can be specified with the two parameters: the distance ratio ρ_D and the sum distance D.

4.2.1 Power optimization

In this study, we are interested in designing power allocation algorithms that minimize the outage probability subject to two kinds of constraints: one is the individual power constraints and the other is the sum power constraint. For simplicity, the individual power constraints for both the source and the relay are set to be identical in the following discussions. However, the following results can be readily extended for problems with non-identical individual power constraints. We treat the two kinds of constraints separately in the following. Based on the results for the two separate problems, the power allocation problem with the combined power constraints can be readily solved with clipping.

4.2.1.1 Power allocation with individual constraints

Problem Statement 4.1 *For any given relay node location $D_{s,r}$, sum distance D (β_1 and β_3), relay self-interference level β_2, and the individual SNR constraint γ_m for both the source and the relay, determine the optimal transmit SNRs γ_s^o and γ_r^o, which*

$$\underset{\gamma_s, \gamma_r}{minimize} \quad P_{outage}(\gamma_s, \gamma_r)$$

$$subject\ to \quad 0 < \gamma_s \leq \gamma_m,\ 0 < \gamma_r \leq \gamma_m.$$

Proposition 4.1 *For NDL systems ($\beta_4 = 0$), the optimal transmit SNRs for the source and relay nodes are given, respectively, by*

$$(\gamma_s^o, \gamma_r^o) = \begin{cases} (\gamma_m, \gamma_m), & if\ \gamma_m < \gamma_{th} \\ \\ (\gamma_m, \gamma_o), & if\ \gamma_m \geq \gamma_{th} \end{cases} \tag{4.10}$$

with

$$\gamma_{th} = \frac{1}{\beta_3}\left(\frac{\beta_1}{\beta_2} + \eta\right) \tag{4.11}$$

and

$$\gamma_o = \frac{\eta}{2\beta_3} + \sqrt{\frac{\eta^2}{4\beta_3^2} + \frac{\beta_1 \gamma_m}{\beta_2 \beta_3}}. \tag{4.12}$$

Proof. The convexity of P_{outage} in terms of γ_s and γ_r can be readily verified. Set $\beta_4 = 0$ and denote $S(\gamma_s, \gamma_r) = -\ln(1 - P_{outage}(\gamma_s, \gamma_r))$. Then we can apply the

Karush-Kuhn-Tucker (KKT) condition to find the unique global minimizer as follows:

$$
\begin{cases}
\frac{\partial S(\gamma_s, \gamma_r)}{\partial \gamma_s} + \mu_1 = 0 \\[2mm]
\frac{\partial S(\gamma_s, \gamma_r)}{\partial \gamma_r} + \mu_2 = 0 \\[2mm]
\mu_1(\gamma_s - \gamma_m) + \mu_2(\gamma_r - \gamma_m) = 0 \\[2mm]
\mu_1 \geq 0, \ \mu_2 \geq 0, \ 0 < \gamma_s \leq \gamma_m, \ 0 < \gamma_r \leq \gamma_m
\end{cases}
\tag{4.13}
$$

Since $\frac{\partial S(\gamma_s, \gamma_r)}{\partial \gamma_s} < 0$ for all $\gamma_s > 0$, solution $\gamma_s^o = \gamma_m$ is fairly straightforward. Solution γ_r^o can also be obtained by solving (4.13). ∎

The intuition for solution (4.10) is as follows. When there is no individual SNR constraint, the outage probability is a monotonically decreasing function of γ_s. For any given γ_s, the optimal transmit SNR for the relay node is given by Eq. (4.12) by solving $\frac{\partial S(\gamma_s, \gamma_r)}{\partial \gamma_r} = 0$. When the individual maximum allowed SNR constraint γ_m is imposed, the source node will always employ the maximum allowed transmit SNR γ_m. However, for the relay node, the maximum allowed transmit SNR is not always optimal, depending on the value of γ_m and γ_{th} as given by (4.11). When γ_m is larger than γ_{th}, the self-interference at the relay node may be so strong that the outage performance would be degraded if γ_m is adopted by the relay node.

Proposition 4.2 *For DL systems ($\beta_4 \neq 0$), the optimal transmit SNRs for the source and the relay, depending on the power constraint γ_m and RSI β_2, can be found as follows:*

- *Case 1: $\beta_2 = 0$*

$$(\gamma_s^o, \gamma_r^o) = \begin{cases} (\gamma_m, \gamma_m), & if \ \gamma_m < \frac{\beta_3 + \eta\beta_4}{\beta_1\beta_4} \\ \\ (\hat{\gamma}, \gamma_m), & if \ \gamma_m \geq \frac{\beta_3 + \eta\beta_4}{\beta_1\beta_4} \end{cases} \tag{4.14}$$

with

$$\hat{\gamma} = \frac{\eta\beta_4 + \sqrt{\eta^2\beta_4^2 + 4\beta_1\beta_3\beta_4\gamma_m}}{2\beta_1\beta_4}. \tag{4.15}$$

- *Case 2: $\beta_2 > 0$*

$$(\gamma_s^o, \gamma_r^o) = \begin{cases} (\gamma_m, \gamma_m), & if \ \gamma_m < \min(\gamma_r^o(\gamma_m), \gamma_s^o(\gamma_m)) \\ \\ (\gamma_m, \gamma_r^o(\gamma_m)), & if \ \gamma_r^o(\gamma_m) \leq \gamma_m \leq \gamma_s^o(\gamma_m) \\ \\ (\gamma_s^o(\gamma_m), \gamma_m), & if \ \gamma_s^o(\gamma_m) \leq \gamma_m \leq \gamma_r^o(\gamma_m) \end{cases} \tag{4.16}$$

where $\gamma_s^o(\gamma_m)$ and $\gamma_r^o(\gamma_m)$ are the solutions of $\frac{\partial S(\gamma_s, \gamma_m)}{\partial \gamma_s} = 0$ and $\frac{\partial S(\gamma_m, \gamma_r)}{\partial \gamma_r} = 0$, respectively.

Proposition 4.2 can be readily derived following the same procedures as in Proposition 4.1. Note that, different from the NDL system, the outage probability is not a monotonically decreasing function of γ_s, the DL system has an optimal source transmit SNR for any given relay transmit SNR. This is induced by the interference at the destination from the source transmission, as shown in Eq. (4.4). However, if the self interference can be completely eliminated ($\beta_2 = 0$), then the outage probability is a monotonically decreasing function of γ_r. If not, for any given source transmit SNR, there is also an optimal relay transmit SNR. Specifically, when there is no individual power constraint, for a given γ_r, the optimal transmit SNR for the source node can

be found by solving

$$\frac{\partial S(\gamma_s, \gamma_r)}{\partial \gamma_s} = 0. \tag{4.17}$$

For a given γ_s, the optimal transmit SNR for the relay node can be found by solving

$$\frac{\partial S(\gamma_s, \gamma_r)}{\partial \gamma_r} = 0. \tag{4.18}$$

4.2.1.2 Power allocation with sum constraint

Problem Statement 4.2 *For any given relay location $D_{s,r}$ (β_1 and β_3), and relay self-interference level β_2, determine the optimal transmit SNRs γ_s^o and γ_r^o, which*

$$\underset{\gamma_s, \gamma_r}{minimize} \quad P_{outage}(\gamma_s, \gamma_r)$$

$$subject\ to \quad \gamma_s > 0,\ \gamma_r > 0,\ \gamma_s + \gamma_r = \gamma.$$

Proposition 4.3 *For systems without a direct link (NDL), the unique optimal transmit SNR ratio between the source and the relay ($\rho_\gamma^o = \frac{\gamma_s^o}{\gamma_r^o}$) for the above power allocation problem can be found by solving the following equation:*

$$\beta_1^2 \rho_\gamma^3 + \eta \beta_1 \beta_2 \rho_\gamma^2 - \beta_1 \beta_3 (1 + \beta_2 \gamma) \rho_\gamma - \eta \beta_2 \beta_3 = 0,\ \rho_\gamma > 0. \tag{4.19}$$

Proof. Set $\beta_4 = 0$ and denote $S = -\ln(1 - P_{outage})$. For any given β_1, β_2, and β_3, we have

$$S(\rho_\gamma) = \frac{\eta}{\gamma} \left[\frac{1}{\beta_1} \left(\frac{1}{\rho_\gamma} + 1 \right) + \frac{1}{\beta_3} (\rho_\gamma + 1) \right] + \ln\left(1 + \eta \frac{\beta_2}{\beta_1} \frac{1}{\rho_\gamma} \right). \tag{4.20}$$

It is easy to verify that (4.20) is a convex function of ρ_γ since

$$\frac{\mathrm{d}^2 S(\rho_\gamma)}{\mathrm{d}\rho_\gamma^2} = \eta \left[\frac{2}{\beta_1 \gamma \rho_\gamma^3} + \frac{\beta_2(2\beta_1\rho_\gamma + \eta\beta_2)}{(\beta_1\rho_\gamma^2 + \eta\beta_2\rho_\gamma)^2} \right] > 0, \forall \rho_\gamma > 0. \tag{4.21}$$

Then, by taking the first order derivative of (4.20) with respect to ρ_γ and setting it to zero, we can find the unique optimal ρ_γ^o which satisfies (4.19). ■

The exact closed-form solution for this cubic equation is readily available. However, the closed-form solution is too complicated to provide much insight. We conduct the perturbation analysis on the parameter β_2 to examine the effect of the self-interference level β_2 on the transmit power optimization.

Note that when $\beta_2 = 0$, the outage probability is the same as the half-duplex mode and the optimal transmit SNR ratio between the source and relay nodes is given by

$$\rho_\gamma^o = \sqrt{\frac{\beta_3}{\beta_1}}, \tag{4.22}$$

which is consistent with the result in [28].

When β_2 is positive and very small, let $\beta_2 = \epsilon$ and $\rho_\gamma = \rho_0 + \epsilon\rho_1$. Then by substituting β_2 and ρ_γ into (4.19), carrying out elementary operations, collecting coefficients of like powers of ϵ only with terms up to $O(\epsilon)$ retained, and equating the coefficient of each power of ϵ to zero, we have

$$\begin{cases} \beta_1\rho_0(\beta_1\rho_0^2 - \beta_3) = 0 \\ 3\beta_1^2\rho_0^2\rho_1 - \beta_1\beta_3(\rho_1 + \rho_0\gamma) + \eta(\beta_1\rho_0^2 - \beta_3) = 0. \end{cases} \tag{4.23}$$

This leads to:

$$
\begin{cases}
\rho_0 = \sqrt{\dfrac{\beta_3}{\beta_1}} \\[3mm]
\rho_1 = \dfrac{\gamma}{2}\rho_0.
\end{cases}
\tag{4.24}
$$

In other words, when β_2 is a very small and positive, we have

$$
\rho_\gamma = \sqrt{\frac{\beta_3}{\beta_1}}\left(1 + \frac{\gamma}{2}\beta_2\right).
\tag{4.25}
$$
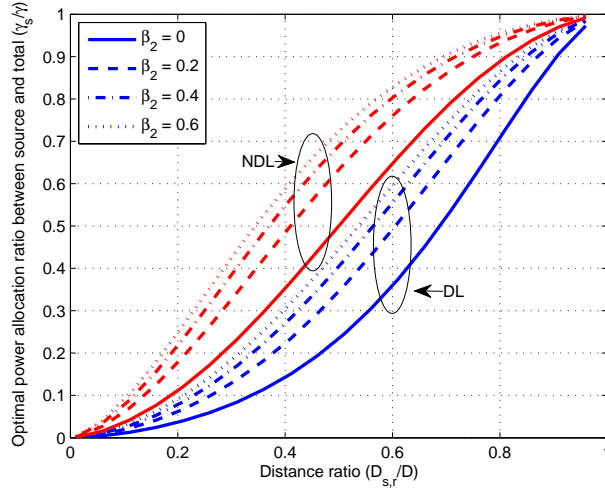
Figure 4.2: Optimal power allocation for different relay locations ($R = 0.5$ bps/Hz, $\gamma = 10$ dB, $D_{s,d} = 1.0$, $D = 1.2$, $\nu = 3$).

From (4.25), it is clear that, for a given relay node location, as the RSI at the relay node increases, the optimal transmit power ratio between the source and relay also increases. This is intuitive since the source node needs to increase the transmit power in order to maintain good reception at the relay node when the RSI at the relay node becomes stronger.

Proposition 4.4 *For systems with a direct link (DL), the unique optimal transmit SNR ratio between the source and relay ($\rho_\gamma^o = \frac{\gamma_s^o}{\gamma_r^o}$) for the above power allocation*

problem can be found by solving the following equation:

$$\frac{\beta_1}{\beta_3}\rho_\gamma^2 = \frac{\beta_2\gamma + C}{\beta_4\gamma + C},$$

(4.26)

where $C = 1 + \eta^2\frac{\beta_2\beta_4}{\beta_1\beta_3} + \eta\frac{\beta_2}{\beta_1}\frac{1}{\rho_\gamma} + \eta\frac{\beta_4}{\beta_3}\rho_\gamma.$

Eq. (4.26) can be obtained following the same procedures as in Proposition 3. Note that when $\beta_2 = \beta_4 = 0$, Eq. (4.26) reduces to Eq. (4.22), which corresponds to the optimal result for the half-duplex scenario without a direct link.

Fig. 4.2 depicts the optimal power allocation for both scenarios with and without a direct link and when the relay placement varies. It is clear that as the relay node moves towards the destination, more transmit power is allocated to the source node. For a given relay location, as the RSI at the relay node increases, the transmit power allocated to the source node also increases in order to guarantee good SINR at the relay node. In addition, for a given self-interference level and relay location, the optimal power allocated to the source node for the DL system is smaller than that of the NDL system. This is due to the fact that the direct link transmission is interfering with the relay-destination transmission, thus the SINR at the destination refrains the source from transmitting at higher power.

4.2.1.3 Numerical examples
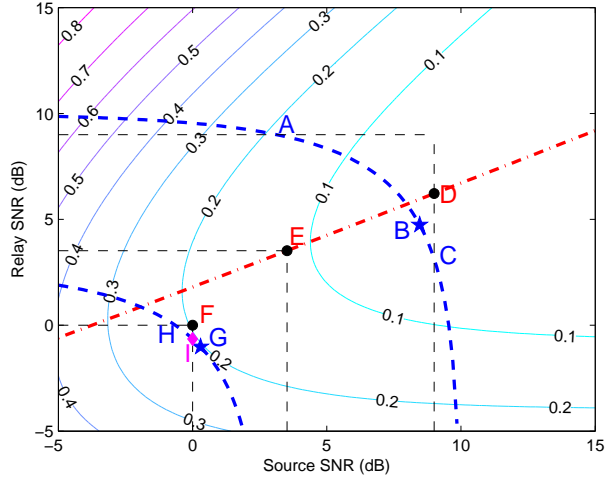
(a) NDL relaying (the red dash-dotted curve is the optimized relay SNR (given by Eq. (4.12)) for any given source SNR; the black dashed curves are three different individual power constraints with $\gamma_m = 0$, 3.521, and 9 dB, respectively; the blue dashed curves are two sum constraints with $\gamma = 2.7$ and 10 dB, respectively)
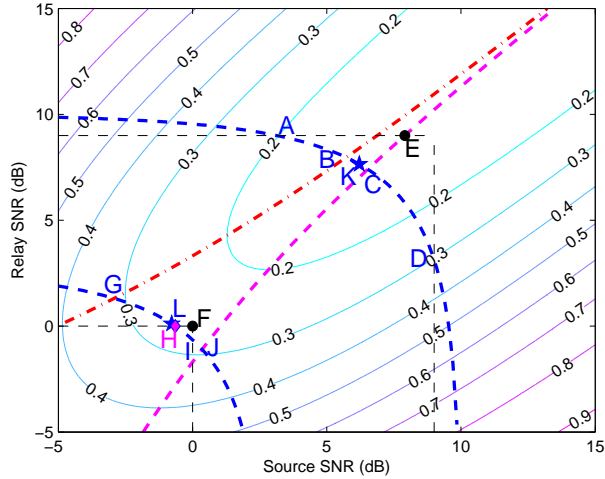
(b) DL relaying (the red dash-dotted curve is the optimized relay SNR (given by Eq. (4.18)) for any given source SNR; the magenta dashed curve is the optimized source SNR (given by Eq. (4.17)) for any given relay SNR; the black dashed curves are two different individual power constraints with $\gamma_m = 0$ and 9 dB, respectively; the blue dashed curves are two sum constraints given by $\gamma = 2.7$ and 10 dB, respectively)

Figure 4.3: The outage contour for source and relay transmit SNRs ($R = 0.5$ bps/Hz, $D_{s,r} = 0.6$, $D = 1.2$, $D_{s,d} = 1.0$, $\nu = 3$, $\beta_2 = 0.1\beta_1$).

Figs. 4.3a and 4.3b show the corresponding outage probability contours for NDL and DL relaying systems, respectively, for a specific system setting. In Fig. 4.3a, the threshold value is $\gamma_{th} = 3.521$ dB. Then for the three individual SNR constraints ($\gamma_m = 0$, 3.521, and 9 dB), the corresponding optimal solutions are given by the points F, E, and D, respectively, according to Proposition 4.1. For the sum SNR constraint ($\gamma = 10$ dB), the optimal solution is given by point B, which is obtained by solving Eq. (4.19). If we consider the combined individual SNR constraint ($\gamma_m = 9$ dB) and sum SNR constraint, then the feasible solutions lie on the curve from point A to point C and the optimal solution given by point B is a feasible solution, so B is also the optimal solution for the combined constraint problem. For another sum SNR constraint ($\gamma = 2.7$ dB), the optimal solution is given by point G. If we combine this sum constraint with the individual SNR constraint ($\gamma_m = 0$ dB), then G is not a feasible solution for the combined problem. In this case, the optimal solution is given by point I by clipping.

In Fig. 4.3b, for the individual SNR constraint $\gamma_m = 0$ dB, it is seen from the figure that $\gamma_m < \min(\gamma_r^o(\gamma_m), \gamma_s^o(\gamma_m))$, then the optimal solution lies in point F. For $\gamma_m = 9$ dB, it is seen that $\gamma_s^o(\gamma_m) \leq \gamma_m \leq \gamma_r^o(\gamma_m)$, then the optimal solution lies in point E. For the sum SNR constraint ($\gamma = 10$ dB), the optimal solution K can be found by solving Eq. (4.26), which lies on the curve from point B to point C. If we consider the individual SNR constraint ($\gamma_m = 9$ dB) and sum SNR constraint together, then K is also the optimal solution for the combined problem. For another sum SNR constraint ($\gamma = 0$ dB), the optimal solution is in point L. If we combine

this sum constraint with the individual SNR constraint ($\gamma_m = 0$ dB), then L is out of the feasible region given by the curve from H to I. Again we can find the optimal solution at point H by clipping.

4.2.2 Location optimization

For the relay location optimization, we adopt the ellipse network topology as shown in Fig.4.1, the rationale of which is justified as follows. Based on the channel model in Section 4.1.1, it is intuitive that for a fixed ρ_D, optimal outage performance can be achieved with $D = D_{s,d}$. This means that if there is no restriction on the relay placement, it is optimal to place the relay on the straight line between the source and the destination. However, it may not always be practical to put the relay on the source-destination line in real life scenarios due to some geographical constraints. So one straightforward approach is to sweep all the feasible sum distance D and find the optimal distance ratio ρ_D for each D. In this study, we will focus on finding the optimal ρ_D for a given $D \geq D_{s,d}$.

Problem Statement 4.3 *For any given transmit SNR at the source and relay nodes (γ_s and γ_r), relay self-interference level β_2, and the path loss exponent ν of the wireless channel, determine the optimal relay location $D^o_{s,r}$ ($\rho^o_D = \frac{D^o_{s,r}}{D}$), which*

$$\underset{D_{s,r}, D_{r,d}}{minimizes} \quad P_{outage}(D_{s,r}, D_{r,d})$$

$$subject\ to \quad D_{s,r} > 0,\ D_{r,d} > 0,\ D_{s,r} + D_{r,d} = D.$$

Proposition 4.5 *For an NDL full-duplex system, there exists a unique optimal relay*

location $D^o_{s,r}$ (ρ^o_D), *which can be computed by solving the following equation:*

$$\left(\frac{1 - \rho_D}{\rho_D}\right)^{\nu - 1} = \frac{\gamma_r}{\gamma_s} + \frac{\beta_2 \gamma_r^2}{\gamma_s + \eta \beta_2 \gamma_r (\rho_D D)^{\nu}}, \quad 0 < \rho_D < 1. \tag{4.27}$$

Proof. In NDL systems, there is no source-destination transmission, thus $\beta_4 = 0$. Define $S = -\ln(1 - P_{outage})$, which is computed as,

$$S(\rho_D) = \eta D^{\nu} \left[\frac{\rho_D^{\nu}}{\gamma_s} + \frac{(1 - \rho_D)^{\nu}}{\gamma_r}\right] + \ln\left(1 + \eta D^{\nu} \beta_2 \frac{\gamma_r}{\gamma_s} \rho_D^{\nu}\right). \tag{4.28}$$

By taking the first order derivative of (4.28) with respect to ρ_D and setting it to zero, we can find the optimal ρ^o_D as in (4.27). ∎

It is easy to verify that the optimal solution is unique since (4.27) has a unique solution and the second order derivative of (4.28) with respect to ρ_D at the optimal solution is positive.

The closed-form solution of (4.27) is not available, thus we resort to perturbation analysis of β_2 to examine the effect of the self-interference level β_2 on the location optimization.

When $\beta_2 = 0$, the system is reduced to the half-duplex mode and the optimal relay location in (4.27) can be simplified to

$$\frac{D_{s,r}}{D_{r,d}} = \left(\frac{\gamma_s}{\gamma_r}\right)^{\frac{1}{\nu - 1}}, \tag{4.29}$$

which is consistent with the result in [58].

90

For small β_2, we have $\frac{\gamma_s}{\beta_2} \gg \eta\gamma_r(\rho_D D)^\nu$, and (4.27) can be approximated as:

$$\left(\frac{1-\rho_D}{\rho_D}\right)^{\nu-1} = \frac{\gamma_r}{\gamma_s}(1+\beta_2\gamma_r), \tag{4.30}$$

and the optimal relay location can be computed as:

$$\rho_D^o = \frac{1}{1 + \left[\frac{\gamma_r}{\gamma_s}(1+\beta_2\gamma_r)\right]^{\frac{1}{\nu-1}}}. \tag{4.31}$$

From (4.31), it is clear that, for any given source and relay transmit SNRs (γ_s and γ_r), as β_2 increases, the optimal system performance is achieved by moving the relay towards the source node. This result is reasonable. As the RSI at the relay node increases, the relay node needs to move towards the source node in order to maintain good reception.

Proposition 4.6 *For a DL full-duplex system, there exists a unique optimal relay location $D_{s,r}^o$ (ρ_D^o) for the above location optimization problem, which can be computed from the following equation:*

$$\left(\frac{1-\rho_D}{\rho_D}\right)^{\nu-1} = \frac{\frac{1}{\gamma_s} + \frac{\beta_2\gamma_r}{\gamma_s+\eta\beta_2\gamma_r(\rho_D D)^\nu}}{\frac{1}{\gamma_r} + \frac{\beta_4\gamma_s}{\gamma_r+\eta\beta_4\gamma_s((1-\rho_D)D)^\nu}}, \quad 0 < \rho_D < 1. \tag{4.32}$$

Eq. (4.32) and the uniqueness of the optimal location can be proven following the same argument as in Proposition 4.5. Note that when $\beta_2 = \beta_4 = 0$, Eq. (4.32) reduces to Eq. (4.29), which corresponds to the optimal result for the half-duplex scenario with no direct link.

Fig. 4.4 depicts the optimal relay location for both DL and NDL relaying systems with the same total system transmit power but with different power allocation. It is clear that as more transmit power is allocated to the source node, the optimal relay node moves towards the destination node. For a given power allocation ratio, as the RSI (β_2) increases, the optimal relay node moves towards the source node in order to guarantee good SINR at the relay node. In addition, for a given RSI and power allocation, the optimal relay location for the DL system is closer to the destination node than that of the NDL system. This is due to the fact that the direct link transmission is interfering with the relay-destination transmission, thus the optimal relay node should be closer to the destination in order to maintain good SINR at the destination node.
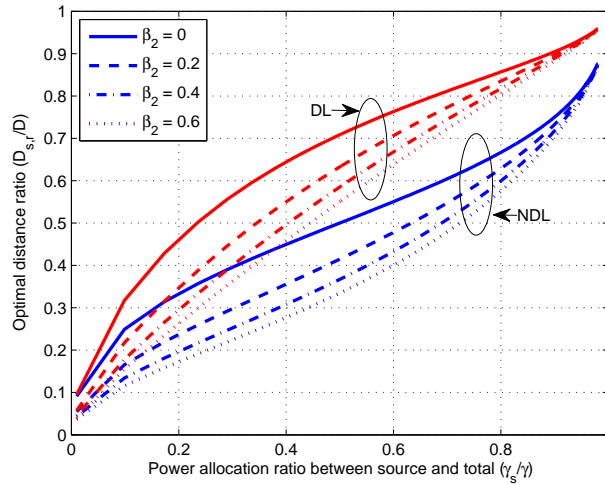
Figure 4.4: Optimal relay location for different power allocation ratios ($R = 0.5$ bps/Hz, $\gamma = 10$ dB, $D_{s,d} = 1.0$, $D = 1.2$, $\nu = 3$).

4.2.3   Joint optimization

For the joint optimization, we try to find the optimal power allocation and relay location such that the outage probability is minimized. For simplicity, we only consider the sum power constraint in the joint optimization problem.

Problem Statement 4.4 *For any given relay self-interference level β_2, and the path loss exponent ν of the wireless channel, determine the optimal combination of transmit SNRs γ_s^o and γ_r^o, and the location of the relay $D_{s,r}^o$ and $D_{r,d}^o$, which*

$$\underset{\gamma_s, \gamma_r, D_{s,r}, D_{r,d}}{minimize} \quad P_{outage}(\gamma_s, \gamma_r, D_{s,r}, D_{r,d})$$

$$subject\ to \quad D_{s,r} > 0,\ D_{r,d} > 0,\ D_{s,r} + D_{r,d} = D$$

$$and \quad \gamma_s > 0,\ \gamma_r > 0,\ \gamma_s + \gamma_r = \gamma.$$

Consider the relaying systems without a direct source-destination link. The above problem can be converted into the following equivalent problem:

$$\underset{\rho_\gamma, \rho_D}{minimize} \quad Q(\rho_\gamma, \rho_D)$$

$$subject\ to \quad \rho_\gamma > 0,\ 0 < \rho_D < 1,$$

where

$$Q(\rho_\gamma, \rho_D) = \frac{\eta D^\nu}{\gamma} \left[\rho_D^\nu \left(\frac{1}{\rho_\gamma} + 1 \right) + (1 - \rho_D)^\nu (\rho_\gamma + 1) \right] + \ln \left(1 + \eta \beta_2 \frac{(\rho_D D)^\nu}{\rho_\gamma} \right).$$

$$(4.33)$$

It can be verified that the Hessian matrix of $Q(\rho_\gamma, \rho_D)$ is not positive definite under the constraint of $\rho_\gamma > 0$, $0 < \rho_D < 1$. So the objective function P_{outage} is not a convex function of variables γ_s, γ_r, $D_{s,r}$, and $D_{r,d}$ under the given constraint for NDL relaying systems. Similarly, we can show the same observation for DL relaying systems. Thus the global optimal solution may not be unique for the joint optimization problem. In order to find the global minimizers, we first present an important property of the optimal outage probability in the following proposition.

Proposition 4.7 *For both NDL and DL relaying systems with any given relay self-interference level β_2, and the path loss exponent ν of the wireless channel, the outage probability with optimized power allocation is symmetric about the middle point. That is, for any given distance ratios ρ_D and $1 - \rho_D$, then the following equality holds:*

$$Q(\rho_{\gamma_1}, \rho_D) = Q(\rho_{\gamma_2}, 1 - \rho_D), \tag{4.34}$$

where ρ_{γ_1} and ρ_{γ_2} are the corresponding optimal power allocation ratios for ρ_D and $1 - \rho_D$, respectively, which can be found by Eq. (4.19) for NDL systems or Eq. (4.26) for DL systems.

Proof. Consider the NDL relaying system first. According to Proposition 4.3, we have

$$\frac{1}{\rho_D{}^{2\nu}}\rho_{\gamma_1}{}^3 + \frac{\eta\beta_2}{\rho_D{}^\nu}\rho_{\gamma_1}{}^2 - \frac{(1 + \beta_2\gamma)}{\rho_D{}^\nu(1 - \rho_D)^\nu}\rho_{\gamma_1} - \frac{\eta\beta_2}{(1 - \rho_D)^\nu} = 0 \tag{4.35}$$

and

$$\frac{1}{(1-\rho_D)^{2\nu}}\rho_{\gamma_2}{}^3 + \frac{\eta\beta_2}{(1-\rho_D)^{\nu}}\rho_{\gamma_2}{}^2 - \frac{(1+\beta_2\gamma)}{\rho_D{}^{\nu}(1-\rho_D)^{\nu}}\rho_{\gamma_2} - \frac{\eta\beta_2}{\rho_D{}^{\nu}} = 0. \qquad (4.36)$$

After some manipulations, we have

$$\frac{(\rho_{\gamma_1}(1-\rho_D)^{\nu})^3}{\rho_D{}^{3\nu}(1-\rho_D)^{3\nu}} + \frac{\eta\beta_2 \cdot (\rho_{\gamma_1}(1-\rho_D)^{\nu})^2}{\rho_D{}^{2\nu}(1-\rho_D)^{2\nu}} - \frac{(1+\beta_2\gamma) \cdot \rho_{\gamma_1}(1-\rho_D)^{\nu}}{\rho_D{}^{2\nu}(1-\rho_D)^{2\nu}} - \frac{\eta\beta_2}{\rho_D{}^{\nu}(1-\rho_D)^{\nu}} = 0$$

$$(4.37)$$

and

$$\frac{(\rho_{\gamma_2}\rho_D{}^{\nu})^3}{\rho_D{}^{3\nu}(1-\rho_D)^{3\nu}} + \frac{\eta\beta_2 \cdot (\rho_{\gamma_2}\rho_D{}^{\nu})^2}{\rho_D{}^{2\nu}(1-\rho_D)^{2\nu}} - \frac{(1+\beta_2\gamma) \cdot \rho_{\gamma_2}\rho_D{}^{\nu}}{\rho_D{}^{2\nu}(1-\rho_D)^{2\nu}} - \frac{\eta\beta_2}{\rho_D{}^{\nu}(1-\rho_D)^{\nu}} = 0. \quad (4.38)$$

From Eqs. (4.37) and (4.38), we have

$$\frac{\rho_{\gamma_1}}{\rho_{\gamma_2}} = \frac{\rho_D{}^{\nu}}{(1-\rho_D)^{\nu}}. \qquad (4.39)$$

Then based on Eqs. (4.39) and (4.33), it is obvious that Eq. (4.34) holds. It can be readily shown that Eq. (4.34) also holds for DL relaying systems. ■

In order to find the global minimizers, we can first find the local minimizers for $\rho_D \in (0, 0.5]$, which satisfy the following

$$\nabla Q(\rho_{\gamma}, \rho_D) = \mathbf{0}, \qquad (4.40)$$

and

$$\mathbf{Q}(\rho_\gamma, \rho_D) > 0, \tag{4.41}$$

where $\nabla Q(\rho_\gamma, \rho_D)$ and $\mathbf{Q}(\rho_\gamma, \rho_D)$ are the gradient the Hessian matrix of Q at (ρ_γ, ρ_D), respectively. Then the global minimizers can be obtained from the local minimizers based on Proposition 4.7.

4.3   Numerical results and comparisons

In this section, numerical optimization results for the DF full-duplex relaying system are provided to illustrate the optimization gain and the effect of RSI. In all results, we consider relay systems in a ellipse topology with sum distance $D = 1.2$, source-to-destination distance $D_{s,r} = 1.0$, target rate $R = 0.5$ bps/Hz, pathloss exponent $\nu = 3$, and sum power constraint $\gamma = 10$ dB. In this case, if the relay is located at the middle point, the average channel gains are $\beta_1 = \beta_3 = 4.6$. To manifest the effect of RSI, we compare the optimization results for four levels of average interference channel gain $\beta_2 = 0, 0.2, 0.4$, and 0.6.

4.3.1 Benefits of power allocation

(a) NDL relaying   (b) DL relaying

Figure 4.5: Outage probability comparison between systems with and without power optimization ($R = 0.5$ bps/Hz, $\gamma = 10$ dB, $D_{s,d} = 1.0$, $D = 1.2$, $\nu = 3$).

Figs. 4.5a and 4.5b depict the benefits of power optimization in terms of the outage probability for NDL and DL relay systems, respectively. For each system, different relay location ($D_{s,r}/D$) ratios and RSI levels (β_2) are considered for comparison. We observe that: i) the systems with optimal power allocation outperform the un-optimized systems under all conditions; ii) the outage probability minima of the optimized systems and the un-optimized ones are quite different.

For both NDL and DL relay systems with uniform power allocation (un-optimized), when the relay node is closer to the source, the outage probabilities with different RSI levels are almost the same. This is because in this case the relay-destination link is the weaker link and thus dominates the outage performance. However, for DL relay systems, with the additional interference to the destination induced by the direct link transmission, the outage probability is clearly much worse than NDL systems. As the relay node moves towards the destination, the source-relay link is the weaker link and the RSI at the relay node begins to play a decisive role in the received SINR at the

relay node. Thus the outage probabilities begin to differ drastically for different RSI levels. In addition, as the RSI increases, both un-optimized NDL and DL systems have the unique minimum outage probability when the relay node is closer to the source. The difference is that, with a given RSI, DL systems have the unique minimum outage probability when the relay node is closer to the destination compared to NDL systems. In this way, the source-relay link and relay-destination link are balanced.

With transmit power optimization, the source-relay and relay-destination link become more balanced with different relay placement for both NDL and DL relay systems. Furthermore, for the optimized systems, the RSI level has great effect on the optimization result. For example, for the optimized NDL relay system, as illustrated more clearly in Fig. 4.5a, the minimum outage probability is achieved at the middle point when β_2 is small (for example, $\beta_2 = 0$ and 0.2). When β_2 increases (for example, $\beta_2 = 0.4$ and 0.6), there exist a pair of relay locations, which are symmetric about the middle point, that can achieve the minimum outage probability with optimal power allocation. The larger the β_2, the further away from the middle point for the two optimal relay locations. This implies that, as the self-interference increases, the relay node can be placed either closer to the source or closer to the destination with proper power allocation to balance the source-relay and relay-destination link to minimize the system outage probability. Similar behaviours can also be observed for the optimized DL relay system.

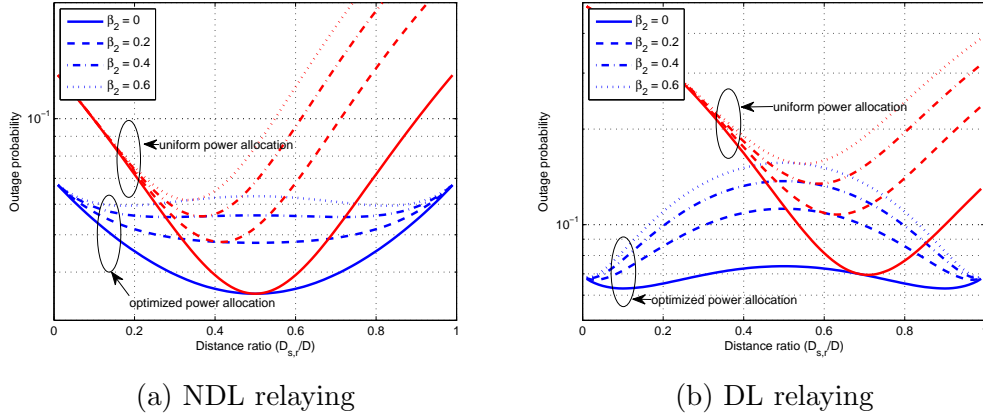### 4.3.2 Benefits of location optimization
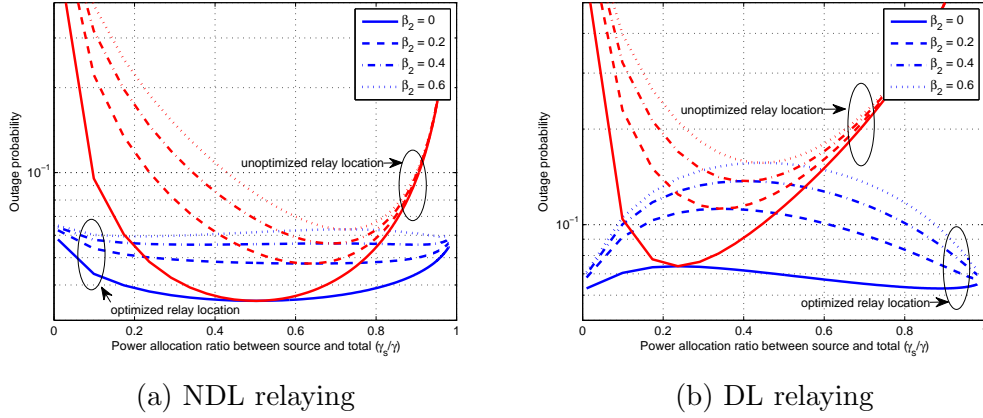
Figure 4.6: Outage probability comparison between systems with and without location optimization ($R = 0.5$ bps/Hz, $\gamma = 10$ dB, $D_{s,d} = 1.0$, $D = 1.2$, $\nu = 3$).

In Figs. 4.6a and 4.6b, we plot the results for relaying systems with and without location optimization and for both NDL and DL relaying systems, respectively. For each system, different power allocation (γ_s/γ) ratios and RSI levels (β_2) are considered for comparison. We observe from the figures that all relaying systems with optimal relay location outperform the corresponding un-optimized systems for all power allocation setups and RSI levels. For the optimized NDL and DL relaying systems, the outage probability curves are more flat than the un-optimized ones. This is because with location optimization, the source-relay and relay-destination links become more balanced with different power allocation ratios.

For both NDL and DL relaying systems without location optimization, as more power is allocated to the source, the outage probability gets similar for different RSI levels. This is due to the fact that the effect of RSI gets less important with smaller relay transmit power, and the SINR at the relay is similar with large source transmit power. On the other hand, as the transmit power for the source node decreases,

the effect of different RSI levels on the outage probability becomes very significant. This is because the source-relay link is the weaker link and dominates the outage performance. The RSI at the relay node plays a decisive role in the received SINR at the relay node. In addition, for the un-optimized DL systems, due to the effect of interference caused by the source-destination direct link transmission, the source transmit power should be reduced to achieve the outage probability minima compared to NDL systems.

It is also observed that, as RSI increases, the outage probability also increases. The outage probability minima of the optimized systems and the un-optimized ones are quite different. Specifically, for the un-optimized NDL systems, when $\beta_2 = 0$, it is obvious that uniform power allocation is the best. As β_2 increases, more power should be allocated to the source node in order to balance the source-relay and relay-destination link. Furthermore, the RSI level has marked impact on the optimization result. For example, for the optimized NDL relaying system, as illustrated in Fig. 4.6a, there is only one power allocation ratio that can achieve the minimum outage probability for no or low RSI (for example, $\beta_2 = 0$ and 0.2) while there exist two power allocation ratios that can achieve the same minimum outage probability as β_2 increases (for example, $\beta_2 = 0.4$ and 0.6). This implies that, as the RSI increases, the source transmit power can be either much higher or much lower with proper relay location optimization to balance the source-relay and relay-destination link to minimize the system outage probability. This is also consistent with the results in Section 4.3.1. Similarly, such behaviors can also be observed for DL relaying systems.

4.3.3 Benefits of joint optimization

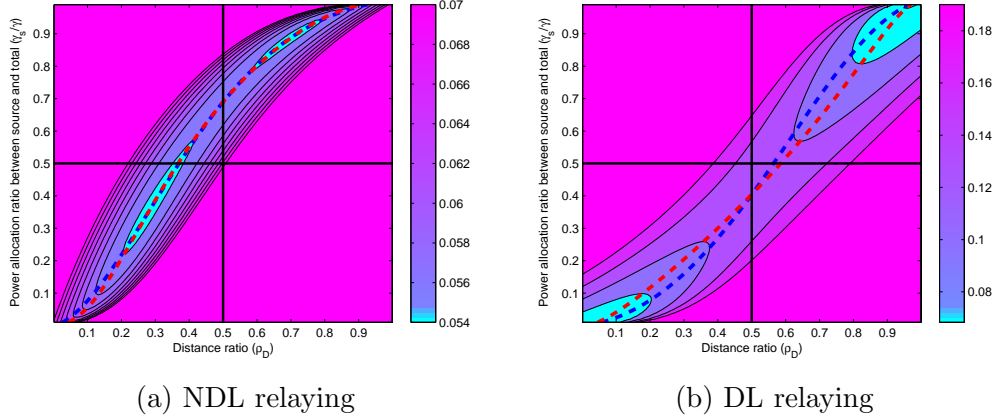(a) NDL relaying   (b) DL relaying

Figure 4.7: The outage probability contour ($R = 0.5$ bps/Hz, $\gamma = 10$ dB, $D_{s,d} = 1.0$, $D = 1.2$, $\nu = 3$, $\beta_2 = 0.4$). The red dashed curve represents the optimized location, the blue dashed curve represents the optimized power allocation, the two black solid curves correspond to the un-optimized location and un-optimized power allocation.

Figs.4.7a and 4.7b depict the outage probability contour for NDL and DL relaying systems, respectively. An RSI level of $\beta_2 = 0.4$ is considered. In both figures, the horizontal line represents the outage of the system with uniform power allocation and the vertical line represents the outage when the relay node is located in the middle point. The curves for power optimization and location optimization are also plotted. From the two figures, we can see that there exist two global minimizers for both NDL and DL systems, which is consistent with the results in Section 4.3.1 and 4.3.2. It is also clear that the outage of the joint optimized systems is much better than that of the un-optimized ones. This indicates the minimum outage can not be obtained with a simply uniform power allocation or mid-distance relay location. Therefore, joint power-location optimization is needed in order to achieve the minimum outage performance. Specifically, for both NDL and DL systems in this scenario, the minimum outage can be achieved by locating the relay either closer to the source or closer

to the destination as long as proper power allocation in Section 4.2.1 is conducted. Furthermore, for DL systems, the optimal relay location is closer to the source or the destination than that of the NDL systems due to the effect of the source-destination interference link in DL systems.

4.3.4 Comparison with half-duplex relaying

(a) NDL relaying   (b) DL relaying
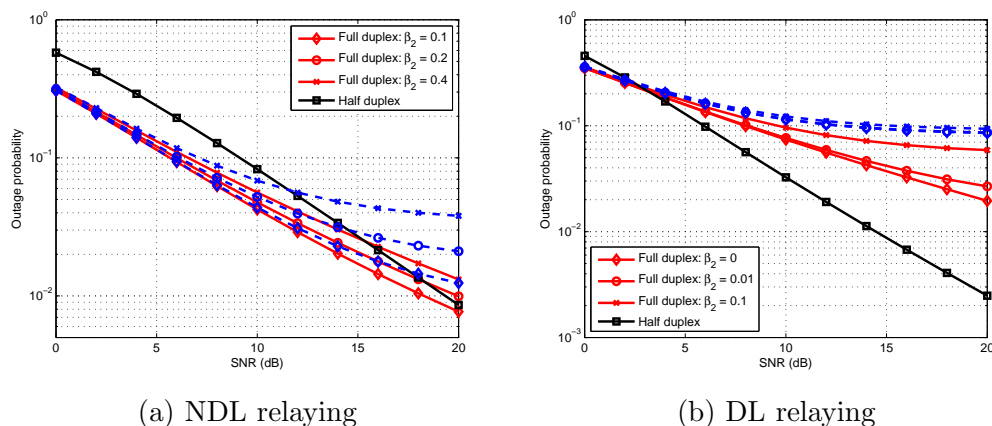
Figure 4.8: Outage probability comparison between full-duplex and half-duplex relaying ($R_{FD} = 0.5$ bps/Hz, $R_{HD} = 1.0$ bps/Hz, $D_{s,d} = 1.0$, $D = 1.2$, $D_{s,r} = 0.6$, $\nu = 3$). The red solid curves represent the outage probability for full-duplex systems with power optimization, the blue dashed curves represent the outage probability for full-duplex systems without power optimization.

The outage performance comparison between full-duplex and half-duplex relaying is shown in Fig. 4.8 for both NDL and DL systems. Different RSI levels are considered for the full-duplex relaying. For the half-duplex relaying, optimal power allocation is conducted. For the full-duplex relaying, outage results for both uniform power allocation and optimized power allocation are plotted. From Fig. 4.8a, we observe that when the SNR is low, the outage probability for full-duplex relaying is better than half-duplex relaying. As the SNR increases, the full-duplex relaying without power op-

timization begins to perform worse than half-duplex relaying due to self-interference, especially when β_2 is large ($\beta_2 = 0.2$ and 0.4). However, with power optimization, the outage performance is comparable to that of the half-duplex relaying. On the other hand, for DL relaying in Fig. 4.8b, the half-duplex system outperforms the full-duplex system no matter whether the power optimization is employed or not. This is due to the fact that, in half-duplex system, the source-destination link is used for diversity while in full-duplex system, the direct link is treated as interference.

4.4   Conclusions

In this chapter, we investigated the resource optimization of full-duplex DF relaying systems. Based on the metric of outage probability, the transmit power optimization, relay location optimization, and joint optimization problems were formulated and the optimal solutions were presented. Analyses of optimization results were provided for both DL and NDL relaying systems. It is shown that the RSI at the relay node has significant impact on the optimization results. In particular, as the RSI increases, the optimal power allocation and relay location further deviate from that of traditional half-duplex systems. In addition, the interference caused by the direct-link transmission requires that the optimal relay system either to allocate less power to the source, or to place the relay closer to the destination, in comparison with the NDL systems. Numerical results also confirmed that significant outage probability gain can be achieved with both power optimization and location optimization. The global optimal solutions for the joint power and location optimization may not be

103

unique, depending on the RSI level. We observed that, as the RSI increases, minimal outage probability can be achieved either by locating the relay closer to the source with a small source transmit power, or by locating the relay closer to the destination with a large source transmit power. The outage performance comparison between full-duplex and half-duplex relaying was also studied and the effect of resource optimization on the performance comparison has been examined.

CHAPTER 5

CONCLUSIONS

In this dissertation, we studied two techniques aiming at improving the spectrum efficiency for future wireless communication systems, namely, small cell enhancement and full-duplex relaying. In terms of small cell enhancement, we first investigated Dynamic TDD in the LTE macro-assisted small cell architecture. For an arbitrarily-located UE in a small cell network, we applied results from stochastic geometry to derive expressions for the distribution of DL SINR at an arbitrary UE and the distribution of UL SINR at its serving BS. The analytic results were verified by system level simulations. In order to deal with the severe inter-cell interference problem in dynamic TDD, we further proposed a frequency domain interference coordination technique. System level simulations based on more realistic system models and assumptions were conducted to evaluate the performance of dynamic TDD systems and the proposed interference coordination technique. Then we studied the AAS-enabled 3D beamforming for traffic load balancing and capacity enhancement in the macro-assisted small cell architecture. Load balancing algorithms together with the UE-specific beamforming scheme have been proposed. We also demonstrated that the flexible and dynamic 3D beamforming with narrow beamwidth can achieve significant performance gain compared to the conventional sectorization with fixed antenna down-tilt scheme in terms of both the cell average capacity and the cell edge user throughput. It was also shown that our proposed UE group-specific beamforming as a more realistic operation

can approach to the performance of UE-specific beamforming.

In addition, we considered applying full-duplex in cooperative relaying networks and investigated the optimal resource allocation (both power and relay location) for full-duplex decode-and-forward relaying systems. The outage probability was adopted as the optimization criterion and a two-dimensional optimization problem was formulated for systems with and without the direct source-destination link. Analytic and numerical results were provided to demonstrate advantages of the resource optimization. More interestingly, the effect of residual self-interference introduced by full-duplex transmission was investigated in terms of optimal resource allocation and outage probability performance improvement.

LIST OF REFERENCES

[1] 3GPP, "Evolved Universal Terrestrial Radio Access (E-UTRA); Further advancements for E-UTRA physical layer aspects," 3rd Generation Partnership Project (3GPP), TR 36.814, March 2010.

[2] ——, "Evolved Universal Terrestrial Radio Access (E-UTRA); Physical layer procedures," 3rd Generation Partnership Project (3GPP), TS 36.213, 2010.

[3] ——, "Evolved Universal Terrestrial Radio Access (E-UTRA); Radio Frequency (RF) system scenarios," 3rd Generation Partnership Project (3GPP), TR 36.942, 2010.

[4] ——, "Evolved Universal Terrestrial Radio Access (E-UTRA); User Equipment (UE) radio transmission and reception," 3rd Generation Partnership Project (3GPP), TS 36.101, March 2012.

[5] M. Al-Rawi and R. Jantti, "A dynamic TDD inter-cell interference coordination scheme for Long Term Evolution networks," in *IEEE 22nd International Symposium on Personal Indoor and Mobile Radio Communications (PIMRC)*, Toronto, ON, Sept. 11-14, 2011, pp. 1590–1594.

[6] J. Andrews, F. Baccelli, and R. Ganti, "A tractable approach to coverage and rate in cellular networks," *IEEE Transactions on Communications*, vol. 59, no. 11, pp. 3122–3134, 2011.

[7] J. Andrews, R. Ganti, M. Haenggi, N. Jindal, and S. Weber, "A primer on spatial modeling and analysis in wireless networks," *IEEE Communications Magazine*, vol. 48, no. 11, pp. 156–163, 2010.

[8] ARTIST4G, "D1.2-Innovative advanced signal processing algorithms for interference avoidance," Advanced Radio InTerface TechnologIes for 4G SysTems (ARTIST4G), Tech. Rep., December 2010.

[9] B. Yu, S. Mukherjee, H. Ishii, and L. Yang, "Dynamic TDD support in the LTE-B enhanced Local Area architecture," in *4th IEEE International Workshop on Heterogeneous and Small Cell Networks (HetSNets) in conjunction with GLOBECOM*, Anaheim, CA, USA, Dec. 3-7, 2012, pp. 585–591.

[10] R. Cao and L. Yang, "The affecting factors in resource optimization for cooperative communications: A case study," *IEEE Transactions on Wireless Communications*, vol. 11, no. 12, pp. 4351 –4361, December 2012.

[11] ——, "Decomposed LT codes for cooperative relay communications," *IEEE Journal on Selected Areas in Communications*, vol. 30, no. 2, pp. 407–414, 2012.

[12] M. Caretti, M. Crozzoli, G. M. Dell'Aera, and A. Orlando, "Cell splitting based on active antennas: Performance assessment for LTE system," in *IEEE 13th*

Annual Wireless and Microwave Technology Conference (WAMICON), Cocoa Beach, FL, USA, April 15-17, 2012, pp. 1–5.

[13] X. Cheng, B. Yu, L. Yang, J. Zhang, G. Liu, Y. Wu, and L. Wan, "Communicating in the Real World: 3D MIMO," *IEEE Wireless Communications Magazine*, vol. 21, no. 4, pp. 136–144, August 2014.

[14] X. Cheng, C.-X. Wang, H. Wang, X. Gao, X.-H. You, D. Yuan, B. Ai, Q. Huo, L.-Y. Song, and B.-L. Jiao, "Cooperative MIMO channel modeling and multi-link spatial correlation properties," *IEEE Journal on Selected Areas in Communications*, vol. 30, no. 2, pp. 388–396, 2012.

[15] W. Cho, R. Cao, and L. Yang, "Optimum resource allocation for amplify-and-forward relay networks with differential modulation," *IEEE Transactions on Signal Processing*, vol. 56, no. 11, pp. 5680–5691, November 2008.

[16] J. I. Choi, M. Jain, K. Srinivasan, P. Levis, and S. Katti, "Achieving single channel, full duplex wireless communication," in *Proceedings of the sixteenth annual international conference on Mobile computing and networking (MobiCom)*, Chicago, Illinois, USA, September 20-24, 2010, pp. 1–12.

[17] Cisco, "Cisco Visual Networking Index: Global Mobile Data Traffic Forecast Update, 2013-2018," White Paper, Feb. 2014.

[18] M. Danneberg, J. Holfeld, M. Grieger, M. Amro, and G. Fettweis, "Field trial evaluation of UE specific antenna downtilt in an LTE downlink," in *International ITG Workshop on Smart Antennas (WSA)*, Dresden, Germany, March 7-8, 2012, pp. 274–280.

[19] H. Dhillon, T. Novlan, and J. Andrews, "Coverage probability of uplink cellular networks," in *IEEE Global Communications Conference (GLOBECOM)*, Anaheim, CA, Dec. 3-7, 2012, pp. 2179–2184.

[20] M. Duarte and A. Sabharwal, "Full-duplex wireless communications using off-the-shelf radios: Feasibility and first results," in *Forty Fourth Asilomar Conference on Signals, Systems and Computers (ASILOMAR)*, Pacific Grove, CA, USA, November 7-10, 2010, pp. 1558–1562.

[21] H. ElSawy, E. Hossain, and M. Haenggi, "Stochastic geometry for modeling, analysis, and design of multi-tier and cognitive cellular wireless networks: A survey," *IEEE Communications Surveys Tutorials*, vol. 15, no. 3, pp. 996–1019, 2013.

[22] E. Everett, D. Dash, C. Dick, and A. Sabharwal, "Self-interference cancellation in multi-hop full-duplex networks via structured signaling," in *49th Annual Allerton Conference on Communication, Control, and Computing (Allerton)*, September 28-30, 2011, pp. 1619–1626.

[23] S. Foss and S. Zuyev, "On a Certain Voronoi Aggregative Process Related to a Bivariate Poisson Process," *Advances in Applied Probability*, vol. 28, pp. 965–981, 1996.

[24] C. Gloaguen, F. Voss, and V. Schmidt, "Parametric distance distributions for fixed access network analysis and planning," in *21st International Teletraffic Congress (ITC)*, Paris, Sept. 15-17 2009, pp. 1–8.

[25] I. Gradshteyn and I. Ryzhik, *Table of Integrals, Series, and Products*, sixth edition ed. Academic Press, 2000.

[26] H. Haas and S. McLaughlin, "A dynamic channel assignment algorithm for a hybrid TDMA/CDMA-TDD interface using the novel TS-opposing technique," *IEEE Journal on Selected Areas in Communications*, vol. 19, no. 10, pp. 1831 –1846, October 2001.

[27] H. Ishii, Y. Kishiyama, and H. Takahashi, "A Novel Architecture for LTE-B: C-plane/ U-plane Split and Phantom Cell Concept," in *International Workshop on Emerging Technologies for LTE-Advanced and Beyond-4G in conjunction with GLOBECOM*, Anaheim, CA, USA, Dec. 3-7, 2012, pp. 624–630.

[28] M. O. Hasna and M.-S. Alouini, "Optimal power allocation for relayed transmissions over rayleigh-fading channels," *IEEE Transactions on Wireless Communications*, vol. 3, no. 6, pp. 1999–2004, 2004.

[29] ITU, "Guidelines for evaluation of radio interface technologies for IMT-Advanced," Rep. ITU-R M.2135, 2008.

[30] M. Jain, J. I. Choi, T. Kim, D. Bharadia, S. Seth, K. Srinivasan, P. Levis, S. Katti, and P. Sinha, "Practical, real-time, full duplex wireless," in *Proceedings of the 17th annual international conference on Mobile computing and networking (MobiCom)*, Las Vegas, Nevada, USA, September 19-23, 2011, pp. 301–312.

[31] X. Jin, M. Ma, B. Jiao, and W. C. Lee, "Studies on spectral efficiency of the CDD system," in *2009 IEEE 70th Vehicular Technology Conference Fall (VTC 2009-Fall)*, Anchorage, Alaska, USA, September 20-23, 2009, pp. 1–5.

[32] J. Kingman, *Poisson Processes*, ser. Oxford Studies in Probability. Oxford University Press, 1993.

[33] J. Koppenborg, H. Halbauer, S. Saur, and C. Hoek, "3D beamforming trials with an active antenna array," in *International ITG Workshop on Smart Antennas (WSA)*, Dresden, Germany, March 7-8, 2012, pp. 110–114.

[34] T. Kwon, S. Lim, S. Choi, and D. Hong, "Optimal duplex mode for DF relay in terms of the outage probability," *IEEE Transactions on Vehicular Technology*, vol. 59, no. 7, pp. 3628–3634, September 2010.

[35] J. Laneman, D. Tse, and G. W. Wornell, "Cooperative diversity in wireless networks: Efficient protocols and outage behavior," *IEEE Transactions on Information Theory*, vol. 50, no. 12, pp. 3062–3080, 2004.

[36] C. Lee and M. Haenggi, "Interference and outage in poisson cognitive networks," *IEEE Transactions on Wireless Communications*, vol. 11, no. 4, pp. 1392–1401, 2012.

[37] S. Li and R. Murch, "Full-duplex wireless communication using transmitter output based echo cancellation," in *IEEE Global Telecommunications Conference (GLOBECOM)*, Houston, Texas, USA, December 5-9, 2011, pp. 1–5.

[38] J. Møller and D. Stoyan, "Stochastic geometry and random tessellations," in *Tesselations in the Sciences: Virtues, Techniques and Applications of Geometric Tilings*. R. van de Weijgaert and G. Vegter and V. Icke and J. Ritzerveld, Springer-Verlag, 2008.

[39] M.S. ElBamby, M. Bennis, W. Saad and M. Latva-aho, "Dynamic Uplink-Downlink Optimization in TDD-based Small Cell Networks," in *Proc. of IEEE INFOCOM workshop*, Toronto, Canada, 2014 (invited paper).

[40] A. Nosratinia, T. Hunter, and A. Hedayat, "Cooperative communication in wireless networks," *IEEE Communications Magazine*, vol. 42, no. 10, pp. 74–80, 2004.

[41] NTT DOCOMO, INC, "Requirements, Candidate Solutions, and Technology Roadmap for LTE Rel. 12 Onward," in *3GPP Workshop on Release 12 and Onwards*, Ljubljana, Slovenia, June 11-12, 2012.

[42] P. Omiyi, H. Haas, and G. Auer, "Analysis of TDD Cellular Interference Mitigation Using Busy-Bursts," *IEEE Trans. on Wireless Communications*, vol. 6, no. 7, pp. 2721 –2731, July 2007.

[43] S. Orfanidis, *Electromagnetic Waves and Antennas*. www.ece.rutgers.edu/ orfanidi/ewa.

[44] R. Prasad and A. Mihovska, *New Horizons in Mobile and Wireless Communications, vol. 1: Radio Interfaces*. Artech House, 2009.

[45] T. Riihonen, S. Werner, and R. Wichman, "Optimized gain control for single-frequency relaying with loop interference," *IEEE Transactions on Wireless Communications*, vol. 8, no. 6, pp. 2801–2806, 2009.

[46] ——, "Hybrid full-duplex/half-duplex relaying with transmit power adaptation," *IEEE Transactions on Wireless Communications*, vol. 10, no. 9, pp. 3074–3085, September 2011.

[47] ——, "Mitigation of loopback self-interference in full-duplex MIMO relays," *IEEE Transactions on Signal Processing*, vol. 59, no. 12, pp. 5983–5993, December 2011.

[48] T. Riihonen, S. Werner, R. Wichman, and Z. Eduardo, "On the feasibility of full-duplex relaying in the presence of loop interference," in *IEEE 10th Workshop on Signal Processing Advances in Wireless Communications (SPAWC)*, Perugia, Italy, June 21-24, 2009, pp. 275–279.

[49] S. Mukherjee, "Distribution of Downlink SINR in Heterogeneous Cellular Networks," *IEEE Journal on Selected Areas in Communications*, vol. 30, no. 3, pp. 575 –585, April 2012.

[50] A. Sang, X. Wang, M. Madihian, and R. D. Gitlin, "Coordinated Load Balancing, Handoff/Cell-site Selection, and Scheduling in Multi-cell Packet Data Systems," in *Proceedings of the 10th Annual International Conference on Mobile Computing and Networking (MobiCom '04)*, Philadelphia, PA, USA, September 26-October 1, 2004, pp. 302–314.

[51] S. Saur and H. Halbauer, "Exploring the vertical dimension of dynamic beam steering," in *8th International Workshop on Multi-Carrier Systems Solutions (MC-SS)*, Herrsching, Germany, May 3-4, 2011, pp. 1–5.

[52] N. Seifi, M. Coldrey, and M. Viberg, "Throughput Optimization for MISO Interference Channels via Coordinated User-Specific Tilting," *IEEE Communications Letters*, vol. 16, no. 8, pp. 1248–1251, August 2012.

[53] Z. Shen, A. Khoryaev, E. Eriksson, and X. Pan, "Dynamic uplink-downlink configuration and interference management in TD-LTE," *IEEE Communications Magazine*, vol. 50, no. 11, pp. 51–59, November 2012.

[54] I. Sohn, K. Lee, and Y. Choi, "Comparison of decentralized time slot allocation strategies for asymmetric traffic in TDD systems," *IEEE Trans. on Wireless Communications*, vol. 8, no. 6, pp. 2990 –3003, June 2009.

[55] T. Thomas and F. Vook, "Transparent user-specific 3D MIMO in FDD using beamspace methods," in *Global Communications Conference (GLOBECOM), 2012 IEEE*, Anaheim, CA, December 3-7, 2012, pp. 4618–4623.

[56] F. Voss, C. Gloaguen, F. Fleischer, and V. Schmidt, "Distributional properties of euclidean distances in wireless networks involving road systems," *IEEE Journal on Selected Areas in Communications*, vol. 27, no. 7, pp. 1047–1055, 2009.

[57] K. Yamamoto, K. Haneda, H. Murata, and S. Yoshida, "Optimal transmission scheduling for a hybrid of full- and half-duplex relaying," *IEEE Communications Letters*, vol. 15, no. 3, pp. 305–307, March 2011.

[58] C. Yang, W. Wang, S. Zhao, and M. Peng, "Power and location optimization for decode-and-forward opportunistic cooperative networks," in *IEEE Global Telecommunications Conference*, Honolulu, Hawaii, USA, November 30-December 4, 2009, pp. 1–7.

[59] Q. Ye, B. Rong, Y. Chen, C. Caramanis, and J. Andrews, "Towards an optimal user association in heterogeneous cellular networks," in *IEEE Global Communications Conference (GLOBECOM)*, Anaheim, CA, Dec 2012, pp. 4143–4147.

[60] O. Yilmaz, S. Hamalainen, and J. Hamalainen, "System level analysis of vertical sectorization for 3GPP LTE," in *6th International Symposium on Wireless Communication Systems (ISWCS)*, Siena-Tuscany, University of Siena, Italy, September 7C10, 2009, pp. 453–457.

[61] B. Yu, L. Yang, X. Cheng, and R. Cao, "Relay location optimization for full-duplex decode-and-forward relaying," in *IEEE Military Communications Conference*, San Diego, CA, USA, November 18-20, 2013.

[62] ——, "Transmit power optimization for full duplex decode-and-forward relaying," in *IEEE Global Communications Conference*, Atlanta, GA, USA, December 9-13, 2013.

[63] B. Yu, L. Yang, and H. Ishii, "3d beamforming for capacity improvement in macrocell-assisted small cell architecture," in *IEEE Global Communications Conference*, Austin, TX, USA, December 8-12, 2014.

[64] B. Yu, H. Ishii, and L. Yang, "System Level Performance Evaluation of Dynamic TDD and Interference Coordination in Enhanced Local Area Architecture," in *IEEE 77th Vehicular Technology Conference (VTC Spring)*, Dresden, Germany, June 2-5, 2013, pp. 1–6.

[65] B. Yu, L. Yang, H. Ishii, and X. Cheng, "Load Balancing with Antenna Tilt Control in Enhanced Local Area Architecture," in *IEEE 79th Vehicular Technology Conference (VTC Spring)*, Soul, Korea, May 18-21, 2014.

[66] J. Zhang, C. Pan, F. Pei, G. Liu, and X. Cheng, "Three-dimension fading channel models: A survey of elevation angle research," *IEEE Communications Magazine, accepted for publication*, vol. 52, no. 6, pp. 218–226, June 2014.

[67] R. Zhang, X. Cheng, Q. Yao, C.-X. Wang, Y. Yang, and B. Jiao, "Interference graph based resource sharing schemes for vehicular networks," *IEEE Transactions on Vehicular Technology*, 2013 (to appear).

[68] W. Zhang, D. Duan, and L. Yang, "Relay selection from a battery energy efficiency perspective," *IEEE Transactions on Communications*, vol. 59, no. 6, pp. 1525–1529, 2011.